

**UV RESONANCE RAMAN INVESTIGATION OF EXPLOSIVES' UV
PHOTOCHEMISTRY**

by

Katie L. Gares

B.S. Chemistry, Frostburg State University, 2011

Submitted to the Graduate Faculty of the
Kenneth P. Dietrich School of Arts and Sciences in partial fulfillment
of the requirements for the degree of
Doctor of Philosophy

University of Pittsburgh

2017

UNIVERSITY OF PITTSBURGH
DIETRICH SCHOOL OF ARTS AND SCIENCES

This dissertation was presented

by

Katie L. Gares

It was defended on

July 26, 2017

and approved by

Dr. Sanford A. Asher, Distinguished Professor of Chemistry, Department of Chemistry

Dr. Sean Garrett-Roe, Assistant Professor, Department of Chemistry

Dr. David Waldeck, Professor, Department of Chemistry

Dr. Kevin P. Chen, Professor, Department of Electrical Engineering

Dissertation Advisor: Dr. Sanford A. Asher, Distinguished Professor of Chemistry,
Department of Chemistry

Copyright © by Katie L. Gares

2017

UV RESONANCE RAMAN INVESTIGATION OF EXPLOSIVES' UV PHOTOCHEMISTRY

Katie L. Gares, PhD

University of Pittsburgh, 2017

Detection of explosives has become an important field of research due to the increased number of terrorist attacks utilizing improvised explosive devices (IEDs). We show that UV resonance Raman (UVRR) spectroscopy is a sensitive and incisive technique for detection of explosives. Deep UV excitation of explosives gives resonance enhancement and greater sensitivity enabling trace detection of explosives and their photochemical products.

We demonstrate how we can utilize UVRR to analyze characteristic spectral changes that result from explosives' photochemistry. In this work, we examined the 229 nm photochemistry of some of the main military explosives, TNT, RDX, and PETN in solution and solid state. We monitored the decrease in intensity of the UVRR bands of the initial explosive and the increase in intensity of the UVRR photoproduct bands during photolysis. Detection of photochemical product UVRR bands can be used to detect the previous presence of explosives even after they have been photolyzed. We determined solution state quantum yields, which gives insight to the susceptibility of the explosive to photolysis upon irradiation. We also determined the initial photoproducts formed by photolysis by using high performance liquid chromatography-high resolution mass spectrometry (HPLC-HRMS) measurements.

TABLE OF CONTENTS

PREFACE.....	XIX
1.0 INTRODUCTION.....	1
1.1 EXPLOSIVE DETECTION	1
1.1.1 Non Standoff Detection Methods	3
1.1.2 Standoff Detection Methods	4
1.1.3 Raman Spectroscopy for Detection of Explosives	6
1.1.4 UV Resonance Raman Spectroscopy for Detection of Explosives	7
1.2 PHOTOCHEMISTRY OF EXPLOSIVES	12
1.2.1 TNT Photochemistry	14
1.2.2 RDX Photochemistry.....	16
1.2.3 PETN Photochemistry.....	18
2.0 THEORY OF RAMAN SCATTERING	21
2.1 INTRODUCTION	21
2.2 CLASSICAL DESCRIPTION OF THE RAMAN EFFECT.....	24
2.3 QUANTUM MECHANICAL DESCRIPTION OF THE RAMAN EFFECT.	
.....	25

3.0	SOLUTION AND SOLID TRINITROTOLUENE (TNT) PHOTOCHEMISTRY: PERSISTENCE OF TNT-LIKE ULTRAVIOLET (UV) RESONANCE RAMAN BANDS...	30
3.1	INTRODUCTION	31
3.2	EXPERIMENTAL SECTION.....	32
3.2.1	Raman Measurements.....	32
3.2.2	Solution Samples.....	33
3.2.3	Solid Samples	34
3.2.4	Absorption Measurements.....	35
3.2.5	LCMS Measurements.....	35
3.3	RESULTS	36
3.3.1	Solid Photolysis	48
3.4	CONCLUSION	53
4.0	SOLUTION AND SOLID HEXAHYDRO-1,3,5-TRINITRO-1,3,5-TRIAZINE (RDX) ULTRAVIOLET (UV) 229 NM PHOTOCHEMISTRY	54
4.1	INTRODUCTION	55
4.2	EXPERIMENTAL.....	56
4.2.1	Raman Measurements.....	56
4.2.2	Solution Samples.....	57
4.2.3	Absorption Measurements.....	58
4.2.4	Mass Spectrometry Measurements	59
4.2.5	Solid Samples	60
4.2.6	X-ray Photoelectron Spectroscopy.....	61

4.2.7	X-ray Powder Diffraction	61
4.3	RESULTS	62
4.3.1	Solution Photolysis.....	62
4.3.2	Solid Photolysis	72
4.4	CONCLUSION	80
4.5	ACKNOWLEDGEMENT	81
5.0	UV RESONANCE RAMAN INVESTIGATION OF PENTAERYTHRITOL TETRANITRATE SOLUTION PHOTOCHEMISTRY AND PHOTOPRODUCT HYDROLYSIS	82
5.1	INTRODUCTION	83
5.2	EXPERIMENTAL.....	85
5.2.1	PETN Solution State UVRR	85
5.2.1.1	Raman Instrumentation	85
5.2.1.2	UVRR Measurements	85
5.2.1.3	Absorption Measurements	86
5.2.1.4	PETN Photolysis Quantum Yield	86
5.2.2	UVRR and Absorption Studies of NO ₂ Hydrolysis in Acetonitrile.....	87
5.3	RESULTS	88
5.3.1	PETN Photolysis	88
5.3.2	Hydrolysis of NO ₂ Photoproduct in CD ₃ CN	92
5.4	CONCLUSION	95
5.5	ACKNOWLEDGEMENT	96
6.0	DISSERTATION SUMMARY	97

APPENDIX A	100
A.1 SUPPORTING INFORMATION FOR CHAPTER 3	100
A.1.1 Solution MS/MS.....	100
A.1.2 Solid Mass Spectra	105
APPENDIX B	107
B.1 SUPPORTING INFORMATION FOR CHAPTER 4	107
APPENDIX C	110
C.1 SUPPORTING INFORMATION FOR CHAPTER 5	110
APPENDIX D	113
D.1 EXPLOSIVE HANDLING AND SAFETY PROCEDURES	113
D.1.1 Purpose	113
D.1.2 Storage	113
D.1.3 Explosive Usage	114
D.1.4 Explosive Inventory.....	115
D.1.5 Personnel Limits	115
D.1.6 Explosive Inventory.....	116
D.2 STANDARD OPERATING PROCEDURES (SOP).....	117
D.2.1 Purpose	117
D.2.2 Procedure	117
D.2.3 Sample Preparation and Experiment	118
D.2.4 Fire Safety	119
D.2.5 Emergency Procedures.....	119
D.2.6 Accident Reporting.....	120

APPENDIX E	121
E.1 DETAILS OF EXPERIMENTAL SETUP.....	121
APPENDIX F	123
F.1 STANDOFF DETECTION DIAGRAM	123
BIBLIOGRAPHY	124

LIST OF TABLES

Table 1.1: Raman cross sections of the explosives PETN, TNT, and RDX at different excitation wavelengths. (Table adapted from Ref. ^{8, 28}).	9
Table 3.1: Absolute differential resonance Raman cross-sections at 229 nm of TNT, 2-amino-4,6-DNT, 4-amino-2,6-DNT, 3,5-dinitroaniline, and 2,5-dinitrophenol in CH ₃ CN solution.....	41
Table 3.2: Mass chromatograms' retention times, m/z values, and identity of species formed. ..	45
Table 3.3: Resonance Raman cross-sections at 229 nm of TNT, 2-amino-4,6-DNT, 4-amino-2,6-DNT, and 3,5-dinitroaniline in the solid state.....	51
Table 3.4: Retention time, m/z, and species present for irradiated solid TNT.	52
Table 4.1: Mass chromatogram retention times, m/z values, empirical formulas, and proposed identities of the species that form a formate adduct.	66

LIST OF FIGURES

Figure 1.1: This figure represents the number of terrorist attacks worldwide and the number of attacks utilizing explosives, bombs, and dynamite (EBD) during the time period of 2004-2014. A large increase has been observed in recent years. (Figure adapted from Ref. ⁸ and ⁹).	1
Figure 1.2: Molar absorptivities of TNT, RDX, HMX, PETN in acetonitrile (CH ₃ CN) and aqueous NH ₄ NO ₃ . The samples' concentrations were 0.1 mg/mL. (Figure adapted from Ref. ³¹)	8
Figure 1.3: Raman excitation profiles for TNT, PETN, and RDX. (a) TNT absorption in CH ₃ CN and Raman cross sections, (b) PETN absorption in CH ₃ CN and Raman cross sections, and (c) RDX absorption in CH ₃ CN and Raman cross sections. (Figure adapted from Ref. ^{8,28}).	11
Figure 1.4: TNT photolysis pathways showing the numerous decomposition products that occur with irradiation from sunlight. (Figure adapted from Ref ⁵⁴).	14
Figure 1.5: TNT absorbance spectrum showing near UV absorption at $\lambda < 400$ nm.	15
Figure 1.6: Proposed mechanistic pathway for RDX photolysis in water when exposed to UV light. (Figure adapted from Ref ⁵⁹).	17
Figure 1.7: RDX absorption spectrum.	18
Figure 1.8: PETN decomposition resulting in cleavage of an O-NO ₂ bond to form NO ₂ and an alkoxy radical. (Figure adapted from Ref ⁶⁹).	19
Figure 1.9: PETN absorbance spectrum.	20

Figure 2.1: The Rayleigh and Raman scattering phenomenon. Electromagnetic radiation of a specific frequency, ν_0 , excites a molecule and light is scattered elastically (Rayleigh) and inelastically (Raman). (Figure adapted from Ref. ⁴³). 22

Figure 2.2: Raman spectra are shown for three different positions of excitation in the absorption spectrum: a) Excitation within absorbance band, b) Excitation near the absorption band, and c) Excitation away from the absorption band. Greatest Raman intensity is observed for (a) where excitation is within the absorption band leading to resonance enhancement. (Figure adapted from Ref. ⁴³). 23

Figure 3.1: A) Irradiance time dependence of DUVRR spectra. 1.5 mL of 1 mg/mL TNT in CD₃CN was irradiated with 10 mW of 229 nm UV light. The TNT spectra were normalized to the CD₃CN 2117 cm⁻¹ band intensity and the silica bands subtracted. The CD₃CN was not subtracted. The absorbed photons/molecule compared to exposure time is shown. B) TNT difference spectra (initial spectrum minus spectra irradiated for t = 30, 90, 150, 210, 270, 330, 390, 450, 510, and 570 min). Negative features result from photoproduct Raman bands. 36

Figure 3.2: Time dependence of the absorption spectra of TNT in CH₃CN after 0, 30, 210, 450, and 570 min. irradiation by 229 nm light measured in a 0.05 mm pathlength cuvette..... 38

Figure 3.3: 229 nm solution DUVRR spectra of 1 mg/mL TNT and possible photoproducts (in CH₃CN): A) TNT, B) 2,5-dinitrophenol (2,5-DNP) (in CD₃CN), C) 3,5-dinitroaniline, and D) 2-amino-4,6-dinitrotoluene, E) 4-amino-2,6-dinitrotoluene. The silica, CH₃CN, and CD₃CN contributions were subtracted. Spectra are scaled proportional to the Raman cross section (corrected for self absorption and instrument function) of the most intense band in each spectrum: 1357 cm⁻¹ band for TNT, 1149 cm⁻¹ band for 2,5-DNP, 976 cm⁻¹ band for 3,5-DNA, 1352 cm⁻¹ band for 2-amino-4,6-DNT, and the 987 cm⁻¹ band for 4-amino-2,6-DNT. 39

Figure 3.4: Absorption spectra of 1 mg/mL TNT and its putative photoproducts: 2-amino-4,6-DNT, 4-amino-2,6-DNT, 2,5-dinitrophenol (2,5-DNP), and 3,5-dinitroaniline in CH₃CN measured in a 0.05 mm pathlength cuvette..... 40

Figure 3.5: Solution TNT Raman band intensities versus irradiation time or absorbed photons per molecule..... 43

Figure 3.6: Mass spectral ion current chromatograms of TNT irradiated with 229 nm light after different irradiation time intervals. After the 15 min. spectrum, only newly eluted peaks are labeled in the 105, 225, and 285 min. spectra that are not seen in the 15 min. Table 3.2 shows the m/z for every peak in each spectrum. The number of photons per molecule at each irradiation time is labeled. 44

Figure 3.7: 229 nm solution DUVRR spectra of 1 mg/mL A) 2-amino-4,6-DNT (in CH₃CN), and B) 2,5-dinitrophenol (in water), and C) Difference spectra of TNT (in CD₃CN) at times initial minus 30 min., 90 min., 210 min., and 570 min. The quartz, CH₃CN, and CD₃CN contributions have been subtracted. Negative features in spectrum C result from photoproduct contributions. Photoproduct contributions give rise to features at ~ 1196 cm⁻¹, 1273 cm⁻¹, and ~1595 cm⁻¹. 47

Figure 3.8: A) 229 nm excited, irradiation time dependence of the DUVRR of solid state TNT on MgF₂ powder (0.06 % mass fraction TNT). B) Solid state TNT difference spectra between initial spectrum and spectra measured at = 10, 20, 30, 40, 50, 60, 90, 120, 150, and 180 sec. Negative features derive from photoproduct band contributions..... 49

Figure 3.9: 229 nm DUVRR spectra of solid TNT and its putative photoproducts on MgF₂ powder: A) TNT, B) 3,5-dinitroaniline, C) 2-amino-4,6-dinitrotoluene, and D) 4-amino-2,6-dinitrotoluene. Spectra are scaled proportional to their Raman cross sections (corrected for self absorption and instrument function) of the -NO₂ symmetric stretching band, at ~1357 cm⁻¹. 50

Figure 3.10: Time dependence of LCMS chromatograms of extracted solid TNT irradiated at 229 nm over different time intervals as monitored by their ion current. 52

Figure 4.1: a) Solution DUVRR spectra of RDX in CD₃CN with increasing irradiation (photons absorbed per molecule). 1 mL of 3 mg/mL RDX in CD₃CN was irradiated with 17 mW of 229 nm light. Quartz and CD₃CN Raman bands were subtracted. b) DUVRR spectra of the 834 cm⁻¹ CD₃CN band in the RDX spectra with increasing irradiation time. The CD₃CN band increases in intensity as the photolysis increases. 62

Figure 4.2: a) Dependence of the absorption spectra of RDX in CD₃CN upon irradiation of 0.01, 1, 2, 5, 10, 20, and 30 photons/molecule by 229 nm light measured in a 0.05 mm path length cuvette. b) Absorbance difference spectra between 1-2, 2-5, 5-10, 10-20, and 20-30 photons/molecule absorption spectra. 64

Figure 4.3: Mass spectral ion current chromatograms of RDX irradiated by 229 nm light at different irradiation times. The irradiation times are given in the number of absorbed photons/molecule. The m/z values correspond to the formate adducts. Table 4.1 indicates the proposed compounds along with their calculated m/z values. 65

Figure 4.4: GCMS of a 30 photon/molecule irradiated RDX sample. The peak at 44 m/z is indicative of formamide. 68

Figure 4.5: Solution RDX 940 cm⁻¹ and 1580 cm⁻¹ Raman bands intensity vs. absorbed photons per molecule and the 267 m/z peak intensity from the HPLC-UV versus absorbed photons/molecule. A linear fit is shown for each of the plots. 69

Figure 4.6: The RDX CD₃CN initial solution, 0.04 photon/molecule spectrum is shown in comparison to the RDX difference spectra between the minimally photolyzed 0.04 phot/molec RDX sample, and the 229 nm DUVRR spectra of RDX samples that absorbed 1, 2, 5, 10, 20, and

30 phot/molec. Negative peaks derive from photoproducts. 229 nm solution DUVRR spectrum of neat nitric acid (69 %) is also shown. The quartz and CD₃CN Raman bands were subtracted.71

Figure 4.7: Irradiation time dependence of 229 nm excited DUVRR spectra of solid state RDX on MgF₂ powder (< 1 % by weight RDX). The sample was spun during excitation and irradiated with 4.2 mW of a 229 nm CW laser beam focused to a spot size of ~200 μm..... 72

Figure 4.8: 229 nm DUVRR spectra of solid state photolyzed RDX on a SiO₂ substrate with varying irradiation times. The sample was stationary during excitation and contained ~1 mg of RDX. The sample was irradiated with 8.5 mW of a CW 229 nm laser beam focused to a spot size of ~200 μm. The 1555 and 2368 cm⁻¹ bands derive from atmospheric oxygen and nitrogen, respectively. 74

Figure 4.9: Nitrogen 1s electron XPS spectra of RDX (on a gold substrate) at different irradiation times: a) RDX with no UV irradiation, b) RDX after 5 min of UV irradiation, and c) RDX after 465 min of UV irradiation. The spectra were fit to Gaussian bands. The RDX sample was irradiated for 465 min with 5 mW of a CW 229 nm laser beam focused to a spot size of ~300 μm. 77

Figure 4.10: Carbon 1s electron XPS spectra of RDX (on a gold substrate) after different irradiation times: a) RDX without UV irradiation, b) RDX with 5 min of UV irradiation, and c) RDX with 465 min of UV irradiation. The spectra were fit to Gaussian bands. The RDX sample was irradiated for 465 min with 5 mW of a CW 229 nm laser beam focused to a spot size of ~300 μm. 79

Figure 5.1: 229 nm UVRR of PETN in CD₃CN with increasing irradiation times (absorbed photons per molec). The NO₂ in CD₃CN spectrum shows the NO₂ Raman band at 1308 cm⁻¹. CD₃CN and quartz UVRR bands were subtracted..... 88

Figure 5.2: PETN photolysis quantum yield measurements. Dependence of PETN 361 m/z peak intensity measured by HPLC-UV on the number of absorbed phot/molc during initial stages of photolysis in the absence of water. The quantum yield is determined from the slope. 90

Figure 5.3: Absorption spectra of PETN in CD₃CN (1 cm path length) upon 229 nm irradiation of 0.5, 1, 3, 5, 11, and 16 absorbed phot/molc..... 91

Figure 5.4: UVRR excited at 229 nm of NO₂ dissolved in CD₃CN with addition of 0.1, 0.5, 1, 3, 5 % volume fractions of H₂O. The spectra are normalized to the 2061 cm⁻¹ band of CD₃CN. Quartz and CD₃CN Raman bands are subtracted. This sample was also used for the absorption measurements of Figure 5.5..... 92

Figure 5.5: Absorption spectra of NO₂ dissolved in CD₃CN at increasing volume fractions of H₂O (0.1, 0.5, 1, 3, and 5 %) measured using a 1.0 cm path length cuvette. This is the same sample used for the UVRR measurements of Figure 5.4..... 94

Figure A1: MS/MS of the standard 1 mg/mL 2-amino-4,6-dinitrotoluene in CH₃CN..... 100

Figure A2: MS/MS of the standard 1 mg/mL 4-amino-2,6-dinitrotoluene in CH₃CN. The 149 m/z peak distinguishes it from its isomer 2-amino-4,6-DNT. 101

Figure A3: MS/MS of 196 m/z peak from the TNT irradiated samples, retention time of 7.1 min. 101

Figure A4: MS/MS of the standard 1 mg/mL 3,5-dinitroaniline in CH₃CN 102

Figure A5: MS/MS of 182 m/z peak from the TNT irradiated samples, retention time of 3.5 min. 102

Figure A6: MS/MS of standard 2,5-dinitrophenol in water..... 103

Figure A7: MS/MS of 183 m/z peak from TNT irradiated samples, retention time of 103

Figure A8: MS/MS of 197 m/z peak from TNT irradiated samples, retention time of 11.7 min. 104

Figure A9: MS/MS of 183 m/z peak from TNT irradiated samples, retention time 7.4 min. 104

Figure A10: Mass spectrum of initial solid TNT sample showing 226 m/z peak, 11.980 min. retention time. 105

Figure A11: Mass spectrum of the 10 min. irradiated solid TNT sample: 183 m/z peak, 10.592 min. retention time. 105

Figure A12: Mass spectrum of the 10 min. irradiated solid TNT sample: 197 m/z peak, 11.395 min. retention time. 106

Figure B1: Diffraction pattern of RDX on the SiO₂ substrate. The blue diffraction pattern is the PDF entry of α -RDX from the database. The black diffraction pattern is the raw data of the RDX on SiO₂ substrate and the red is the peaks identified by the Bruker Eva software program. There is overlap of the blue PDF entry of α -RDX from the database and the black raw data of RDX on SiO₂ substrate. 107

Figure B2: Diffraction pattern of RDX on the gold coated glass slide. The black diffraction pattern is the raw data of the RDX on SiO₂ substrate and the red are the peaks identified by the Bruker Eva software program. The contribution from the gold is labeled at ~ 38.25 degrees... 108

Figure C1: Total absorption spectrum of gaseous NO₂ measured at 298 K. [Reproduced with permission of Elsevier Sequoia.¹³³] 110

Figure C2: Absorption cross sections of gaseous N₂O₄ at 220 K. The cross sections are compared to previous work completed by Bass et al. (1976) at 250 K. [Reproduced with the permission of Kluwer Academic Publishers.¹⁴⁴] 111

Figure C3: Absorption cross sections of gaseous HNO ₂ . [Reproduced with permission from Elsevier. ¹⁵³]	112
Figure D1: Magazine containing high explosives.	114
Figure D2: Magazine containing low explosives.....	114
Figure E1: Diagram of experimental setup utilized for the photochemistry experiments.....	121
Figure F1: Diagram of the proposed rastering standoff detection setup.....	123

PREFACE

I would like to thank my advisor, Professor Sanford Asher, for all of his guidance and support throughout my years as a graduate student at the University of Pittsburgh. He taught me to be an independent scientist. I really enjoyed working for Dr. Asher and I admire his excitement towards science and research. Thank you for being a wonderful PI and teaching me to be a successful scientist.

I would also like to thank the members of the Asher group. I am thankful for meeting such a wonderful group of people that I consider to be my friends and lab family. I especially would like to thank Dr. Sergei Bykov. Sergei worked with me on the explosive photochemistry project and has taught me so much about Raman spectroscopy. I am grateful for his mentorship and friendship. I am especially grateful for my friendships with Lily Wu, Brittney Graff, and Natasha Smith. You guys are such awesome friends! I also want to thank Sharon Mansfield for being such a wonderful and caring person. I am so grateful for our friendship. And I want to thank her for always being there to help and give advice.

I would like to acknowledge my thesis committee for their guidance and mentorship, specifically Dr. Garrett-Roe, Dr. Waldeck, and Dr. Chen.

I would like to thank my family. For my parents, Donna and Larry Johnson, who have always believed in me and taught me to reach for my dreams. Without them I would not be the person I am today or have gotten where I am today. Their support and love is tremendous and I

am so thankful to have them as my parents. I would like to thank my brother, Clinton Johnson. I am so grateful to be able to share the love of chemistry with him. He is always there when I need him for help with my science or things in life.

Finally, I want to thank my wonderful husband, Daniel. Thank you for always believing in me and always being there for me. Your support and love is amazing and I could not have accomplished what I have without you. Thank you to my adorable and loving puppy Bimmer who always makes me happy and is always there for me. I also want to thank my son Carter for inspiring me to be the best I can be for him. I can only hope to be a great role model for you and teach you to love science like I do. I hope that one day you will reach all of your dreams and know that anything is possible.

1.0 INTRODUCTION

1.1 EXPLOSIVE DETECTION

The use of improvised explosive devices (IEDs) in terrorist attacks has substantially increased.¹⁻⁷

Figure 1.1 shows the increase in the number of terrorist attacks worldwide. Developing methods for detecting explosives has become an important area of research as a result of the increase level of terrorist attacks.¹⁻⁷ Explosive detection methods should be able to detect and identify the explosives.

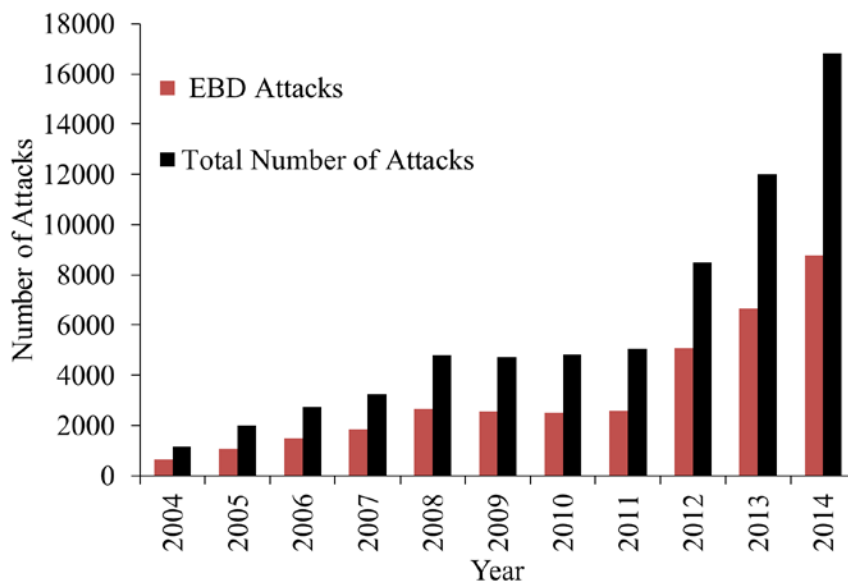


Figure 1.1: This figure represents the number of terrorist attacks worldwide and the number of attacks utilizing explosives, bombs, and dynamite (EBD) during the time period of 2004-2014. A large increase has been observed in recent years. (Figure adapted from Ref. ⁸ and ⁹).

IEDs are one of the primary threats used in terrorist attacks.^{5, 10} There are different types of explosives that are used in these IEDs. Some of the main military explosives that need to be detected are HMX (cyclotetramethylene-tetranitramine), RDX (cyclotrimethylenetrinitramine), PETN (pentaerythritol tetranitrate), and TNT (trinitrotoluene). Military explosives often contain $-NO_2$ groups such as O- NO_2 groups in the nitrate esters of PETN, C- NO_2 groups in the nitroaromatics such as TNT, and N- NO_2 groups in the nitramines such as RDX and HMX.^{8, 11} Plastic explosives have also become widely used in terrorist bombings.¹¹ These plastic explosives consist of C-4 (RDX and plasticizers) and Semtex-H (RDX and PETN). More recently peroxide based explosives have become more prevalent in terrorists attacks.^{3, 11} These peroxide compounds are triacetone triperoxide (TATP) and hexamethylene triperoxide diamine (HMTD). These compounds can be readily made from materials that are easy to obtain and are relatively cheap in cost.^{3, 11} The peroxide compounds are very unstable due to the O-O bond which can rapidly oxidize and cause them to explode.^{3, 11}

Improved methods for detecting explosives at security check points, at government buildings, and/or at airport screening check points are needed. At airports, detecting explosives inside luggage or as residues on people's hands or clothing is extremely important.⁷ Furthermore, photochemistry will impact detection of explosives. Explosives will absorb UV light and photodegrade into multiple photochemical products, which sometimes hinders the detection of the explosive molecule. Therefore, it is imperative to understand the photochemistry of explosives.

1.1.1 Non Standoff Detection Methods

Numerous detection methods utilizing different chemical techniques exist for detecting explosive compounds. The non-spectroscopy methods of detection consist of canine olfaction, ion mobility mass spectrometry, and colorimetric and fluorimetric methods. Canine olfaction is one of the most widely used methods for detecting explosives.¹² Canine olfaction offers sensitivity and specificity, but there are numerous challenges in detecting explosives using canines.⁸ It is uncertain if the canines are sensing the specific analyte of interest or if they are sensing impurities in the explosive sample.³ Furthermore, canines are only able to work for a few hours in a day.^{8, 13}

Ion mobility spectrometry (IMS) is the analytical technique used for detection of explosives in airports worldwide.¹⁴ This method consists of swabbing the surface of a suspected explosive area and then rapidly heating this sample to analyze any adsorbed volatile explosive species.¹⁴ The IMS instrument consists of a sample inlet system along with an atmospheric pressure ion source.¹⁴ IMS is one of the most popular portable and commercial techniques for detection of explosives; however it is challenged by many obstacles. IMS is not ideal for standoff detection since ions need to be physically drawn into the spectrometer.⁸ Many explosives have extremely low vapor pressures (ppb), therefore making it difficult to detect trace explosive vapors using IMS. IMS also has challenges with distinguishing analytes from environmental interferences and produces false alarms from molecules that are not explosives.¹⁴

Another common detection method is colorimetric sensors. Colorimetric sensors are easily portable and allow for easy interpretation and rapid detection. Colorimetric methods typically use chemistries such as the Griess or Meisenheimer reactions which produce brightly colored compounds for detection of nitrite (NO_2^-) or nitroaromatics, respectively.¹⁵ The Griess

reaction is widely used to detect NO_2^- from nitrate esters and nitramines such as PETN and RDX, for example.¹⁶ The Griess reaction consists of a nitrate ester or nitramine that is treated with base to produce NO_2^- .¹⁵ This is then treated with sulfanilamide, which under acidic conditions will form a diazo intermediate compound.¹⁵ This intermediate compound is then reacted with an arylamine to produce a bright pink colored azo dye that gives visual detection of PETN, RDX, HMX, nitroglycerin, or nitrocellulose.^{15, 16}

The Meisenheimer reaction is used for detection of nitroaromatics such as TNT, and dinitrotoluene (DNT).^{15, 16} The aromatic ring of these compounds reacts with a strong nucleophilic base to produce the brightly colored Meisenheimer complex for visual detection of the nitromatics.^{15, 16} These reactions have been utilized in commercial spray can kits for detection of explosives.¹⁶ The colorimetric methods are inexpensive and easy to use for personnel in the field; however, they lack specificity and are known to give false positives.

Fluorescence quenching is another technique used for explosive detection assays. This technique involves using electron rich conjugated polymer systems which contain fluorophores for the explosive analytes to bind to.¹⁵ Commercial fluorescence detection based sensors have been developed and utilized for military use, such as the FIDO system demonstrated by Cumming et al.¹⁷ Fluorescence methods are only specific to one class of explosives, nitroaromatics, and cannot detect nitramines or other types of explosives.¹⁵ These methods are not suitable for standoff detection.

1.1.2 Standoff Detection Methods

Laser based spectroscopy methods are being investigated for standoff detection purposes. These methods involve interrogation the surface with a laser at a standoff distance. The scattered light

is then collected to obtain information about the explosive molecule being detected. Standoff spectroscopies have been successfully demonstrated at tens to hundreds of meters.^{8, 18, 19} Standoff spectroscopy methodologies utilize instrumentation that can analyze and scan an area for threat molecules. Chemical imaging can also be implemented in these spectroscopic methods.⁸

Laser-induced breakdown spectroscopy (LIBS) has recently been utilized for standoff detection of explosives.^{20, 21} LIBS uses short, high peak power lasers to ablate the sample which results in a plasma formation and rapid heating.^{20, 21} LIBS uses the light emitted from the laser generated plasma to determine the makeup of the sample through the emission lines of elements and molecules from the sample.²¹ When the material is ablated by the plasma spark, they decompose into smaller molecular, ionic, and atomic species.⁸ These species are then excited by the plasma and emit at characteristic specific wavelengths before relaxing. LIBS can rapidly analyze bulk materials and has therefore been recently explored for standoff detection of explosives. LIBS can analyze a broad range of materials at long standoff distances.^{20, 21} LIBS has been demonstrated to successfully detect TNT, RDX, and C-4 deposited on a car door 30 m away.²²

LIBS is not ideal for trace detection of explosives since it will ablate trace amounts of sample making it difficult to identify the explosive present. LIBS instruments are not eye safe due to the use of high power laser pulses. LIBS utilizes the carbon, hydrogen, nitrogen, and oxygen emission lines to identify an explosive; however, the atomic emission lines do not give specific information on the stoichiometry to identify the molecular structure as easily as other techniques. The matrix/background emission lines from organics and atmospheric gases can also make it difficult to identify the explosive molecule in the LIBS spectrum.

There have also been groups that have investigated using nonlinear Raman spectroscopy techniques for standoff detection of explosives such as coherent-anti Stokes Raman spectroscopy (CARS).²³⁻²⁵ CARS traditionally uses two laser beams to excite the sample. The pump and probe is generated from one laser beam and interacts with the Stokes field of the other laser beam.²⁶ This generates anti-Stokes scattered light.²⁶ CARS has the advantage of Raman spectroscopy with unique vibrational spectra that can identify explosive molecules; however, CARS is challenging for standoff detection because of having to overlap several laser beams from several sources.²⁵ Recently, groups have utilized ultrashort femtosecond laser pulses to simultaneously provide the pump, probe and Stokes photons, which simplifies the phase matching of multiple beams.²⁵ Natan et al. have demonstrated single beam CARS detection of nitrate, RDX, and urea at 12-50 m distances.²⁵ CARS standoff detection methods have expensive laser costs and are not eye safe since ultrafast laser pulses are used.

1.1.3 Raman Spectroscopy for Detection of Explosives

Raman spectroscopy has been widely used as a standoff detection method.^{3, 4, 8, 27-33} Raman spectroscopy is a successful detection method since it can detect unique vibrational signatures of explosive molecules. Raman spectroscopy involves utilizing a laser source to irradiate a surface and the Raman scattered light is then collected and analyzed. Raman spectra give details about the structure of the molecule, which are useful for the detection of specific molecules. Raman spectra can be used as specific fingerprints to determine the chemical composition of the explosive molecule.

Carter et al. and Sharma et al. demonstrated the first standoff Raman detection of explosives in the early 2000's.^{34, 35} The Raman instrument Carter developed utilized a Nd:YAG

532 nm laser as the excitation wavelength and detected explosives at a 50 m distance. A telescope collected the Raman scattered light. The explosives detected were TNT, RDX, PETN, and NH_4NO_3 . Östmark et al. recently demonstrated a standoff visible Raman imaging instrument that detected solid chunks of DNT, NH_4NO_3 , and TNT at a 10 m standoff distance utilizing 532 nm excitation.³⁶ Standoff visible Raman spectroscopy is used for detection of bulk explosives.

Trace detection of explosives is a challenge for normal Raman spectroscopy. This is due to the typically small, normal Raman cross sections when exciting samples with visible light. There is also a large component of sample and background fluorescence, which will cause difficulty in distinguishing the molecule's Raman bands from the background fluorescence. The fluorescence also affects signal to noise (S/N) of the spectra being collected. Visible Raman is also not selective for explosive analytes. The visible Raman bands of the explosives will have similar cross sections to the Raman bands of substrates and environmental interferences making it difficult for detection. Therefore, UV Resonance Raman spectroscopy has been recently demonstrated as a promising technique for detection of trace amounts of explosives at standoff distances.

1.1.4 UV Resonance Raman Spectroscopy for Detection of Explosives

UV resonance Raman spectroscopy has been proven to be a successful technique for standoff detection of trace explosives.^{8, 27, 28, 31, 33, 37-42} Most explosives absorb in the deep UV at wavelengths < 260 nm.^{28, 31} Exciting explosive analytes in the deep UV results in increased spectral sensitivity and selectivity due to the ν^4 dependence of the scattered intensity.^{43, 44} The lack of competing fluorescence at $\lambda < 260$ nm also contributes to an increase in spectral (S/N).^{43, 44} The Raman intensities will be increased for molecules that absorb at or near the excitation

wavelength. UVRR can be used for detection of photochemical products to monitor the time dependent spectral changes resulting from photolysis. We have estimated a detection limit of $\sim 1 \mu\text{g}/\text{cm}^2$ for PETN and ammonium nitrate films utilizing UVRR, as demonstrated by Hufziger et al.³³

Trace detection of explosives is optimized through the use of excitation wavelengths that resonantly enhance the Raman spectra of an explosive molecule. Figure 1.2 shows the absorption spectra of multiple explosives.

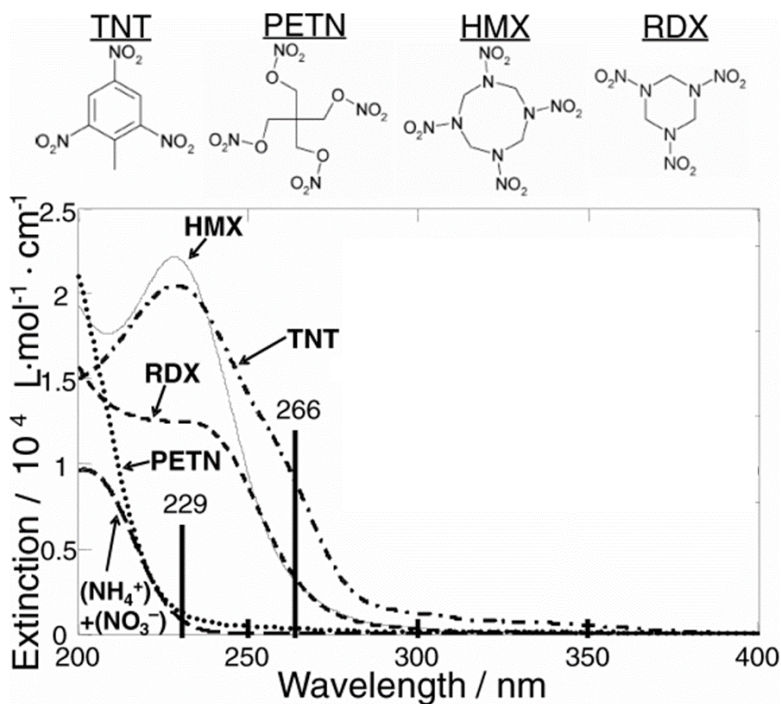


Figure 1.2: Molar absorptivities of TNT, RDX, HMX, PETN in acetonitrile (CH_3CN) and aqueous NH_4NO_3 . The samples' concentrations were 0.1 mg/mL . (Figure adapted from Ref. ³¹)

All of these explosives show absorption bands below $\lambda < 260 \text{ nm}$.^{28, 31} In this Thesis, we will focus on TNT, RDX, and PETN. TNT and RDX absorption maximum is $\sim 229 \text{ nm}$. PETN has deep UV absorption with a maximum at $\sim 200 \text{ nm}$. Exciting these explosives with 229 nm light will yield the largest resonance enhancement. Photochemistry will also occur when these

explosives are excited with UV light. Therefore, examining the photochemistry is important for enabling trace detection of these explosives.

The RDX and TNT absorptions derive from the π - π^* transitions of the nitro groups (-NO₂).^{8, 31} PETN absorption results from π - π^* transitions localized on the O-NO₂ groups. By utilizing excitation wavelengths in the deep UV, Raman spectral intensities of the explosives will be increased. This will enable detection of trace amounts of explosives and their photochemical products.

In addition, Raman cross sections for these explosives have been measured.^{28, 31, 45-47} The spontaneous Raman cross section indicates the efficiency of Raman scattering for a specific molecule. Excitation within a specific electronic absorption band leads to an increase in the Raman cross section for that molecule. Table 1.1 lists the Raman cross sections of PETN, TNT, and RDX in CH₃CN for excitation wavelengths between 204 and 257 nm.^{8, 28, 31} These deep UV Raman cross sections are roughly three orders of magnitude larger than those for visible excitation.³¹

Table 1.1: Raman cross sections of the explosives PETN, TNT, and RDX at different excitation wavelengths. (Table adapted from Ref. ^{8, 28}).

Explosive	Raman bands/cm ⁻¹	204 nm Raman cross-sections/10 ⁻²⁶ cm ² ·molc ⁻¹ ·sr ⁻¹	229 nm Raman cross-sections/10 ⁻²⁶ cm ² ·molc ⁻¹ ·sr ⁻¹	244 nm Raman cross-sections/10 ⁻²⁶ cm ² ·molc ⁻¹ ·sr ⁻¹	257 nm Raman cross-sections/10 ⁻²⁶ cm ² ·molc ⁻¹ ·sr ⁻¹
PETN	1294	29.8	1.8	0.30	0.26
	1658	13.3	1.4	0.12	0.12

TNT	1209	1.5	5.8	1.5	1.9
	1354	9.8	65.4	28.5	41.6
	1616	4.9	33.0	13.3	21.4
RDX	1270	13.0	6.8	2.7	2.1
	1314	13.9	3.0	0.07	1.3
	1586	4.2	5.5	1.7	0.71

Resonance Raman excitation profiles were also determined for these explosives.^{28, 31} The resonance Raman excitation profiles typically track the square of the absorption molar absorptivities.³¹ The excitation profiles for each explosive indicate the excitation wavelength that results in the greatest resonance enhancement of the Raman bands' for each explosive analyte.

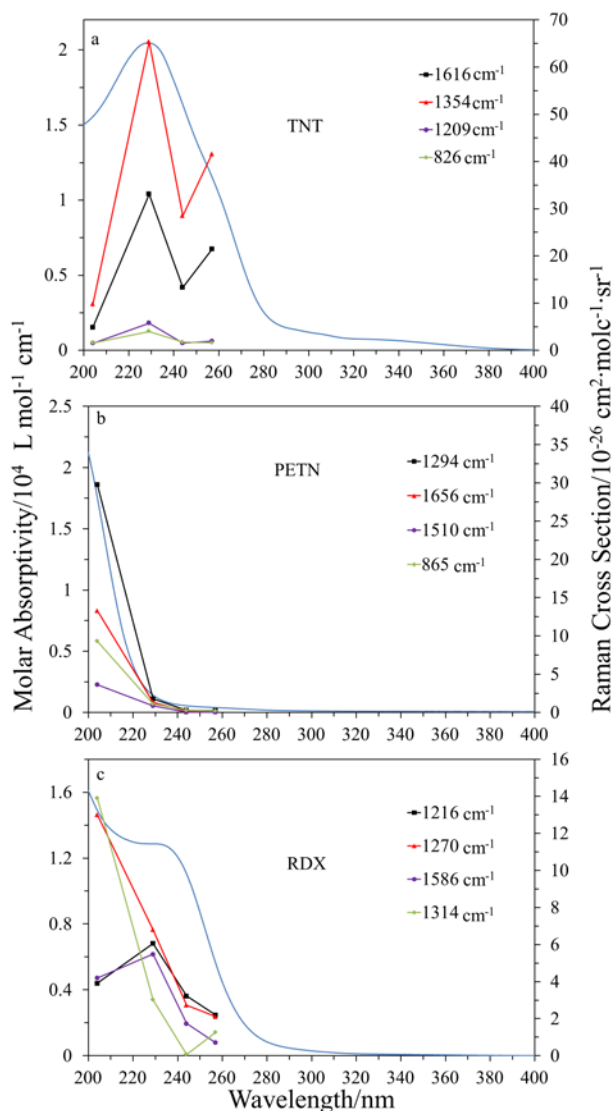


Figure 1.3: Raman excitation profiles for TNT, PETN, and RDX. (a) TNT absorption in CH_3CN and Raman cross sections, (b) PETN absorption in CH_3CN and Raman cross sections, and (c) RDX absorption in CH_3CN and Raman cross sections. (Figure adapted from Ref. ^{8,28}).

Figure 1.3 shows the PETN, TNT, and RDX Raman excitation profiles. Figure 1.3a shows that the PETN maximum absorption is also $\sim 200 \text{ nm}$ indicating its largest cross section occurs with excitation $\sim 204 \text{ nm}$.²⁸ TNT shows an absorption maximum at $\sim 229 \text{ nm}$ and the largest Raman cross section is observed at this wavelength. The excitation profile of TNT roughly tracks the square of the absorption spectrum.³¹ RDX shows absorption bands below

~200 nm and at ~230 nm.³¹ Excitation ~230 nm gives rise to the largest Raman cross sections for the 1216 and 1586 cm^{-1} Raman bands of RDX.³¹

Figure 1.3 also demonstrates that each explosive will have optimal excitation wavelengths that will give the greatest resonance enhancement; however adjacent excitation wavelengths will also give rise to resonance enhancement. We would expect to observe a similar photochemistry with excitation of these adjacent wavelengths, since excitation will involve similar electronic π - π^* transitions of the nitro groups on the explosive molecules.

UV excitation within the absorption bands of explosives will maximize the Raman cross section which is vital for detection of these explosives; however, UV excitation also causes photolysis which decreases the explosive molecule's concentration. This causes the explosive's UVRR band intensities to decrease. The photoproducts formed may also absorb deep UV light. Fundamentally understanding the photochemistry is imperative for detection of explosives and their photoproducts. Photolysis will hinder detection of the explosive analyte. Photoproducts will have UVRR bands that need to be identified. Identifying the photoproduct UVRR bands will allow for identification of the explosive even after it has been photolyzed.

1.2 PHOTOCHEMISTRY OF EXPLOSIVES

Photochemical reactions can be initiated by the absorption of electromagnetic radiation.⁴² Electronically excited states are produced from the absorption of a photon. Photochemical reactions and chemical changes to the molecule occur during the absorption of electromagnetic radiation. Photodegradation is a process where the analyte molecule is degraded and undergoes

chemical changes to form photoproducts. Photodegradation can occur when the molecule is exposed to ultraviolet (UV) or visible light.⁴⁸

Experimentally, photochemical reactions are examined in order to determine photoproducts formed, the overall rate of the reaction, and the quantum yield.⁴⁸ Over the course of the photochemical reaction, the reactants will decrease in concentration while the products increase in concentration. Lasers are commonly used as excitation sources for photodegradation measurements.

The quantum yield is used to describe the behavior of a photochemical process.⁴⁸ The quantum yield (Φ) measures the efficiency of a photochemical reaction. The quantum yield of a photochemical reaction can be defined as the number of photochemical events that form products divided by the number of photons absorbed. The following equation describes the overall quantum yield:⁴⁹

$$\Phi = \frac{\text{number of molecules of reactant consumed}}{\text{number of photons absorbed by reactant}} \quad (1.1)$$

Photochemistry will also impact the resonance Raman spectra observed for explosives. During the Raman scattering process the explosive analytes will cycle through their electronic excited states multiple times.⁵⁰ The explosive analyte will undergo photolysis during this cycling and decrease in concentration. New photochemical species will be formed during photolysis. Characteristic spectral changes due to photoproduct formation and the decrease in analyte concentration will be observed in the UVRR spectra. These characteristic spectral changes can be used to identify the presence of a specific explosive. Standoff detection measurements will be affected by photochemistry.^{8, 37-39, 42, 50-60} Explosives will photodegrade when exposed to UV irradiation.^{8, 52, 54, 57} Examining the photochemistry is crucial for standoff detection of explosives.

1.2.1 TNT Photochemistry

The photolysis of TNT in both the solution and solid state has been widely studied to determine the photoproducts of TNT when exposed to UV light.^{39, 54, 57, 61-63} TNT photodegrades upon exposure to near UV (<400 nm) irradiation and forms numerous photoproducts from multiple reaction pathways as studied by Clark and Kunz et al (Figure 1.4).^{54, 57} The photolysis reaction pathways shown in Figure 1.4 will occur when TNT is irradiated with near UV light.

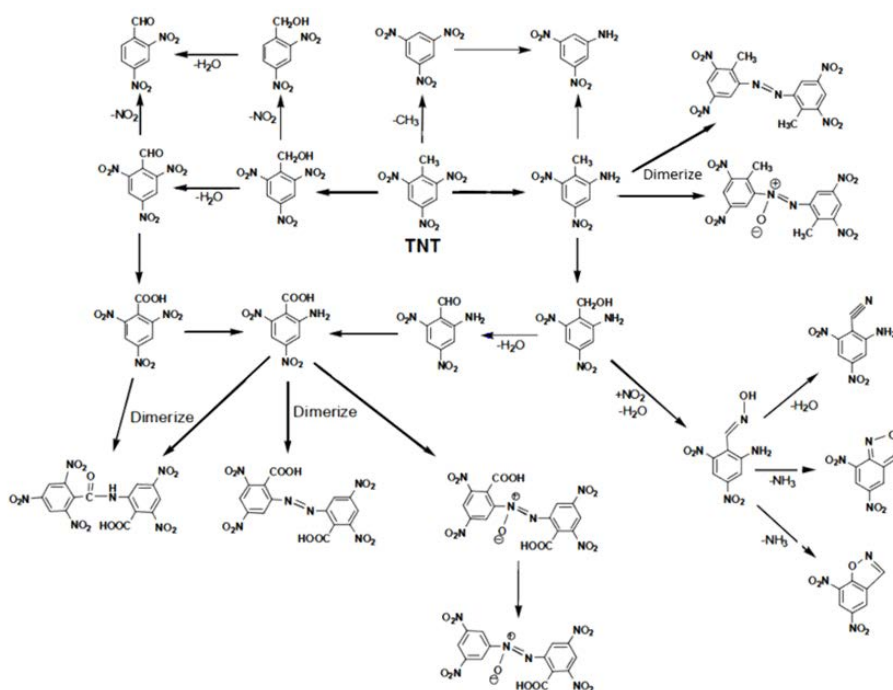


Figure 1.4: TNT photolysis pathways showing the numerous decomposition products that occur with irradiation from sunlight. (Figure adapted from Ref⁵⁴).

Clark and Kunz et al. investigated solid samples of TNT that were exposed to ~ 100 hours of sunlight.^{54, 57} These samples were analyzed for photoproducts by using gas chromatography and direct analysis in real time (DART) mass spectrometry. The samples of TNT that were exposed to sunlight changed color from an initial light yellow to a dark red-brown color indicating the formation of photoproducts. It is hypothesized that the red-brown color

indicates the formation of dimers, trimers, and oligomers linked with azo and azoxy (-N=N-) molecular linkages.⁵⁴ Figure 1.4 shows the photolysis scheme observed from these studies. These results are important for standoff detection where traces of TNT in the field could be exposed to sunlight and form these photolysis products. Understanding the photochemistry of TNT will aid in detection of TNT and its photoproducts.

TNT photolysis has also been investigated previously because of the toxicity of TNT and its photoproducts which have been observed in waste water from manufacturing plants resulting in polluted waters. TNT in aqueous solutions when exposed to sunlight is initially a light pink color, referred to as “pink water.” The TNT “pink water” solution will gradually become a rusty, orange color after long sunlight irradiation periods.^{61, 62} This photolysis has been studied previously to determine the composition of the photoproducts of TNT to help with determining the toxicity of the water and to determine how to inhibit the formation of this “pink water.”

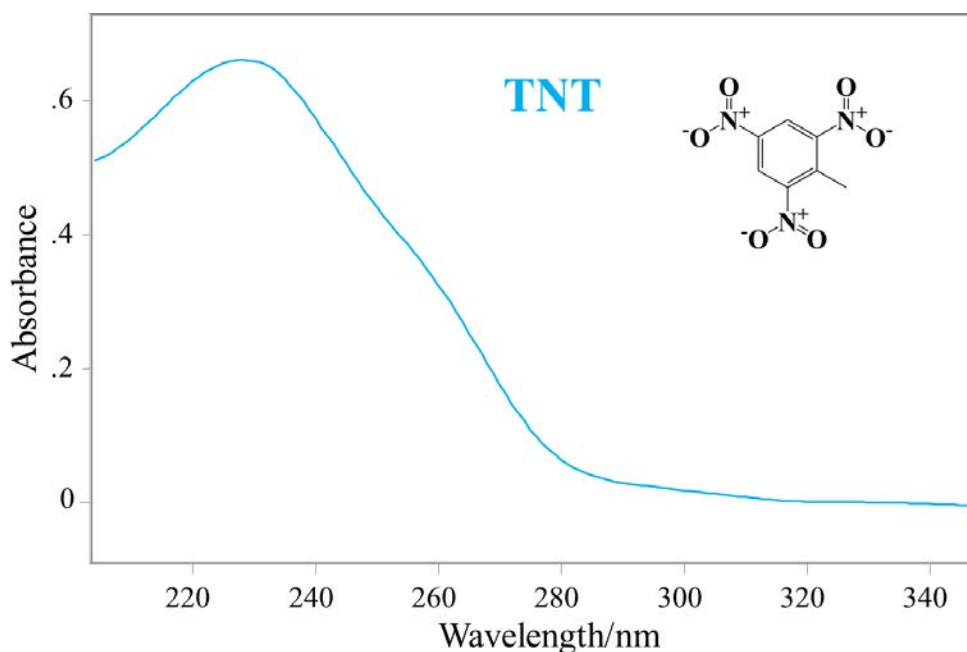


Figure 1.5: TNT absorbance spectrum showing near UV absorption at $\lambda < 400$ nm.

We have studied TNT photolysis in the deep UV exciting with 229 nm light.³⁹ TNT absorbs in the deep UV (Figure 1.5).³⁹ The photolysis of TNT is complex and consists of numerous photoproduct pathways. Upon UV photolysis, TNT's aromatic ring stays intact and substitution reactions occur on the aromatic ring to form amines, hydroxyl groups and carboxylic acid group. After long irradiation periods dimers, trimers, and oligomers form.

1.2.2 RDX Photochemistry

RDX undergoes photolysis when exposed to UV light in both the condensed and gas phases.^{38, 55, 56, 59, 60, 64-66} The initial stages of RDX photolysis in both the condensed and gas phases involve a N-N bond scission that generates neutral NO₂.^{38, 59, 60, 64-66} The mono-, di-, and tri-nitroso derivatives of RDX are formed in the condensed phase photolysis.⁵⁹

RDX UV photolysis has been previously studied for application in treating RDX waste water contamination.⁵⁹ RDX enters the waste streams during munitions loading at manufacturing plants.⁵⁹ Groups have studied how UV irradiation will convert RDX in wastewater to small organic compounds such as formaldehyde and formic acid, as well as, nitrate and nitrite compounds.⁵⁹ This method of photolyzing RDX with UV light into these smaller compounds is being used to deplete the RDX contaminants in waste streams. Peyton et al. constructed the pathway of RDX photolysis in water as shown in Figure 1.6.

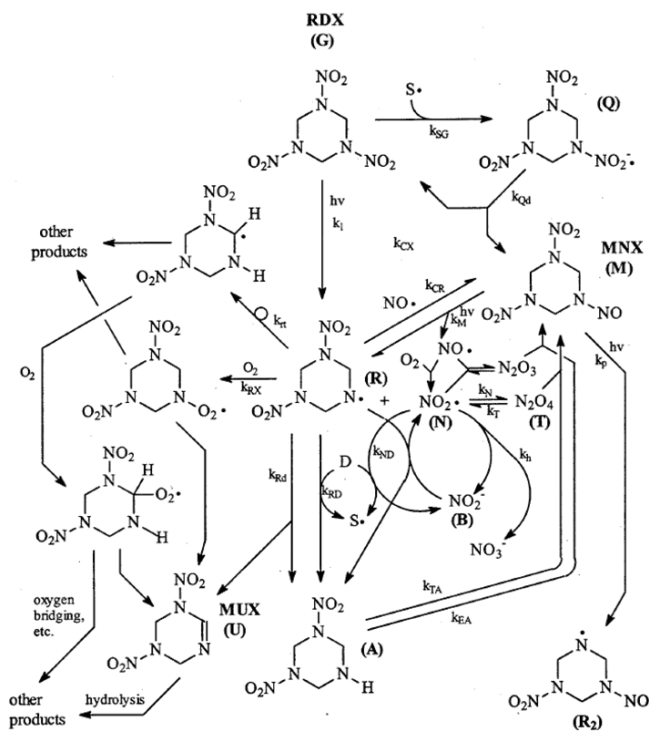


Figure 1.6: Proposed mechanistic pathway for RDX photolysis in water when exposed to UV light. (Figure adapted from Ref⁵⁹).

The proposed photochemical pathway is initiated by the scission of the N-N bond forming a nitrogen centered aminyl radical and NO₂.⁵⁹ Amine compounds are formed and nitrosated by N₂O₃ and/or N₂O₄ yielding the mono-nitroso derivative (MNX).⁵⁹ The di- and tri-nitroso derivatives of RDX can also be formed through analogous reactions during the photolysis. These photolysis experiments were performed with UV mercury lamps at ~254.7 nm.⁵⁹

RDX UV photolysis has also been studied in the gas phase using femtosecond laser pump-probe techniques and matrix-assisted laser desorption (MALDI) by Bernstein et al.^{55, 56, 65} These results showed formation of gaseous photoproducts such as nitrogen oxide (NO). Gaseous products such as NO, N₂O, HCN, and formaldehyde have also been observed in gas phase RDX photolysis.^{55, 60, 65}

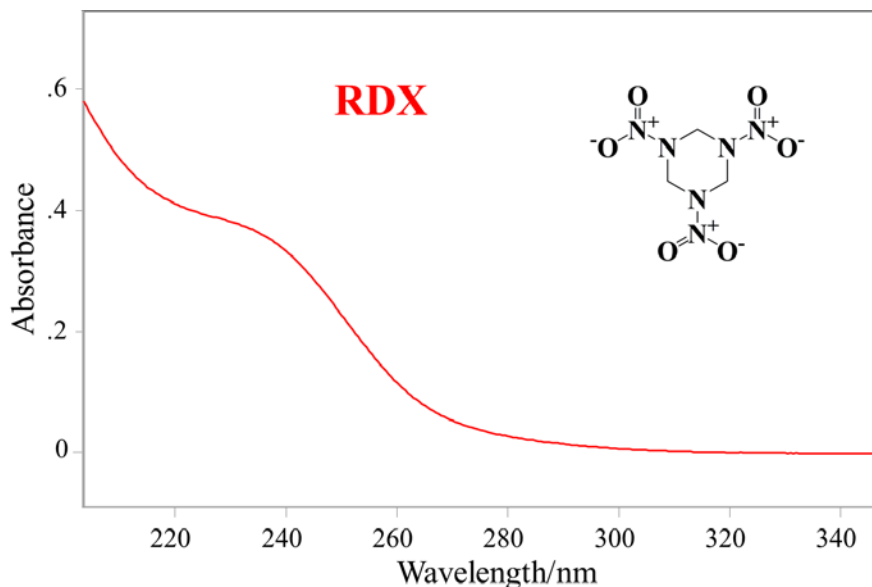


Figure 1.7: RDX absorption spectrum.

We studied RDX in the deep UV at 229 nm and observed the initial photolysis step as the scission of the N-N bond. We also observe the formation of the nitroso derivatives, as well as nitrate forming in solution state. RDX absorbs in the UV as shown in Figure 1.7, indicating it will photodegrade when exposed to UV light. RDX photolysis is complex with multiple reaction pathways occurring and numerous photoproducts that form.

1.2.3 PETN Photochemistry

Photolysis of nitrate esters has been studied in detail in the gas phase for atmospheric chemistry studies.⁶⁷ This work motivated the need to characterize nitrogen oxides formed during atmospheric chemistry.⁶⁷ These studies used excitation wavelengths >290 nm, which is an area of very weak absorption for PETN. Exciting nitrate esters at $\lambda > 290$ nm, involves cleavage of the O-NO₂ bond to form NO₂ and an alkoxy radical as photolysis products.⁶⁷⁻⁷¹ The photolysis of gas

phase nitrate esters forms nitrogen oxides in the gas phase. This gas phase photolysis is similar to the thermal decomposition of PETN which has been studied in detail.^{69, 72-75} Thermal decomposition involves cleavage of the O-NO₂ bonds of PETN. Gaseous products such as NO, NO₂, N₂O, and CO are formed in the thermal decomposition.

In general, it is known that decomposition of primary and secondary aliphatic nitrate esters (PETN) involves cleavage of the O-NO₂ bond to form an alkoxy radical and NO₂ (Figure 1.8).^{69, 75}

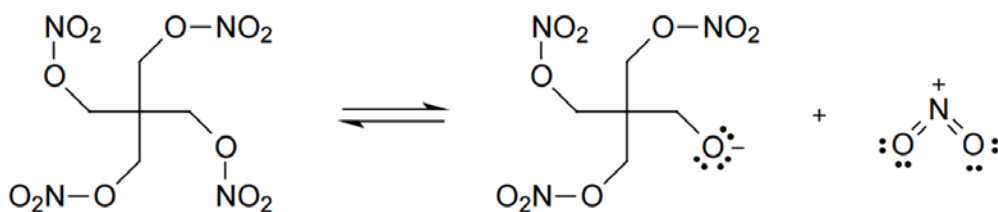


Figure 1.8: PETN decomposition resulting in cleavage of an O-NO₂ bond to form NO₂ and an alkoxy radical. (Figure adapted from Ref ⁶⁹).

There are multiple decomposition routes that can occur after the initial step. These can involve the NO₂ attacking the PETN or alkoxy radical to form other products.⁶⁹ The alkoxy radical can be oxidized by NO₂ forming products such as peroxides, nitrates, or aldehyde groups in place of the radical.⁶⁹

We studied PETN photolysis in the deep UV and observe similar decomposition routes of cleavage of an O-NO₂ bond and formation of NO₂. Figure 1.9 shows the absorption of PETN in the deep UV.

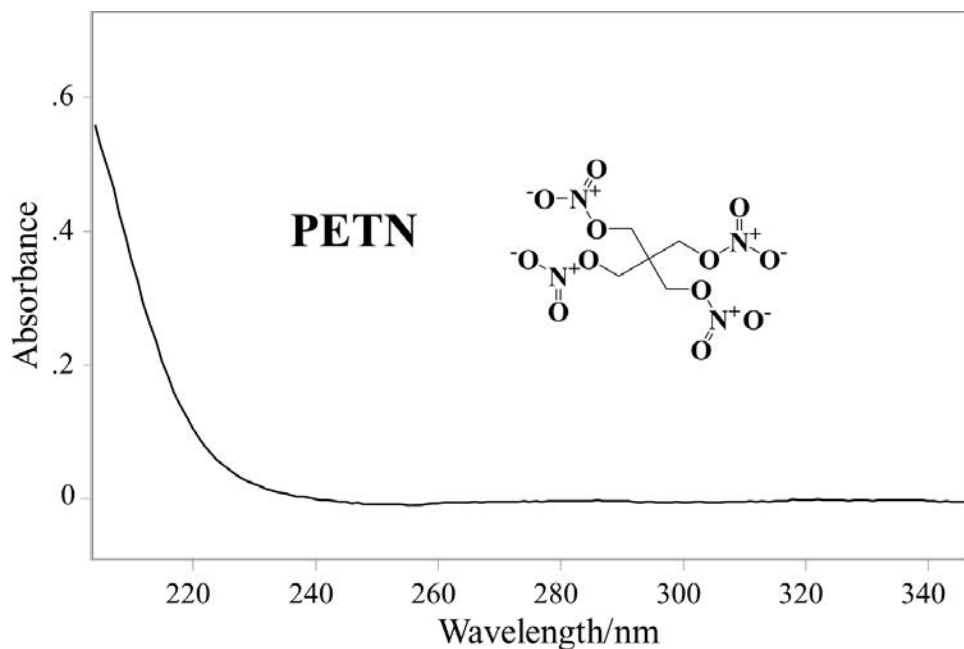


Figure 1.9: PETN absorbance spectrum.

We assume that the tail of the absorption band excited with $\lambda > 290$ nm light will involve the same electronic transition that peaks at ~ 200 nm.⁵⁰ The PETN 229 nm excitation photochemistry and the atmospheric photochemistry at $\lambda > 290$ nm have identical mechanisms and photoproducts.⁵⁰

2.0 THEORY OF RAMAN SCATTERING

2.1 INTRODUCTION

Electromagnetic radiation excites a molecule and causes its electron cloud to oscillate at the frequency of the incident light and in turn causes a charge displacement inducing a change in the dipole moment of the molecule. The charge is accelerating causing it to radiate energy in the form of light.⁴³ Light is elastically scattered if the radiated light occurs at the same frequency as the incident electromagnetic radiation. This phenomena is called Rayleigh scattering. Figure 2.1 shows that some of the light from the excited molecule is inelastically scattered. This inelastically scattered light is at a shifted frequency from the incident light due to coupling of nuclear vibrational motions and the motion of oscillating electrons.⁴³ This coupling results in a beat frequency ($\nu_0 \pm \nu_v$) which is Raman (inelastic) scattering.⁴³ Raman scattered light can be shifted to lower ($\nu_0 - \nu_v$) or higher ($\nu_0 + \nu_v$) frequencies with respect to the incident frequency of the electromagnetic radiation. The light that is scattered at lower frequencies is called Stokes Raman scattering and the light that is scattered at higher frequencies is called anti-Stokes Raman scattering. Under normal conditions Stokes scattering is much stronger than anti-Stokes scattering because molecules are typically in their ground states before excitation. Therefore, Stokes scattering is more widely used in Raman scattering experiments.

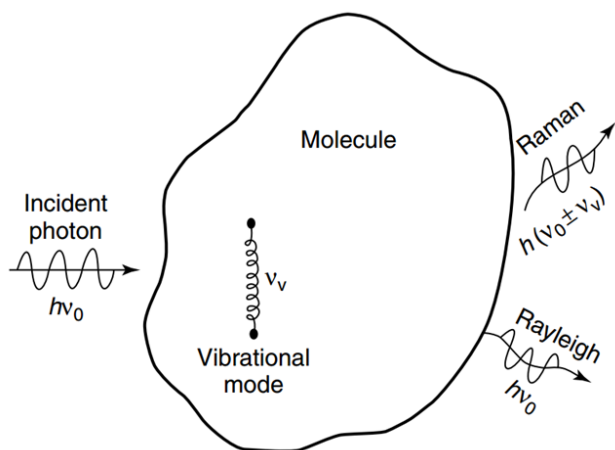


Figure 2.1: The Rayleigh and Raman scattering phenomenon. Electromagnetic radiation of a specific frequency, ν_0 , excites a molecule and light is scattered elastically (Rayleigh) and inelastically (Raman). (Figure adapted from Ref. ⁴³).

Resonance Raman scattering occurs when the exciting radiation is within the electronic absorption bands of molecules. When the excitation is within the electronic absorption band, there is an increased induced dipole moment and an increase in Raman scattering. This results in enhancement factors for resonance Raman with $\sim 10^8$ more scattering than in normal Raman.⁴³ Another advantage for resonance Raman scattering is that only the vibrations that couple most efficiently to the electronic transition being excited in the molecule will be observed in the resonance Raman spectra. This allows for unique spectral selectivity utilizing resonance Raman compared to normal Raman. The excitation wavelength can be varied to lie within a specific absorption band and therefore selectively enhance a specific vibration of a chromophore in a molecule.⁴³ Figure 2.2 shows the selectivity utilizing resonance Raman.⁴³

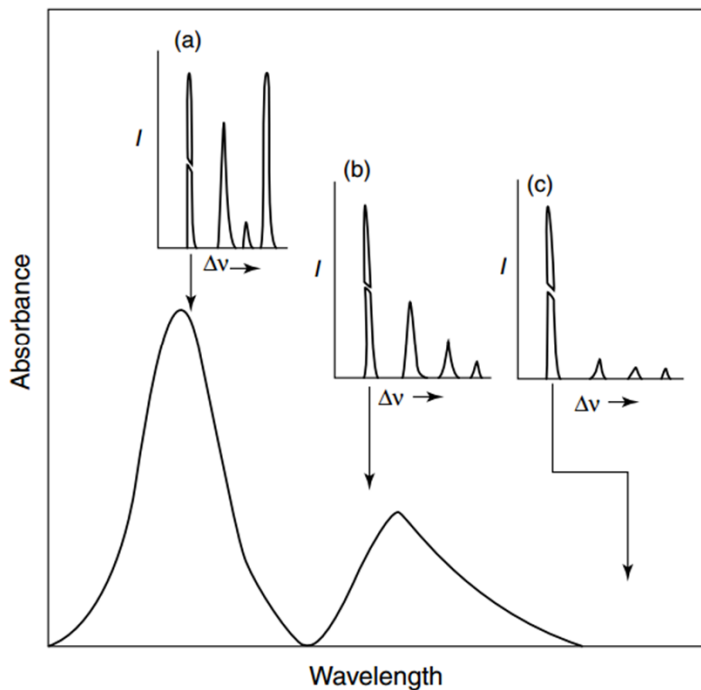


Figure 2.2: Raman spectra are shown for three different positions of excitation in the absorption spectrum: a) Excitation within absorbance band, b) Excitation near the absorption band, and c) Excitation away from the absorption band. Greatest Raman intensity is observed for (a) where excitation is within the absorption band leading to resonance enhancement. (Figure adapted from Ref. ⁴³).

Figure 2.2a shows that excitation within the absorption band or electronic transition of a molecule leads to the greatest resonance enhancement of the Raman bands. This selectivity simplifies the resonance Raman spectra, with fewer Raman bands, compared to non-resonance Raman. This is particularly useful for detection of explosives since the excitation wavelength will be tuned to the absorption band of the explosive allowing for enhancement in the resonance Raman spectra. This allows for increased selectivity and sensitivity with increased Raman intensities. The increased selectivity and sensitivity allows for trace detection of explosives and their photochemical products.⁸

2.2 CLASSICAL DESCRIPTION OF THE RAMAN EFFECT

A basic description of the Raman effect can be described using classical theory.⁷⁶ The induced dipole moment μ depends on the molecular polarizability, α , and the electric field, E .

$$\mu = \alpha E \quad (2.1)$$

Oscillating electric dipoles in the molecule are induced by the incident electromagnetic radiation (excitation) thus creating scattered light. The electric field of incident radiation oscillates at a frequency, ω_o , with an amplitude, E_o .

$$E = E_o \cos \omega_o t \quad (2.2)$$

In the scattering event, the molecule vibrates causing nuclei to be displaced from their equilibrium positions. Thus, the polarizability changes due to the vibrations of the molecule. The change in the polarizability tensor can be expressed as a Taylor series with respect to the normal coordinates of the vibration.

$$\alpha_{\rho\sigma} = (\alpha_{\rho\sigma})_o + \sum_k \left(\frac{\partial \alpha_{\rho\sigma}}{\partial Q_k} \right)_o = \alpha_o + \alpha'_k Q_k \quad (2.3)$$

The $(\alpha_{\rho\sigma})_o$ is the value of the polarizability, $\alpha_{\rho\sigma}$, at the equilibrium position. This is representative of Rayleigh scattering. Q_k is the normal coordinates of the vibration. The α'_k is the change in polarizability due to the k-th normal coordinate.

If harmonic vibration is assumed, then the normal coordinate, Q_k , has a time dependence:

$$Q_k = Q_{k0} \cos(\omega_k t + \delta_k) \quad (2.4)$$

The Q_{k0} is normal coordinate amplitude or the amplitude of the vibration. The δ_k is the phase of the vibration and ω_k is the frequency of the vibration.

The equations above can be combined to yield:

$$\mu = \alpha_o E_o \cos(\omega_o t) + \left(\frac{\partial \alpha_{\rho\sigma}}{\partial Q_k} \right)_o E_o Q_{ko} \cos(\omega_k t + \delta_k) \cos(\omega_o t) \quad (2.5)$$

We can then obtain the equation for the induced dipole moment:

$$\mu = \alpha_o E_o \cos(\omega_o t) + \frac{1}{2} \left(\frac{\partial \alpha_{\rho\sigma}}{\partial Q_k} \right)_o E_o Q_{ko} [\cos((\omega_o + \omega_k)t + \delta_k) + \cos((\omega_o - \omega_k)t - \delta_k)] \quad (2.6)$$

This equation represents the induced dipole moment which results from electromagnetic radiation exciting a molecule and inducing dipole moments which oscillate and emit light at three different frequencies. Rayleigh scattering arises from the first term with the frequency ω_o . The second term describes the anti-Stokes ($\omega_o + \omega_m$) and the Stokes ($\omega_o - \omega_m$) of Raman scattering. Furthermore, the term, $\left(\frac{\partial \alpha_{\rho\sigma}}{\partial Q_k} \right)_o$, provides information on if a vibration will be Raman active. If this expression is zero, then the vibration is not Raman active. A vibration will only be Raman active if there is a change in polarizability.

The quantum mechanical approach to the Raman scattering phenomenon will provide information on the Raman band intensities and describe the resonance Raman enhancement, which classical theory does not.

2.3 QUANTUM MECHANICAL DESCRIPTION OF THE RAMAN EFFECT

The Raman Effect was first experimentally discovered by C. V. Raman in 1928. A fundamental equation of Raman theory is the Kramers-Heisenberg dispersion equation, which explains resonance Raman theory from time dependent perturbation theory.⁷⁶⁻⁷⁸ A molecule can absorb or emit only small quantized amounts of energy, according to quantum mechanical principles. These quantized amounts of energy correspond to the difference between discrete energy states

of the molecule. The incident electromagnetic radiation is treated as a perturbation to the molecule. The following equation describes the total radiated power from a Raman transition from state |I> to state |F>:⁷⁷

$$P_{I \rightarrow F} = I \sigma_{I \rightarrow F}(E_L) \quad (2.7)$$

where $P_{I \rightarrow F}$ is the radiated power in photons/second, I is the incident photo flux (photons area⁻¹ sec⁻¹), E_L is the incident photo energy, and $\sigma_{I \rightarrow F}$ is the Raman cross section.

The spontaneous Raman cross section of a Raman band indicates its efficiency for Raman scattering. The probability of Raman scattering is denoted by the Raman cross section from state |I> to state |F>:⁷⁷

$$\sigma_{I \rightarrow F}(E_L) = \frac{8\pi e^4 E_s^3 E_L}{9\hbar^4 c^4} \sum_{\rho, \lambda} \left| (\alpha_{\rho\lambda})_{I \rightarrow F} \right|^2 \quad (2.8)$$

where E_s and E_L are the incident and scattered photo energies and α is the polarizability caused by the |I> to |F> transition. The Raman cross sections in resonance Raman, typically increase as the excitation wavelength is tuned into the analyte's electronic absorption bands.

In resonance Raman, the excitation line is within an electronic transition of a chromophoric group of a molecule.⁷⁹ The intensity of the Raman bands are enhanced by 10³ to 10⁵ factor.⁷⁹ The Raman band intensities, when excited at a particular frequency, depend on the degree to which the polarizability changes due to a specific vibration of the molecule.⁸⁰ The intensity of a Raman band is given theoretically as:⁷⁹

$$I_{IF} = c I_o (v_o - v_{IF})^4 \sum_{\rho, \lambda} \left| (\alpha_{\rho\lambda})_{IF} \right|^2 \quad (2.9)$$

where c is a constant, I_o is the incident laser beam with the frequency v_o , $(v_o - v_{IF})^4$ is the difference between the incident laser frequency (v_o) and the frequency of the transition (v_{IF}), and

“(α_{ρλ})_{I→F}” is the change in the polarizability due to the I → F transition. The second-order perturbation theory equation for polarizability is:

$$(\alpha_{\rho\lambda})_{I\rightarrow F} = \sum_V \left\{ \frac{\langle F|m_\rho|V\rangle\langle V|m_\lambda|I\rangle}{E_V - E_I - E_L - i\Gamma} + \frac{\langle F|m_\lambda|V\rangle\langle V|m_\rho|I\rangle}{E_V - E_F + E_L - i\Gamma} \right\} \quad (2.10)$$

where F and I refer to the final and initial states of the electronic ground state and V refers to an electronic excited intermediate state with the sum being over all intermediate states. The terms E_I, E_V, and E_F are their energies. E_L is the incident photon energy. The term iΓ is the damping constant related to the lifetime of the intermediate states |V⟩ and Γ is the homogeneous linewidths of the electronic transitions. The terms m_ρ and m_λ are vector terms of the transition dipole moment operators.

In normal Raman scattering the incident frequency is less than the frequency of the electronic transition of the molecule, ν_o < ν_{vi}.⁷⁹ In this instance the Raman intensity is proportional to (ν_o - ν_{IF})⁴. In resonance Raman, the excitation frequency approaches resonance with the frequency of a specific electronic oscillation of the molecule. The induced dipole moment will increase tremendously resulting in an enhancement of the Raman scattering by 10⁸.^{43, 81} Resonance Raman involves excitation into an electronic absorption band of a molecule.

In terms of the KHD expression, as the excitation frequency approaches resonance with an electronic absorption band of a molecule the first term (resonant term) will become dominant as the denominator becomes small. The Raman polarizability will be dominated by the vibrations which enhance the displacement of the oscillating charges. This allows for selective enhancement of the Raman scattering of specific chromophores in molecules.

The Born-Oppenheimer approximation can be used to better describe the resonance Raman case.^{79, 80} In this approximation, the total wavefunction in equation 2.10 can be separated

into products of the electronic and vibrational wavefunctions.⁷⁹ Resonance Raman can then be described with the polarizability tensor being expressed as a sum of three Albrecht A, B, and C terms:⁸²

$$(\alpha_{\rho\sigma})_{mn} = A + B + C \quad (2.11)$$

$$A \cong M_e^2 \frac{1}{h} \sum_v \frac{\langle j|v\rangle\langle v|i\rangle}{v_{ji}-v_0+i\Gamma_v} \quad (2.12)$$

where j, v, and i are vibrational states and M_e is the electronic transition moment and

$$B \cong M_e M_e' \frac{1}{h} \sum_v \frac{\langle j|Q|v\rangle\langle v|i\rangle + \langle j|v\rangle\langle v|Q|i\rangle}{v_{vi}-v_0+i\Gamma_v} \quad (2.13)$$

where M_e' contains the vibronic coupling operator involving the electronic Hamiltonian and Q is the vibrational coordinate.⁷⁹ The Franck-Condon overlap $\langle j|v\rangle\langle v|i\rangle$ found in both the A and B term contains the product of two overlap integrals of the ground state and excited state vibrational wave functions.⁷⁹ This term will be non-zero when there is a difference between the geometry of the ground and excited states.^{79, 80} The A term is observed for the symmetric normal modes of a molecule. In the case of resonance Raman, the A term will dominate the enhancement of symmetric normal modes via the strong allowed electronic transitions. The B term consists of the enhancement of mostly non symmetric normal modes due to vibrational coupling of the excited states.^{79 80}

In resonance Raman spectroscopy the excitation wavelength is chosen to excite the sample in the electronic absorption band of the molecule of interest. This leads to greatly increased resonance Raman cross sections on the order of 10^3 - 10^6 greater than normal Raman cross sections.⁴³ This allows for low concentrations of samples to be studied. Furthermore, deep UV excitation with resonance Raman avoids fluorescence. Fluorescence occurs at longer

wavelengths that do not overlap with spectral bands in the UV. Also, most species have extremely small fluorescent quantum yields in the deep UV.⁴⁴ These characteristics of resonance Raman spectroscopy indicate that it is an ideal technique for detection of explosives and examining explosives UV photochemistry. This is because explosives have electronic absorption bands in the deep UV.³¹ Exciting these explosives with deep UV light will lead to an increase in sensitivity and selectivity allowing for trace detection of explosives. Resonance Raman is also an effective technique for monitoring unique spectral changes that result from photochemistry of the explosive analytes.

3.0 SOLUTION AND SOLID TRINITROTOLUENE (TNT) PHOTOCHEMISTRY: PERSISTENCE OF TNT-LIKE ULTRAVIOLET (UV) RESONANCE RAMAN BANDS

Adapted with permission from: "Solution and Solid Trinitrotoluene (TNT) Photochemistry: Persistence of TNT-like Ultraviolet (UV) Resonance Raman Bands", K.L. Gares, S.V. Bykov, B. Godugu and S.A. Asher, *Applied Spectroscopy*, 2014, 68, 49-56.

We examined the 229 nm deep ultraviolet resonance Raman spectra (DUVRR) of solution and solid state trinitrotoluene (TNT) and its solution and solid state photochemistry. Although TNT photodegrades with a solution quantum yield of $\phi \sim 0.015$, the initial photoproducts show DUVRR spectra extraordinarily similar to pure TNT, due to the similar photoproduct enhancement of the $-\text{NO}_2$ stretching vibrations. This results in TNT-like DUVRR spectra even after complete TNT photolysis. These ultraviolet resonance Raman (UVRR) spectral bands enable DUVRR of trace as well as DUVRR standoff TNT detection. We determined the structure of various initial TNT photoproducts by using liquid chromatography mass spectrometry (LCMS) and tandem mass spectrometry (MS/MS). Similar TNT DUVRR spectra and photoproducts are observed in the solution and solid states.

3.1 INTRODUCTION

There is intense interest in standoff detection of trace quantities of explosives on surfaces because of the increasing threats posed by improvised explosive devices (IEDs).^{3, 18, 28, 29, 83} The methods presently being investigated for standoff detection mainly involve spectroscopy, where a light source probes a distant surface and the spectral response is monitored in order to detect explosive molecular species. Standoff detection obviously improves safety for the precious spectroscopists.^{18, 29} This intense interest in developing standoff detection methods, unfortunately, is severely challenged by the difficulty of devising sufficiently sensitive standoff detection methods.^{28, 29}

Raman spectroscopy is one of the few spectroscopic methods that can be developed for standoff detection of dilute analytes. Numerous investigations have probed the utility of normal Raman for explosives detection.^{3, 18, 28-30, 32, 83-86} These normal Raman spectral studies, with excitation in the visible spectral region, while promising, have not demonstrated sufficient S/N to be clearly applicable for standoff detection.

More recently deep UV resonance Raman (DUVRR) has been investigated as a standoff detection method.^{28, 29, 31} It has the potential to have an increased sensitivity to explosive molecules because of resonance enhancement, and the increased Raman cross sections that result from the increased excitation frequencies. In addition, increased DUVRR spectra signal-to-noise ratios occur because there is an absence of competing relaxed fluorescence in condensed phase samples, due to the lack of significant fluorescence at $\lambda < 260$ nm.^{28, 31, 44} Most explosives have their first allowed electronic transitions in the UV region below 250 nm.³¹

The prognosis for DUVRR standoff detection is still unknown because the overall sensitivity depends on unknown phenomena such as the attenuation from self absorption and the

potential interferences that derive from analyte photochemistry as well as the photochemistry of interfering background species. This photochemical interference could result from phenomena such as the loss of analyte spectral intensities due to photodestruction of the analyte, or from interfering spectral contributions from new photoproduct species that derive from the analyte or from other species.⁴² Furthermore, it is well known that some explosives thermally degrade and that some explosives such as trinitrotoluene (TNT) can be photolyzed by near UV irradiation from the sun.⁵⁴ In order to determine whether DUVRR will work for standoff explosives detection it is necessary to characterize the DUVRR of the explosive molecules as well as their photodegradation products.

In the work here we examine the photochemistry of solid and solution TNT by using 229 nm DUVRR. The maximum of the TNT's main absorption band occurs at 229 nm.³¹ This excitation wavelength gives rise to a maximal resonance enhancement of the TNT Raman bands, maximizing the TNT Raman cross sections.³¹ This strongly absorbed wavelength initiates facile TNT photochemistry.^{54, 57, 61-63} We also characterize some of the initial TNT photoproducts.

3.2 EXPERIMENTAL SECTION

3.2.1 Raman Measurements

The ultraviolet Raman (UVR) spectrometer was described previously.^{87, 88} The UVRR spectra were excited by CW 229 nm light generated by using a Coherent Industries Innova 300 FreD frequency doubled Ar⁺ laser.⁸⁷ A Spex Triplemate spectrograph and a Princeton Instruments

CCD camera (spec-10 System, Model 735-0001) were used to disperse and detect the Raman scattered light.

3.2.2 Solution Samples

DUVRR measurements of 1.0 mg/mL TNT solutions in CH₃CN (EMD Chemicals), or CD₃CN (Acros Organics) utilized accumulation times of 5 min. per spectrum measured. DUVRR of CD₃CN, CH₃CN and the quartz cell were separately measured.

Different conditions were used for the photodegradation experiments. The exposure was normalized to absorbed photons/molecule to compare the data between experiments. In the DUVRR photodegradation experiment, a 1.5 mL solution of 1 mg/mL concentration of TNT in CD₃CN (Acros Organics) was placed in a 1 cm path length fused silica temperature controlled cuvette kept at 20.0 °C. The solution was continuously stirred with a magnetic stir bar and excited over a total of 9.5 hours by a focused (~80 μm diameter) 10 mW 229 nm CW laser beam. An initial spectrum was measured during the first 5 min and then spectra were measured after 30, 90, 150, 210, 270, 330, 390, 450, 510, and 570 min. (5, 16, 26, 36, 47, 57, 67, 78, 88, 98 photons/molecule). Another photodegradation experiment was performed for the LC-MS/MS measurements using 1.5 mL of a 0.25 mg/mL TNT in CH₃CN solution in a 1 cm path length fused silica cuvette. It was irradiated for a total of 4 hr. and 45 min. by 5 mW of a 229 nm CW laser beam. 100 μL aliquots were taken at 15, 105, 225, and 285 min. (5, 36, 78, 98 photons/molecule) for LC-MS/MS measurements.

In order to investigate the DUVRR spectra of potential photoproducts of TNT, we purchased the commercially available compounds. Generally the photoproducts are unstable and unsafe when dried in the solid state, so we kept the compounds in the original solvent they were

purchased in for the DUVRR, UV/Vis, and LCMS experiments. The standards of 2-amino-4,6-DNT, 4-amino-2,6-DNT, and 3,5-dinitroaniline came dissolved in CH₃CN. The 2,5-DNP was received as a wet powder and we dissolved this in both water and CD₃CN for measurements. The solvent CD₃CN was used in the photodegradation experiments where we focused on the Raman bands since CD₃CN has no overlapping Raman bands in the 1100-2000 cm⁻¹ spectral region of TNT. DUVRR with 229 nm light was used to measure 0.5 mL samples of 1 mg/mL 2-amino-4,6-dinitrotoluene (Supleco Analytical), 4-amino-2,6-dinitrotoluene (Supleco Analytical), and 3,5-dinitroaniline (Thermo Scientific Acros Organics) in CH₃CN with spectral accumulation times of 3 min. DUVRR using 229 nm light was measured of 1 mg/mL 2,5-dinitrophenol (2,5-DNP) (Aldrich) in CD₃CN with a spectral accumulation time of 5 min.

3.2.3 Solid Samples

A total of 350 mg of MgF₂ (Strem Chemicals) was ground to a fine powder. A volume of 0.2 mL of a 1 mg/mL TNT solution in CH₃CN was added and the system left to evaporate. The dried sample was ground and packed into the groove of a brass rotating Raman cell that was spun during excitation. Raman spectra were measured by using 10 mW of 229 nm CW laser excitation with a laser spot size diameter of ~80 μm at the sample surface. Laser excitation occurred in an almost backscattering geometry (150°) over a 3 min period over which 18 spectra were measured with integration times of 10 sec each. A teflon Raman spectrum was measured for Raman frequency calibration. The Raman spectra of solid 2-amino-4,6-dinitrotoluene (DNT), 4-amino-2,6-DNT, and 3,5-dinitroaniline (3,5-DNA) were also measured as described above using the 1 mg/mL solutions of the derivatives. Na₂SO₄ was added to the solid samples as an internal standard to estimate the Raman cross sections.

3.2.4 Absorption Measurements

A 1.5 mL sample of 1 mg/mL TNT in CH₃CN was irradiated with ~10 mW of 229 nm CW light focused to an 80 μm spot diameter for 9.5 hours. During this irradiation 75 μL aliquots were taken after 0, 30, 210, 450, and 570 min of irradiation. Absorption spectra were measured by using a 0.05 mm pathlength fused silica cuvette and a Varian Cary 5000 UV-Vis-NIR spectrometer. Absorbance spectra were also measured of 1 mg/mL 2-amino-4,6-DNT, 4-amino-2,6-DNT, 3,5-DNA, and 2,5-DNP in CH₃CN using the 0.05 mm pathlength fused silica cuvette.

3.2.5 LCMS Measurements

In order to obtain information on the photochemical products, LC-MS/MS were measured of 0.1 mL aliquots obtained after specific illumination times. The samples were measured using the Dionex-UltiMate 3000 Rapid Separation LC System and the Thermo Scientific Q-Exactive mass spectrometer. Electrospray Ionization (ESI) in the negative ionization mode was used to analyze the samples. A 150 mm X 2 mm diameter Jupiter column containing 3 μm diameter C-18 silica particles was used along with an isocratic method consisting of a mobile phase of 50/50 methanol/water. The flow rate was 0.2 mL/min with a total run time of 20 min. LC-MS/MS was also measured of 0.1 mL samples of 1 mg/mL 2-amino-4,6-DNT, 4-amino-2,6-DNT, and 3,5-DNA in CH₃CN and 2,5-DNP in water.

LCMS was also measured for the solid TNT photochemical products at various illumination times. The surface of two ~ 45 mg samples of the fine powder containing TNT, MgF₂, and Na₂SO₄ were irradiated for 10 and 20 min. Once irradiated, the samples were extracted with CH₃CN and centrifuged. The extract was monitored by LCMS. The analysis

method utilized a combination of ESI and APCI (Atmosphere Pressure Chemical Ionization) using the negative ionization mode with the Shimadzu LCMS2020. The mobile phase consisted of CH₃CN and 0.1 % formic acid. The gradient elution began using 10 % of CH₃CN and gradually increased to 90 % CH₃CN over a 13 min period. The gradient remained constant until 16 min whereupon the elution decreased to 10 % CH₃CN at 20 min. The flow rate was 0.2 mL/min with a total run time of 20 min.

3.3 RESULTS

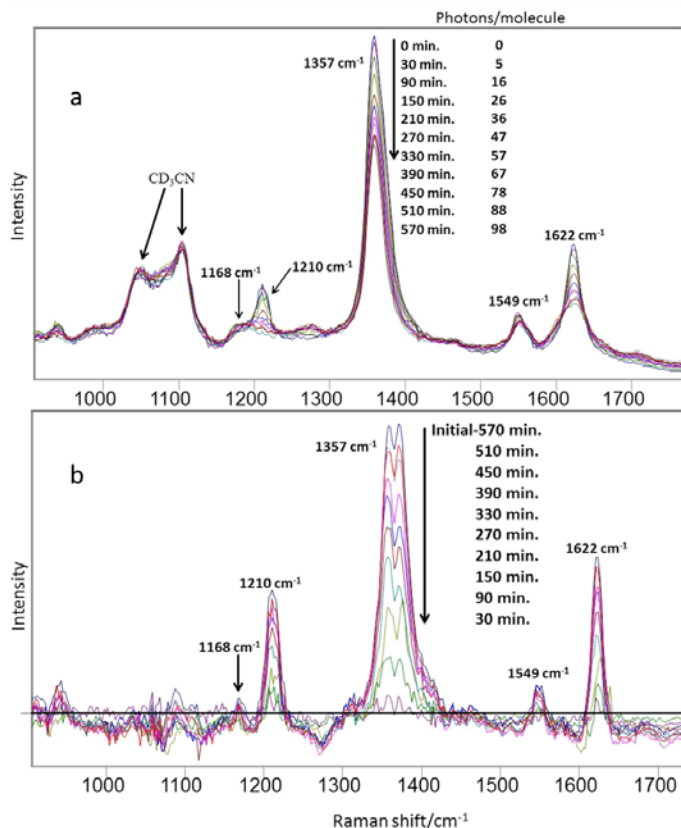


Figure 3.1: A) Irradiance time dependence of DUVRR spectra. 1.5 mL of 1 mg/mL TNT in CD₃CN was irradiated with 10 mW of 229 nm UV light. The TNT spectra were normalized to the CD₃CN 2117 cm⁻¹ band intensity and the silica bands subtracted. The CD₃CN was not

subtracted. The absorbed photons/molecule compared to exposure time is shown. B) TNT difference spectra (initial spectrum minus spectra irradiated for $t = 30, 90, 150, 210, 270, 330, 390, 450, 510,$ and 570 min). Negative features result from photoproduct Raman bands.

Figure 3.1A shows that the DUVRR intensities of TNT dissolved in CD_3CN decays rather slowly with time. The strongest band at 1357 cm^{-1} derives from a TNT vibration where $-\text{NO}_2$ symmetric stretching is coupled to C-N stretching. The 1549 cm^{-1} and 1622 cm^{-1} peaks derive from vibrations where aromatic ring stretching couples to $-\text{NO}_2$ asymmetric stretching.^{31, 89, 90} The 1210 cm^{-1} band derives from a vibration that primarily involves symmetric aromatic ring breathing motion.^{31, 89-91} The band at 1168 cm^{-1} derives from C-C ring in-plane trigonal bending that also contains C-N and C- CH_3 stretching.^{31, 89, 90}

The 1210 cm^{-1} TNT Raman band completely disappears over the 450 min. irradiation time indicating the complete photolysis of TNT. The 1210 cm^{-1} TNT marker band results from a dominantly aromatic ring vibration that occurs only for the specific ring substitution of TNT. As shown below, this band does not exist in the putative photoproduct spectra. The other TNT Raman bands show much smaller relative intensity decreases as well as band shape changes.

The lack of disappearance of these other bands results from the overlapping contributions of photoproduct Raman bands at frequencies similar to the dominant bands of TNT; the vibrations involve similar $-\text{NO}_2$ stretching motions. These photoproduct Raman bands limit the intensity decrease of the 1357 cm^{-1} , 1549 cm^{-1} , and the 1622 cm^{-1} band intensities (by $\sim 30\%$ over the 570 min of irradiation). Even after the 1210 cm^{-1} TNT marker band disappears, the intense spectral features of the $-\text{NO}_2$ stretching vibrations from the photoproducts remain dominant. These strong spectral features allow UV Raman detection of TNT after long irradiation times subsequent to after all TNT is photolyzed.

Figure 3.1B shows the difference spectra between the initial TNT spectrum and the later irradiation time DUVRR spectra of the TNT solutions. The troughs seen in the Figure 3.1B difference spectra derive from photochemical product(s) bands.

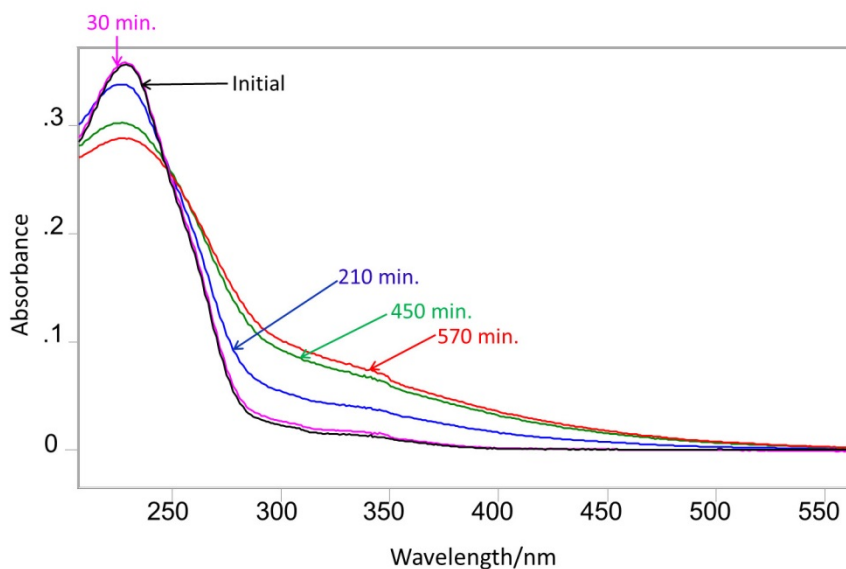


Figure 3.2: Time dependence of the absorption spectra of TNT in CH₃CN after 0, 30, 210, 450, and 570 min. irradiation by 229 nm light measured in a 0.05 mm pathlength cuvette.

Figure 3.2 shows the dependence of the absorption spectrum of TNT in CH₃CN on the irradiation time. After 30 min irradiation the maximum absorbance at ~230 nm slightly increases and then monotonically decreases with time while a broad shoulder appears between ~275-450 nm. The absorption spectra show complex changes as the TNT is photolyzed presumably due to formation of numerous overlapping photoproduct absorption bands.

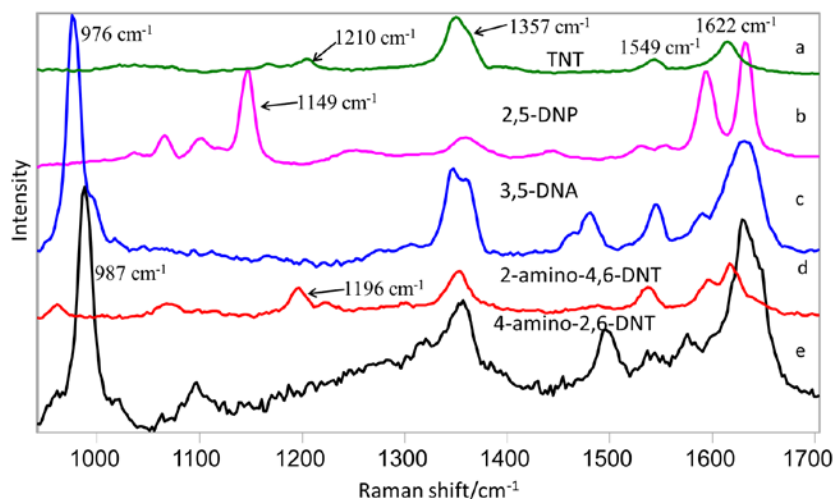


Figure 3.3: 229 nm solution DUVRR spectra of 1 mg/mL TNT and possible photoproducts (in CH_3CN): A) TNT, B) 2,5-dinitrophenol (2,5-DNP) (in CD_3CN), C) 3,5-dinitroaniline, and D) 2-amino-4,6-dinitrotoluene, E) 4-amino-2,6-dinitrotoluene. The silica, CH_3CN , and CD_3CN contributions were subtracted. Spectra are scaled proportional to the Raman cross section (corrected for self absorption and instrument function) of the most intense band in each spectrum: 1357 cm^{-1} band for TNT, 1149 cm^{-1} band for 2,5-DNP, 976 cm^{-1} band for 3,5-DNA, 1352 cm^{-1} band for 2-amino-4,6-DNT, and the 987 cm^{-1} band for 4-amino-2,6-DNT.

Previous studies of the photolysis of TNT showed multiple product formation pathways.^{54, 57} TNT shows significant absorbance in the near UV that can be excited by sunlight to give rise to photoproducts that may be similar to those formed with 229 nm excitation. With sunlight, photochemical reactions occur that leads to amine, hydroxyl, or carboxylic acid groups on the aromatic ring, while the aromatic ring stays intact.⁵⁷ TNT photolysis by sunlight forms initial photoproducts such as 4-amino-2,6-DNT or 2-amino-2,6-DNT, and 3,5-dinitroaniline.⁵⁴ 2,5-DNP is another photoproduct formed in solutions of TNT in water that undergo ultraviolet radiation.⁹²

Figure 3.3 compares the solution DUVRR spectra of TNT to some of its possible photoproducts. The -NO_2 symmetric stretching Raman band at $\sim 1357\text{ cm}^{-1}$ and the -NO_2 antisymmetric stretching Raman band at 1622 cm^{-1} are the strongest DUVRR features of TNT and are strongest in the mixture of photoproducts formed (especially evident in the solid state *vide infra*). Figure 3.3 shows that these photoproducts also display individual strong signature bands for each compound that involves specific aromatic ring vibrations. These occur at 1196 cm^{-1} for 2-amino-4,6-DNT, 987 cm^{-1} for 4-amino-2,6-DNT, 976 cm^{-1} for 3,5-dinitroaniline, and 1149 cm^{-1} for 2,5-DNP. These bands can be utilized to identify each photoproduct as it forms.

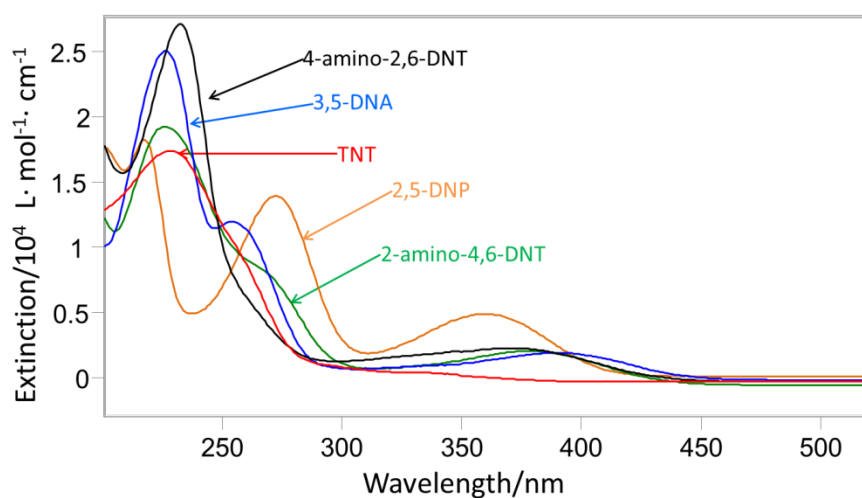


Figure 3.4: Absorption spectra of 1 mg/mL TNT and its putative photoproducts: 2-amino-4,6-DNT, 4-amino-2,6-DNT, 2,5-dinitrophenol (2,5-DNP), and 3,5-dinitroaniline in CH_3CN measured in a 0.05 mm pathlength cuvette.

Figure 3.4 compares the TNT absorption spectrum to that of its putative photoproducts. TNT in CH_3CN shows an absorption maximum at $\sim 229\text{ nm}$ that derives from the S_9/S_{10} electronic transitions⁹¹ and a shoulder at $\sim 260\text{ nm}$ that derives from its S_8 electronic transition.⁹¹ A weaker absorption tail is evident in the near UV that can absorb sunlight. Our recent TNT

electronic state studies indicate that the C_s TNT conformer S₈ and S₉/S₁₀ electronic transitions induce large changes in the –NO₂ group and aromatic ring electron densities.⁹¹ The three putative photoproducts show higher 229 nm molar absorptivities than TNT does. These photoproducts also show larger features at longer wavelengths (~ 370-380 nm). A maximum absorbance at ~226 nm with a shoulder at ~270 nm and a feature at ~380 nm is seen for 2-amino-4,6-DNT. A maximum absorbance at ~230 nm with a second band at ~370 nm is seen for 4-amino-2,6-DNT. A maximum absorbance at ~226 nm with a shoulder at ~255 nm with a second band at ~390 nm is seen for 3,5-dinitroaniline. Three absorption bands at ~218 nm, ~272 nm, and ~360 nm are present for 2,5-DNP. The larger molar absorptivities of the photoproducts at 229 nm explain the initial increased absorption at 229 nm. The later decrease in the 229 nm absorption must result from the conversion of these photoproducts to other species.

The absolute differential resonance Raman cross sections that were measured for the DUVRR bands of TNT, 4-amino-2,6-DNT, 2-amino-4,6-DNT, 2,5-DNP, and 3,5-dinitroaniline are displayed in Table 3.1. These RR cross sections were determined using the known cross section of the 919 cm⁻¹ band of CH₃CN and corrected for self absorption and the instrument function using the method described in references.^{28, 93}

Table 3.1: Absolute differential resonance Raman cross-sections at 229 nm of TNT, 2-amino-4,6-DNT, 4-amino-2,6-DNT, 3,5-dinitroaniline, and 2,5-dinitrophenol in CH₃CN solution.

	Frequencies (cm ⁻¹)	229 nm resonance Raman cross-sections (10 ⁻²⁶ cm ² /molc · sr)
TNT	1168	2.8
	1210	3.8
	1357	15.7
	1549	3.3
	1622	9.2

2-amino-4,6-DNT	1196 1351 1537 1593 1618	6.1 9.8 4.6 3.2 10.0
4-amino-2,6-DNT	987 1354 1497 1576 1634	37.2 16.5 9.3 12.6 28.1
3,5-dinitroaniline	976 1347 1481 1546 1593 1632	39.8 7.4 3.9 5.0 3.7 14.9
2,5-dinitrophenol	1069 1149 1272 1358 1595 1633	3.5 11.7 3.2 1.6 7.9 9.3

Figure 3.5 shows the dependence of the TNT Raman bands intensities upon the irradiation time and the number of photons absorbed. For this analysis we fit each of the TNT DUVRR bands (Figure 3.1A) to single Lorentzians except for the 1357 cm^{-1} $-\text{NO}_2$ symmetric stretching band that we fit to two overlapping Lorentzians. We determined the integrated intensities of these bands at each irradiation time. During irradiation all the incident 229 nm light was absorbed by our optically thick TNT sample. Thus, we can calculate the average number of photons absorbed per TNT molecule at the different irradiation times; the total number of photons absorbed is identical to the number of incident photons.

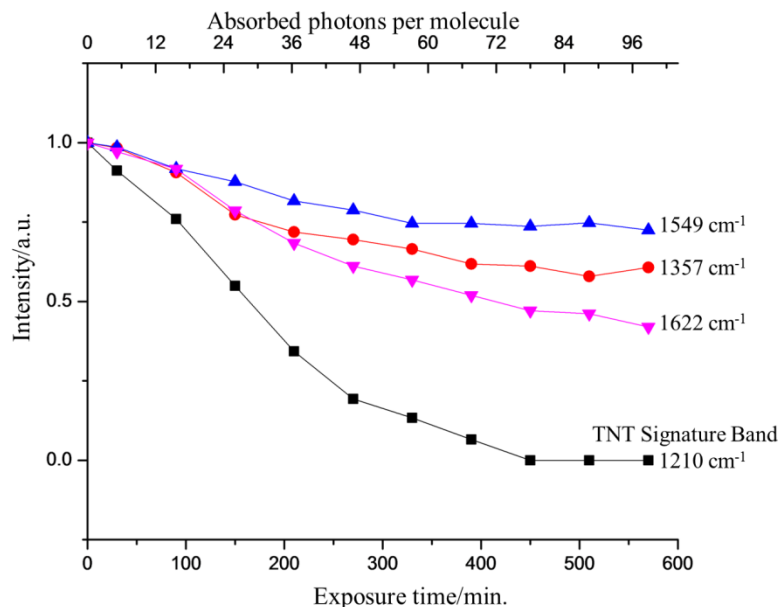


Figure 3.5: Solution TNT Raman band intensities versus irradiation time or absorbed photons per molecule.

We determined the photochemical quantum yield for the TNT photolysis in solution by measuring the 1210 cm⁻¹ TNT signature Raman band (Figure 3.5) time dependence. The initial time dependent rate of change of the TNT concentration is:

$$\frac{d[\text{TNT}]}{dt} = -\phi I / N_a V \quad (3.1)$$

where [TNT] is the TNT concentration, ϕ is the quantum yield, I is the number of photons absorbed per TNT molecule per second, N_a is Avogadro's Number and V is the sample volume. For our calculation we fit the initial linear portion of the 1210 cm⁻¹ band's exponential decay; its slope indicates a quantum yield of $\phi=0.015$ ($R^2=0.9986$).

In order to determine the photoproducts formed we measured the LCMS of the irradiated samples as shown in Figure 3.6.

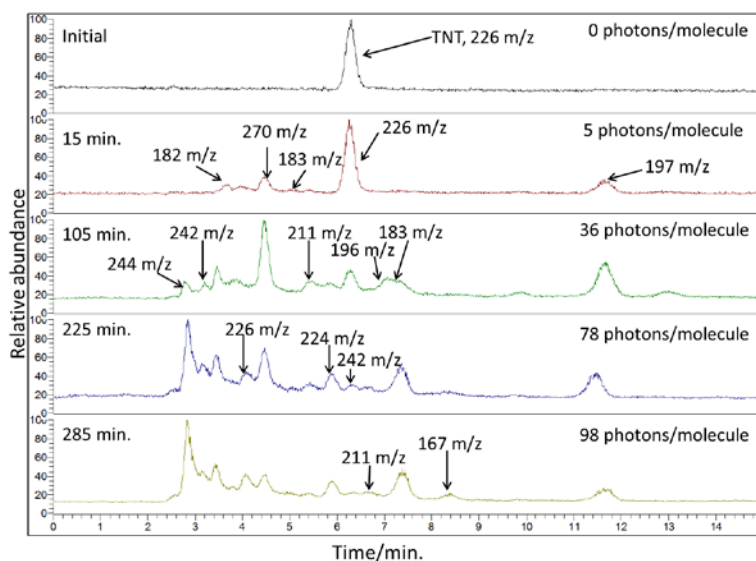


Figure 3.6: Mass spectral ion current chromatograms of TNT irradiated with 229 nm light after different irradiation time intervals. After the 15 min. spectrum, only newly eluted peaks are labeled in the 105, 225, and 285 min. spectra that are not seen in the 15 min. Table 3.2 shows the m/z for every peak in each spectrum. The number of photons per molecule at each irradiation time is labeled.

The chromatogram of the nonirradiated solution shows a single peak at ~6.30 min. that derives from TNT. In contrast, the 15 min. irradiated sample chromatograph shows the TNT peak and multiple peaks at different elution times resulting from photoproducts. As the irradiation time increases, the relative intensities of the TNT peak decrease while new peaks appear that derive from additional photoproducts. The mass chromatograms in Figure 3.6 show the complexity of photoproducts formed.

The LCMS data (Table 3.2) indicates that multiple initial photoproduct are formed during the TNT photolysis. These have mass to charge ratios of 196, 197, 182, and 183 m/z. The 196 m/z and 183 m/z peaks are small in the 15 min. spectrum. At later times additional photoproducts are formed. The 196 m/z photoproduct likely derives from an amino-dinitrotoluene derivative that is also reported in the recent sunlight irradiated TNT photolysis studies that demonstrated 2-

amino-4,6-dinitrotoluene or 4-amino-2,6-dinitrotoluene as TNT photoproducts with 196 m/z.^{54, 57} The 182 m/z photoproduct is likely 3,5-dinitrotoluene, which is also reported to be a sunlight excited photoproduct of TNT.^{54, 57} The 183 m/z photoproduct is likely 2,5-dinitrophenol. The 197 m/z photoproduct's molecular formula is C₇H₆O₅N₂, as given by MS/MS. We could not obtain this compound to use DUVRR to determine its structure. It most likely results from a dinitrobenzyl alcohol as observed in the sunlight photochemical study.⁵⁴ The 183 m/z product at 7.1 min. retention time has a molecular formula of C₆H₄O₅N₂, as given by MS/MS. We were not able to determine its structure.

Table 3.2: Mass chromatograms' retention times, m/z values, and identity of species formed.

TNT Sample	Retention Time (min.)	m/z Peak	Species
Initial	6.3	226	TNT
15 min.	3.5	182	3,5-DNA
	4.4	271	
	5.1	183	2,5-DNP
	6.3	226	TNT
	7.1	196	2-amino-4,6-DNT
	7.4	183	
	11.7	197	
105 min.	2.4	244	
	3.2	242	
	3.5	182	3,5-DNA
	4.1	226	
	4.4	271	
	5.1	183	2,5-DNP
	5.2	211	
	6.3	226	TNT
	7.1	196	2-amino-4,6-DNT
	7.4	183	
	11.7	197	

225 min.	2.4	244	3,5-DNA
	3.2	242	
	3.5	182	
	4.1	226	2,5-DNP
	4.4	271	
	5.1	183	
	5.2	211	
	5.9	224	
	6.2	242	2-amino-4,6-DNT
	6.6	211	
	7.1	196	
7.4	183		
11.7	197		
285 min.	2.4	244	3,5-DNA
	3.2	242	
	3.5	182	
	4.1	226	2,5-DNP
	4.4	271	
	5.1	183	
	5.2	211	
	5.9	224	
	6.2	242	2-amino-4,6-DNT
	6.6	211	
	7.1	196	
	7.4	183	
	8.4	167	
11.7	197		

The MS/MS data directly determines which 196 m/z DNT isomer, forms in the initial stages of TNT photolysis (Figure 3.6). The 4-amino-2,6-DNT derivative's MS/MS contains a peak at 149 m/z that makes it distinctly different from the 2-amino-4,6-DNT derivative's MS/MS spectrum. This 149 m/z peak is not present in the MS/MS of the 196 m/z peak of the TNT irradiated sample. Therefore, it is 2-amino-4,6-DNT that forms in the initial stages of photolysis. The MS/MS data also allowed us to determine some of the other initial photoproducts formed. We find that 3,5-DNA is the 182 m/z compound and 2,5-dinitrophenol is the 183 m/z compound at the 5.1 min. retention time. The pure MS/MS of 2,5-dinitrophenol matches the 183 m/z

MS/MS from the irradiated samples, and the pure 3,5-dinitroaniline MS/MS matches the 182 m/z compound's MS/MS (see Appendix A for details).

Figure 3.7 compares the 229 nm DUVRR solution spectra of 2-amino-4,6-DNT and 2,5-DNP to the TNT difference spectra at different irradiation times. 2-amino-4,6-DNT was determined above to be one of the initial photoproducts formed (Figure 3.6). In Figure 3.7C, a weak negative feature is seen at $\sim 1196\text{ cm}^{-1}$, that likely corresponds to one of the lower intensity signature Raman bands of 2-amino-4,6-DNT indicating that it is detectable as an initial photoproduct. Figure 3.7C also shows weak negative features at $\sim 1273\text{ cm}^{-1}$ and $\sim 1596\text{ cm}^{-1}$, that likely correspond to two of the higher intensity Raman bands of 2,5-DNP (Figure 3.7B) indicating that it is detectable as another initial photoproduct.

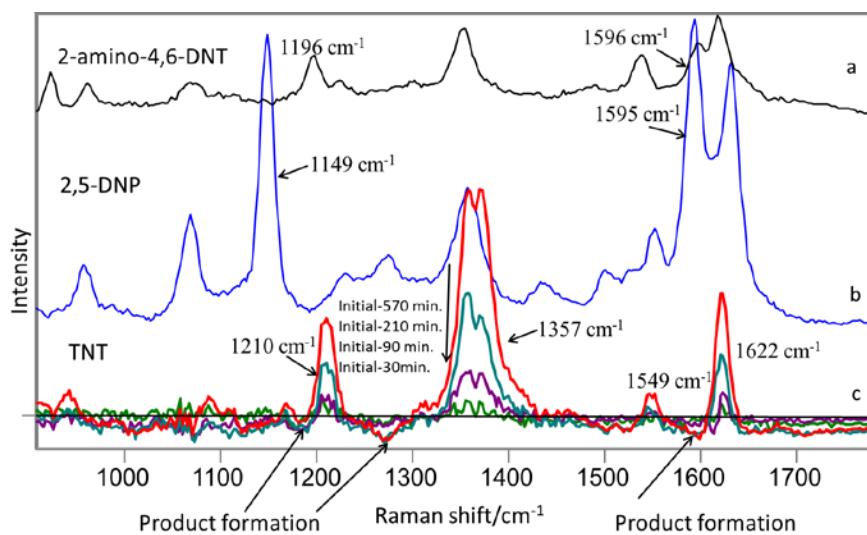


Figure 3.7: 229 nm solution DUVRR spectra of 1 mg/mL A) 2-amino-4,6-DNT (in CH_3CN), and B) 2,5-dinitrophenol (in water), and C) Difference spectra of TNT (in CD_3CN) at times initial minus 30 min., 90 min., 210 min., and 570 min. The quartz, CH_3CN , and CD_3CN contributions have been subtracted. Negative features in spectrum C result from photoproduct contributions. Photoproduct contributions give rise to features at $\sim 1196\text{ cm}^{-1}$, 1273 cm^{-1} , and $\sim 1596\text{ cm}^{-1}$.

Multiple initial photoproducts are formed (Figure 3.6) indicating that TNT photolysis is complex even in the early stages of photolysis. With further photolysis, a complex mixture of photoproducts occur many of which give rise to the overlapping Raman bands of $-\text{NO}_2$ group attached to an aromatic ring. These remaining photoproduct bands give rise to persistent DUVRR TNT-like spectra that enable identification of trace TNT in DUVRR standoff detection studies.

3.3.1 Solid Photolysis

We compared the photochemistry of solid state TNT (Figure 3.8) to that of TNT in CD_3CN (Figure 3.1A). The 1210 cm^{-1} TNT solution signature band occurs in the solid state at 1202 cm^{-1} . As in solution, this band quickly disappears upon irradiation (Figure 3.8).

As in TNT solutions, the strongest solid state TNT DUVRR bands (Figure 3.8) involve $-\text{NO}_2$ stretching vibrations. The solid state TNT photoproducts also have their dominant Raman bands at frequencies similar to that of pristine TNT due to their similar $-\text{NO}_2$ stretching vibration resonance enhancement. The $-\text{NO}_2$ stretching vibration intensities decrease only slowly with irradiation time due to the photoproduct Raman intensity contributions. These strong photoproduct Raman bands give rise to TNT-like DUVRR spectra even after long irradiation times even after all of the TNT is photolyzed.

The DUVRR difference spectra between the initial and irradiated solid state TNT (Figure 3.8) show photolysis of TNT and photoproduct formation similar to that in the solution. As seen in solution, there is a broad mixture of photoproducts forming.

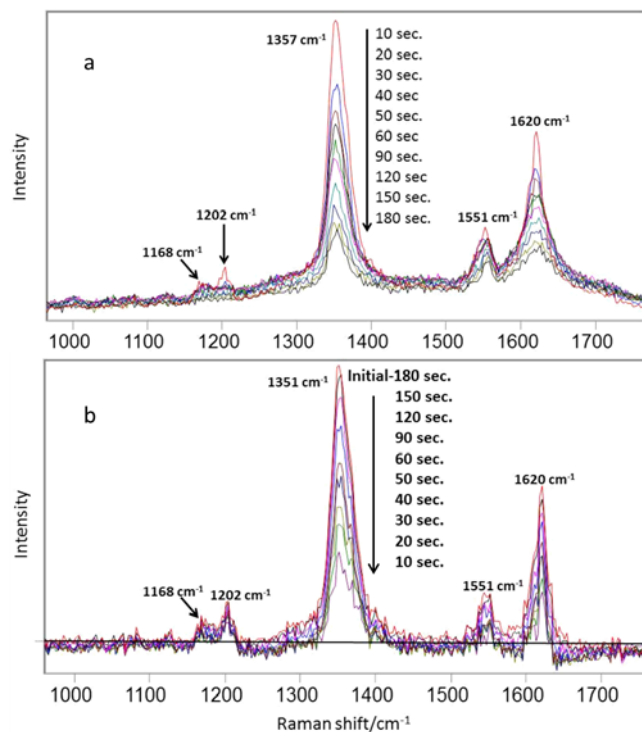


Figure 3.8: A) 229 nm excited, irradiation time dependence of the DUVRR of solid state TNT on MgF₂ powder (0.06 % mass fraction TNT). B) Solid state TNT difference spectra between initial spectrum and spectra measured at = 10, 20, 30, 40, 50, 60, 90, 120, 150, and 180 sec. Negative features derive from photoproduct band contributions.

Figure 3.9 shows the solid state DUVRR spectra of TNT and its putative photoproducts. As in the solution DUVRR, the most intense bands derive from -NO₂ symmetric and asymmetric stretching vibrations that contain aromatic ring stretching motion.^{31, 89, 90} The DUVRR spectra of TNT and its possible, putative photoproducts in the solid state are similar to those in solution except for small frequency shifts and relative intensity changes.

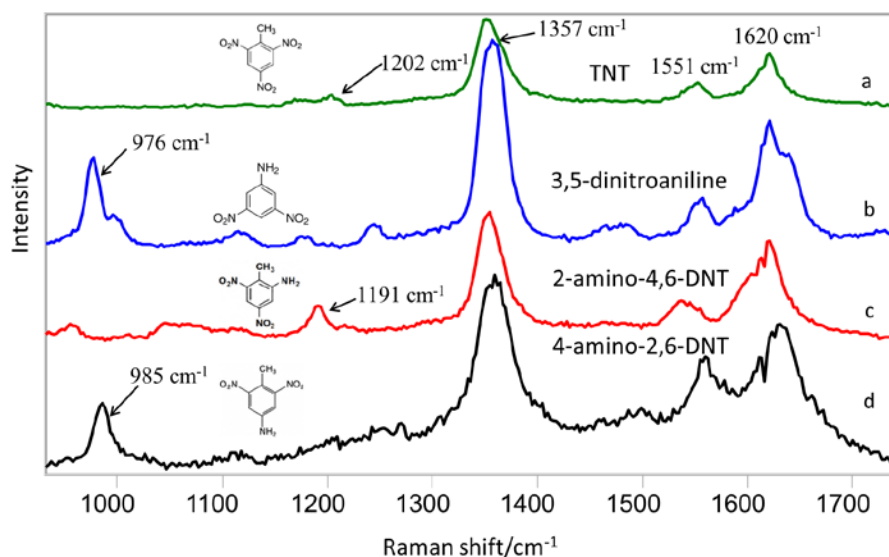


Figure 3.9: 229 nm DUVRR spectra of solid TNT and its putative photoproducts on MgF₂ powder: A) TNT, B) 3,5-dinitroaniline, C) 2-amino-4,6-dinitrotoluene, and D) 4-amino-2,6-dinitrotoluene. Spectra are scaled proportional to their Raman cross sections (corrected for self absorption and instrument function) of the –NO₂ symmetric stretching band, at ~1357 cm⁻¹.

The solid state DUVRR cross sections were determined for TNT, 4-amino-2,6-DNT, 2-amino-4,6-DNT, and 3,5-dinitroaniline as shown in Table 3.3. The RR cross sections were determined by using the Na₂SO₄ 995 cm⁻¹ SO₄⁻² stretching band as an internal intensity standard.⁴⁵

The cross sections were corrected for the instrument efficiency and for self absorption. It was assumed that the extinction coefficients for the solution TNT and photoproducts' bands would be the same as for that in the solid state, in order to correct for self absorption. All of the solid state DUVRR bands of TNT and the photoproducts have decreased 229 nm cross sections compared to those in solution.

Table 3.3: Resonance Raman cross-sections at 229 nm of TNT, 2-amino-4,6-DNT, 4-amino-2,6-DNT, and 3,5-dinitroaniline in the solid state.

	Frequencies (cm ⁻¹)	229 nm resonance Raman cross-sections (10 ⁻²⁶ cm ² /molc · sr)
TNT	1168 1202 1357 1551 1620	0.57 0.53 5.5 1.8 3.7
2-amino-4,6-DNT	1191 1354 1540 1597 1622	1.8 8.8 1.5 1.6 5.0
4-amino-2,6-DNT	985 1359 1494 1565 1633	3.5 15.1 2.1 4.2 6.6
3,5-dinitroaniline	976 1356 1477 1551 1619 1640	3.5 16.3 2.4 3.0 9.13 5.65

To compare the solid state TNT photochemical products to those in solution, we examined the LCMS of irradiated solid samples extracted with CH₃CN. Figure 3.10 shows the mass spectral chromatogram ion currents. In the absence of irradiation the chromatogram shows only the TNT peak, while after longer irradiation time the chromatograms show an attenuated TNT peak and additional peaks at different elution times in a manner similar to the solution state irradiation. Table 3.4 indicates that the photochemistry of solid state TNT is essentially identical to that of TNT in solution (Table 3.2). See Appendix A for the corresponding mass spectra.

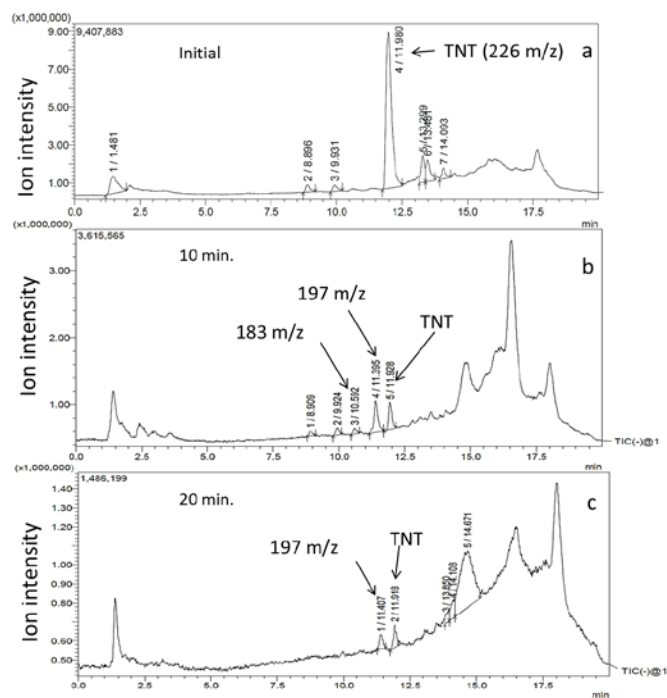


Figure 3.10: Time dependence of LCMS chromatograms of extracted solid TNT irradiated at 229 nm over different time intervals as monitored by their ion current.

Table 3.4: Retention time, m/z, and species present for irradiated solid TNT.

TNT Sample	Retention Time (min.)	m/z Peak
Initial	12.0	226
10 min.	10.6	183
	11.4	197
20 min.	11.9	226
	11.4	197
	11.9	226

3.4 CONCLUSION

The TNT signature band at 1210 cm^{-1} in solution and at 1202 cm^{-1} in the solid state derives from a symmetric aromatic ring breathing motion that is unique to pure TNT. The intensity of these TNT signature bands decrease and disappear with 229 nm irradiation demonstrating that TNT quickly photolyzes with a solution quantum yield of $\phi \sim 0.015$. In contrast, the intensities of the other peaks in the 229 nm TNT solution and solid state DUVRR appear to only slowly decrease. This is because the TNT photoproducts have similar bands at very similar frequencies. These bands mainly involve $-\text{NO}_2$ stretching vibrations. The dominance of these bands in the TNT Raman spectrum and those of its photoproducts enable highly sensitive DUVRR detection of TNT and its photoproducts even after the complete photolysis of TNT. The similarity of the DUVRR of TNT and its photoproducts enables standoff detection of trace quantities of TNT.

We were able to determine some of the initial TNT photoproducts. 2-amino-4,6-DNT, 3,5-DNA, and 2,5-DNP were confirmed to be initial photoproducts formed. The 2-amino-4,6-DNT and 3,5-DNA are the same photoproducts previously observed in the photochemical degradation of TNT by sunlight.

TNT photolysis at later stages forms an even more complex mixture of photoproducts that dominate the DUVRR spectrum. The TNT degradation Raman spectra show a characteristic class of compounds that consist of $-\text{NO}_2$ groups attached to aromatic rings that can be used to sense for TNT for standoff detection.

4.0 SOLUTION AND SOLID HEXAHYDRO-1,3,5-TRINITRO-1,3,5-TRIAZINE (RDX) ULTRAVIOLET (UV) 229 NM PHOTOCHEMISTRY

Adapted with permission from: "Solution and Solid Hexahydro-1,3,5-trinitro-1,3,5-triazine (RDX) Ultraviolet (UV) 229 nm Photochemistry", K.L. Gares, S.V. Bykov, T. Brinzer and S.A. Asher, *Applied Spectroscopy*, 2015, 69, 545-554.

We measured the 229 nm deep ultraviolet resonance Raman (DUVRR) spectra of solution and solid state hexahydro-1,3,5-trinitro-1,3,5-triazine (RDX). We also examined the photochemistry of RDX both in solution and solid states. RDX quickly photodegrades with a HPLC measured solution quantum yield of $\phi \sim 0.35$. New spectral features form over time during the photolysis of RDX indicating photoproduct formation. The photoproduct(s) show stable DUVRR spectra at later irradiation times that allow standoff detection. In the solution state photolysis, nitrate is a photoproduct that can be used as a signature for detection of RDX even after photolysis. We used high performance liquid chromatography-high resolution mass spectrometry (HPLC-HRMS) and gas chromatography mass spectrometry (GCMS) to determine some of the major solution state photoproducts. X-ray photoelectron spectroscopy (XPS) was also used to determine photoproducts formed during solid state RDX photolysis.

4.1 INTRODUCTION

Due to the increasing use and risk of improvised explosive devices (IEDs) there is a need for standoff detection methods to detect explosives for security/environmental screening.^{3, 18, 28, 29, 31, 39, 83, 85} IEDs may contain commercial, military, or homemade explosives that make detection challenging.³⁰ Hexahydro-1,3,5-trinitro-1,3,5-triazine (RDX) is a commonly used explosive. This compound is often found in soil and groundwater near military facilities.⁹⁴⁻⁹⁶

Methods for standoff detection must be able to detect trace amounts of explosives at a distance.^{18, 29, 30} Spectroscopy has become a prominent method for standoff detection.^{18, 28, 29, 31, 39, 85, 94, 97, 98} Spectroscopic methods involve irradiating a surface with a laser beam and then collecting the scattered light for analysis.

Raman spectroscopy has been shown to be an effective standoff detection method for explosives.^{18, 28-31, 39} Raman spectroscopy allows for the identification of explosive molecules through their unique vibrational spectra. Normal Raman gives low signal-to-noise (S/N) spectra due to the small Raman cross sections.^{28, 31, 39} Although standoff measurements of explosives has been demonstrated with normal Raman,^{18, 29, 30, 32, 83, 85} it will be of limited use for standoff detection of low concentrations.

Deep ultraviolet resonance Raman (DUVRR) spectroscopy is emerging as a promising technique for standoff detection of explosives.^{28-31, 39} DUVRR allows for increased sensitivity due to the increased Raman cross sections that result from resonance enhancement. Most explosives have absorption bands in the deep-UV.^{28, 31, 39} Excitation in the deep-UV allows for increased S/N spectra of the explosives making this approach promising for standoff detection.^{28,}

31, 39

With deep UV excitation into electronic absorption bands, explosive compounds can undergo photolysis leading to a loss of analyte species as well as the appearance of interfering spectral features. These interferences in the DUVRR spectra result from the photodegradation of the analyte to new photochemical products.⁴² RDX in both the condensed phase and in the gas phase photodegrades when exposed to UV light into multiple photochemical products.^{52, 55, 56, 60, 65, 95, 96, 99, 100} Thus, the DUVRR spectra of RDX may show additional bands that result from photoproducts. These additional bands could result in characteristic DUVRR time dependent spectra that can be used to identify the explosive precursor.

In this paper, we investigate the photochemistry of solution and solid state RDX using 229 nm DUVRR. We determine the solution state quantum yield for RDX photolysis. We use HPLC-HRMS and GCMS to determine early and late stage RDX photoproducts. XPS was also used to determine solid state RDX photoproducts.

4.2 EXPERIMENTAL

4.2.1 Raman Measurements

The ultraviolet resonance Raman (UVRR) instrumentation was described previously.^{87, 88} The samples were excited by CW 229 nm light that was generated by using a Coherent Industries Innova 300 FreD frequency doubled Ar⁺ laser.⁸⁷ The Raman scattered light was dispersed by using a SPEX Triplemate spectrograph and detected using a Princeton Instruments CCD camera (spec-10 System, Model 735-0001).

4.2.2 Solution Samples

In the deep-ultraviolet resonance Raman (DUVRR) photodegradation experiment, 1 mL of a 3 mg/mL RDX (AccuStandard) in CD₃CN (Acros Organics) solution was placed into a 1 cm pathlength fused silica capped cuvette that was constantly stirred with a magnetic stir bar. The solution was excited with 14 mW of 229 nm light for irradiation times that yielded absorption of 0.1, 1, 2, 5, 10, 20, 30 photons/molecule. We calculated the number of absorbed photons/molecule using Equation 4.1:

$$\frac{\text{abs. photons}}{\text{molecule}} = \frac{\left(t_{\text{irrad.}} \times \frac{P_{\text{laser}}}{E_{\text{photon}}} \right)}{N_{\text{init. RDX}}} \quad (4.1)$$

where P_{laser} is the power of the laser (J/sec), E_{photon} is the energy of a photon (J), $N_{\text{init. RDX}}$ is the number of initial RDX molecules in the sample, and $t_{\text{irrad.}}$ is the irradiation time. We then measured the ultraviolet resonance Raman (UVRR) of these samples after these irradiation times by exciting with ~0.5 mW of 229 laser beam focused to a spot size of ~200 μm. Each spectrum was accumulated for 5 min. The deep ultraviolet Raman (DUVR) of quartz and CD₃CN solvent were subtracted.

The absorbance and high performance liquid chromatography-high resolution mass spectrometry (HPLC-HRMS) photodegradation measurements utilized recrystallized RDX (Omni Explosives) dissolved in CD₃CN. This recrystallized RDX was previously extracted from commercial nylon detonating cords (Omni Explosives) and purified by recrystallization from acetonitrile (Fisher Scientific, HPLC Grade).

For the photodegradation absorbance and HPLC-HRMS measurements, 2 mL of the 2 mg/mL RDX in CD₃CN solution was placed in a capped 1 cm path length fused silica cuvette.

The solution was stirred continuously with a magnetic stir bar and excited by CW 229 nm light focused to a spot size of ~ 80 μm . The photolysis is proportional to the average number of absorbed photons/molecule. 100 μL aliquots were taken at varying irradiation times and analyzed by ultraviolet-visible (UV-Vis) spectroscopy and by high performance liquid chromatography-high resolution mass spectrometry (HPLC-HRMS). The laser power was ~ 0.5 mW at the sample for exposure times in the early stages of photodegradation (0.01 absorbed photons/molecule). For intermediate exposures (1-2 absorbed photons/molecule), the laser power was increased to ~ 3.8 mW at the sample. For 5-30 absorbed photons/molecule, the laser power at the sample was increased to ~ 6.1 mW.

Photodegradation measurements were performed to determine the solution state photolysis quantum yield for RDX. In this experiment a 2 mL sample of 0.06 mg/mL RDX in 50/50 methanol/water + 0.1 % formic acid solution was placed in a 1 cm path length fused silica cuvette and continuously stirred with a magnetic stirring bar. It was irradiated for a total of 9.5 min. by 1 mW of a 229 nm CW laser beam. 100 μL aliquots were taken at 1, 2.8, 5.7, and 9.5 min. (2, 6, 12, and 20 absorbed photons/molecule) for HPLC-HRMS measurements.

We measured the DUVRR spectra of neat nitric acid (EMD Chemicals, 69%). A 1 mL sample was irradiated with ~ 5 mW of a 229 nm CW laser beam. The accumulation time was 90 sec per spectrum.

4.2.3 Absorption Measurements

UV absorbance spectra were measured using a Cary 5000 UV-Vis/near infrared spectrometer operated in a double beam mode. Absorption spectra of the 2 mg/mL RDX irradiated samples were measured in a 0.05 mm path length fused silica cuvette. The sample chamber and

spectrometer were purged with N₂ gas (Matheson Tri-Gas) to allow for absorbance measurements to 185 nm.

4.2.4 Mass Spectrometry Measurements

High performance liquid chromatography-high resolution mass spectrometry (HPLC-HRMS) measurements were performed using a Dionex UltiMate 3000 Rapid Separation LC System and the Thermo Scientific Q-Exactive mass spectrometer. Electrospray ionization (ESI) in the negative ionization mode was used. An isocratic method utilizing a 50/50 methanol/water + 0.1 % formic acid mobile phase was used. The flow rate was 0.2 mL/min.

100 µL aliquots of RDX solutions at specific exposure times were measured in order to determine photochemical products forming during the photolysis of RDX. A reversed-phase 150 mm x 2 mm Jupiter column containing 3 µm diameter C-18 silica particles was used. The HRMS detection limit is 50 m/z.

A HPLC-HRMS experiment was also performed to determine the solution state quantum yield of RDX. A 50 x 2.1 mm Thermo Scientific hypersil gold HPLC column with 1.9 µm diameter C-18 silica particles was used. The area of the RDX peak at ~1.5 min was measured in the high performance liquid chromatography-ultraviolet (HPLC-UV) chromatogram. Calibration standards of 0.06, 0.03, 0.02, 0.008, and 0.004 mg/mL RDX in 50/50 methanol/water + 0.1 % formic acid solutions were measured to obtain a calibration curve. Photolyzed RDX samples at varying irradiation times were also measured using the HPLC. The calibration curve was used to determine the concentrations of the irradiated RDX samples. The area of the RDX peak and the

concentration of the RDX in the samples were then used to determine the solution photolysis quantum yield.

Gas chromatography mass spectrometry (GCMS) was used to identify formamide in the irradiated 30 photon/molecule irradiated RDX sample in CD₃CN. A GC2010 Shimadzu gas chromatograph coupled with a GCMS-QP2010S Shimadzu mass spectrometer was used for the measurements. A SHRXI-5MS column (30 m in length) was used. The column was held at 50 °C ramped at 10 °C/min to 270 °C and finally ramped to 275 °C with a hold time of 5 min. A volume of 1 µL was injected into the gas chromatograph for each sample. Electron ionization (EI) in the positive ionization mode was used. The scan range was from 30-300 m/z. The interface and ion source temperatures were held at 280 and 200 °C, respectively. The total run time was 27 min for each sample.

4.2.5 Solid Samples

For the DUVRR solid state photodegradation experiment, 1 mL of a 1 mg/mL RDX solution in 50:50 CH₃OH:CH₃CN (AccuStandard) was added to MgF₂ powder (Strem Chemicals) and left to evaporate. The dried sample was packed into the groove of a brass rotating Raman cell. The sample was spun during excitation and excited with 4.2 mW of a 229 nm CW laser beam focused to a spot size of ~200 µm. A Teflon UVRR spectrum was measured for Raman frequency calibration. Each spectrum was accumulated for 5 sec.

We prepared solid state samples for photolysis studies by evaporating 1 mL of a 1 mg/mL RDX solution in 50:50 CH₃OH:CH₃CN (AccuStandard) onto a quartz slide to obtain 1 mg of RDX crystals. 1 µL of a 50:50 H₂O:CH₃OH mixture was added to the 1 mg of RDX crystals on the quartz slide and compacted to form a paste. The system was left to evaporate. The

dried sample was irradiated with 8.5 mW of a CW 229 nm laser beam focused to a spot size of ~200 μm . DUVRR spectra were accumulated for 30 sec.

We prepared a solid state RDX sample for DUVRR and X-ray photoelectron spectroscopy (XPS) measurements by pipetting 6 μL of water onto a gold coated glass slide. We then pipetted 10 μL of a 1 mg/mL RDX solution in 50:50 $\text{CH}_3\text{OH}:\text{CH}_3\text{CN}$ onto the 6 μL of water on the slide. The system was left to evaporate. The dried sample was irradiated for 465 min with 5 mW CW 229 nm laser beam focused to a spot size of ~300 μm .

4.2.6 X-ray Photoelectron Spectroscopy

X-ray photoelectron spectroscopy (XPS) measurements of the RDX utilized the Thermo Scientific ESCALAB 250Xi instrument with a monochromatic Al $\text{K}\alpha$ source focused to a spot size of 200 μm . The sample stage was cooled with liquid nitrogen in a base vacuum of 1×10^{-10} mbar. A survey spectrum was taken for each sample with a pass energy of 150 eV and a step size of 0.1 eV. The C1s and N1s spectra were measured with a pass energy of 50 eV and a step size of 0.1 eV. The flood gun was used to charge neutralize the RDX sample.

4.2.7 X-ray Powder Diffraction

X-ray powder diffraction was used to determine the crystal structure of the RDX on the SiO_2 substrate and RDX on the gold coated glass slide. X-ray powder diffraction patterns were collected using a Bruker AXS D8 Discover powder diffractometer with the Lynxeye 1-D detector at 40 kV, 40 mA for Cu $\text{K}\alpha$ ($\lambda = 1.5406 \text{ \AA}$) radiation. A scan speed of 0.400495 s/step and a step size of 0.04° was used for the sample of RDX on SiO_2 . A scan speed of 5 s/step and a

step size of 0.04° was used for the sample of RDX on the gold coated glass slide. The experimental x-ray powder patterns of RDX for both samples were corrected for background using the Bruker Eva software program. They were then matched to a Powder Diffraction File (PDF). The experimental RDX x-ray powder patterns are in excellent agreement with the PDF entry 00-044-1619, which is the alpha form of RDX with unit-cell parameters of $a=13.192$, $b=11.592$, $c=10.709$, and $\alpha=\beta=\gamma=90$ deg. See Appendix B for the X-ray powder diffraction patterns.

4.3 RESULTS

4.3.1 Solution Photolysis

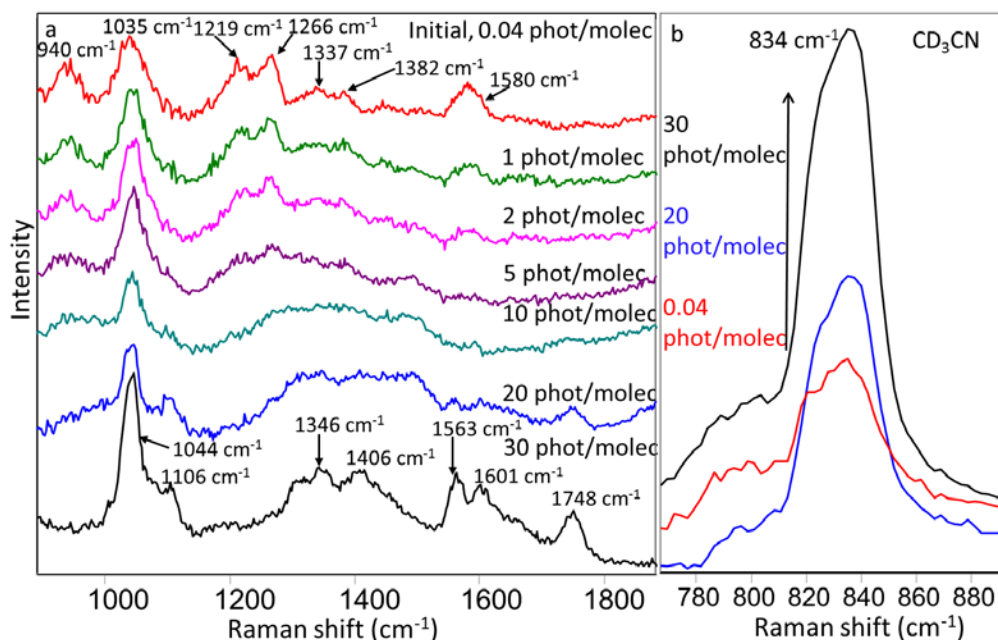


Figure 4.1: a) Solution DUVRR spectra of RDX in CD₃CN with increasing irradiation (photons absorbed per molecule). 1 mL of 3 mg/mL RDX in CD₃CN was irradiated with 17 mW of 229

nm light. Quartz and CD₃CN Raman bands were subtracted. b) DUVRR spectra of the 834 cm⁻¹ CD₃CN band in the RDX spectra with increasing irradiation time. The CD₃CN band increases in intensity as the photolysis increases.

The least photolyzed (0.04 photons/molecule) DUVRR spectrum of RDX in Figure 4.1a shows DUVRR bands at 940 cm⁻¹ (N-N stretching), 1035 cm⁻¹ (N-C stretching with CH₂ rocking), 1219 cm⁻¹ (N-C stretching), 1266 cm⁻¹ (N-N stretching and O-N-O stretching), 1337 cm⁻¹ (CH₂ wag or combination), 1382 cm⁻¹ (CH₂ twisting), and 1580 cm⁻¹ (O-N-O stretching).^{28, 31, 101}

Photochemically induced spectral changes occur even after a small number of photons are absorbed per RDX molecule. This indicates a high RDX photolysis quantum yield. The 940 cm⁻¹ N-N stretching band essentially disappears after the absorption of 5 phot/molec. This indicates destruction of the RDX N-N bonds in the initial stage of photolysis. The 1580 cm⁻¹ band, which derives from O-N-O stretching, also disappears after 5 phot/molec illumination. This indicates the loss of the -NO₂ groups of RDX.

At longer irradiation times, DUVRR bands of RDX photoproducts appear, as seen in the 20 phot/molec spectrum. The Raman bands of the photoproducts increase in the 30 phot/molec spectrum. This is in part due to the absorption decrease at 229 nm observed in the 30 phot/molec spectrum (Figure 4.2a). The photoproducts absorb less at 229 nm and therefore a larger volume is excited due to the laser beam penetrating deeper into the solution. This also leads to an increase in the Raman intensities of the solvent Raman bands. Figure 4.1b shows the increase in Raman intensity of the solvent CD₃CN band at 834 cm⁻¹ as the irradiation time increases.

A dominating photoproduct Raman band is seen at 1044 cm⁻¹. This band is likely to result from the ν_1 symmetric stretching vibration of NO₃⁻.⁵¹

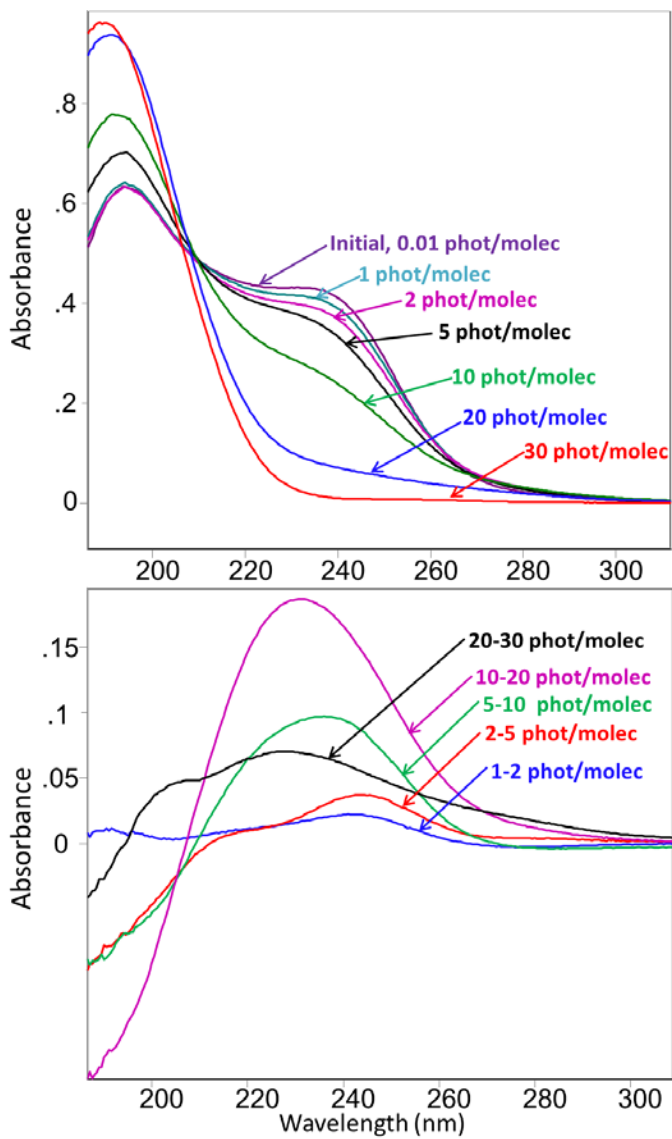


Figure 4.2: a) Dependence of the absorption spectra of RDX in CD₃CN upon irradiation of 0.01, 1, 2, 5, 10, 20, and 30 photons/molecule by 229 nm light measured in a 0.05 mm path length cuvette. b) Absorbance difference spectra between 1-2, 2-5, 5-10, 10-20, and 20-30 photons/molecule absorption spectra.

Figure 4.2a shows the dependence of the RDX absorption spectra on increasing irradiation by 229 nm light. The initial RDX absorption spectrum shows a strong peak at ~195

nm and a broad shoulder at ~240 nm. Our recent excited electronic state studies of RDX indicate that these absorption bands derive from multiple overlapping electronic transitions.⁹¹

The broad absorption shoulder at ~240 nm decreases as RDX is photolyzed. The ~190 nm absorption increases and blue-shifts during the photolysis. The 30 photon/molecule spectrum in Figure 4.2a shows a single, broad absorption peak with a maximum at ~190 nm. The increase in the 190 nm absorption band observed after long irradiation indicates formation of photoproducts.

A complex behavior is observed in the absorption difference spectra (Figure 4.2b). Multiple difference absorption bands evolve during the photolysis. This complex photochemistry is likely due to multiple photoproduct species forming during the photolysis.

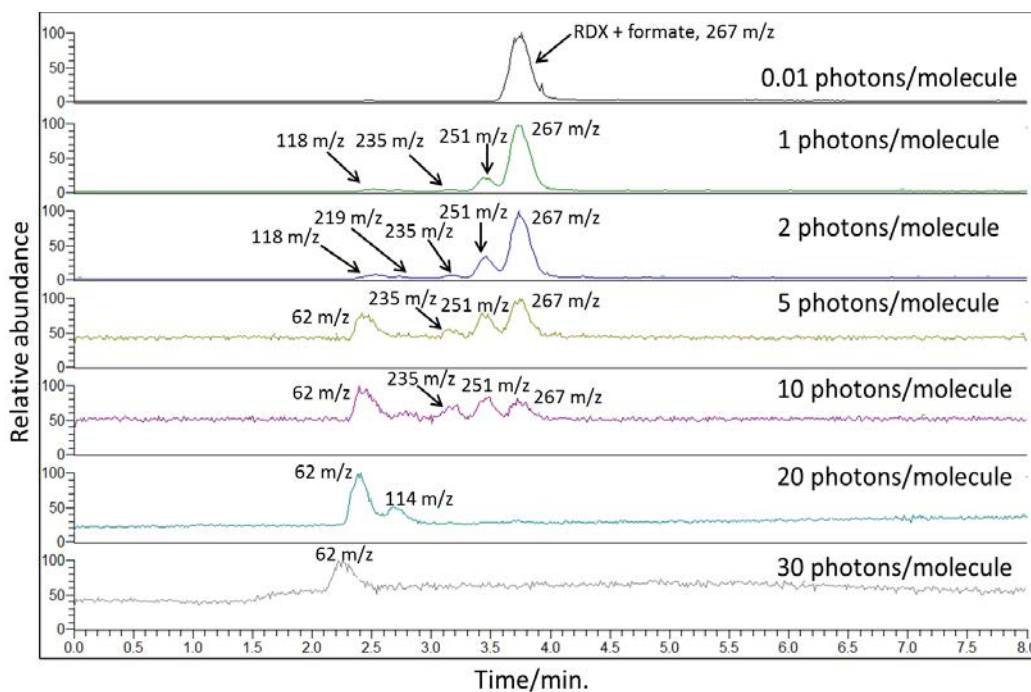


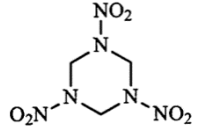
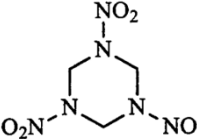
Figure 4.3: Mass spectral ion current chromatograms of RDX irradiated by 229 nm light at different irradiation times. The irradiation times are given in the number of absorbed

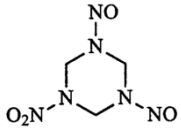
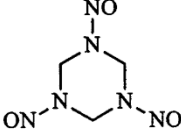
photons/molecule. The m/z values correspond to the formate adducts. Table 4.1 indicates the proposed compounds along with their calculated m/z values.

We used high performance liquid chromatography-high resolution mass spectrometry (HPLC-HRMS) to determine the photoproducts formed during RDX photolysis (Figure 4.3). The HRMS low mass detection limit is 50 m/z .

The non-irradiated sample chromatogram shows a peak that elutes at ~ 3.7 min that derives from the RDX + formate complex. Studies using electrospray ionization (ESI) in the negative ionization mode show that RDX forms adducts with anions.¹⁰² As the irradiation time increases, new peaks appear indicating formation of photoproducts. At least three major condensed phase photoproducts are observed during the initial photolysis with m/z values of 251, 235, and 219 m/z . At larger irradiances (5-30 photons/molecule) an intense peak is observed at ~ 2.4 min with a mass-to-charge ratio of 62 m/z . Table 4.1 indicates the Figure 4.3 retention times, m/z values, and their proposed identities.

Table 4.1: Mass chromatogram retention times, m/z values, empirical formulas, and proposed identities of the species that form a formate adduct.

Retention time /min	m/z	Empirical formula	Proposed species / structure + formate
3.7	267	$[\text{C}_4\text{H}_7\text{O}_8\text{N}_6]^-$	RDX + formate 
3.5	251	$[\text{C}_4\text{H}_7\text{O}_7\text{N}_6]^-$	MNX + formate 

3.2	235	$[\text{C}_4\text{H}_7\text{O}_6\text{N}_6]^-$	DNX + formate 
3.0	219	$[\text{C}_4\text{H}_7\text{O}_5\text{N}_6]^-$	TNX + formate 
2.3-2.4	61	$[\text{NO}_3]^-$	Nitrate

Three major condensed phase initial photoproducts of RDX are hexahydro-1-nitroso-3,5-dinitro-1,3,5-triazine (MNX), hexahydro-1,3-dinitroso-5-nitro-1,3,5-triazine (DNX), and hexahydro-1,3,5-trinitroso-1,3,5-triazine (TNX) with mass-to-charge ratios of 251, 235, and 219 m/z. At 5 phot/molec, the nitrate ion appears with a mass-to-charge ratio of 62 m/z.

RDX photolysis in the gas phase has been studied in detail.^{55, 60, 100} Formation of gaseous photoproducts such as NO, N₂O, HCN, and formaldehyde were detected.^{55, 60, 100}

The photolysis of RDX occurs along multiple parallel photolysis pathways.^{60, 66, 95, 99} The UVRR spectra show resonance enhanced photoproducts such as nitrate that must involve cleavage of the RDX N-N bonds. The HPLC-HRMS data show the formation of nitroso derivatives as well as formation of nitrate. The UVRR and HPLC-HRMS give different insights into the complex photolysis of RDX.

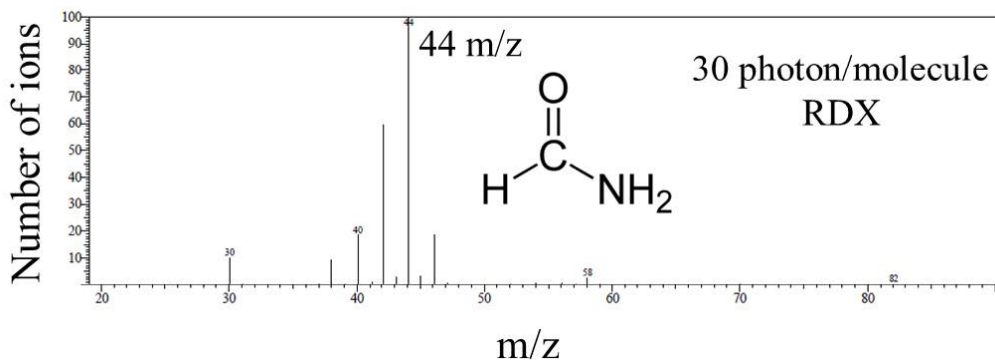


Figure 4.4: GCMS of a 30 photon/molecule irradiated RDX sample. The peak at 44 m/z is indicative of formamide.

Gas chromatography mass spectrometry (GCMS) was used to determine lower molecular weight (< 50 m/z) compounds formed during RDX photolysis. Figure 4.4 shows the mass spectrum that identified formamide in the 30 photon/molecule irradiated RDX solution sample. Presumably, we do not see formamide bands present in the photolyzed RDX DUVRR spectra because its concentration is below the detection limit.

We determined the photochemical quantum yield of RDX photolysis in the solution state by monitoring both the RDX peak intensity decrease in the high performance liquid chromatography (HPLC), and the intensity decrease of the 940 cm^{-1} and 1580 cm^{-1} Raman bands as a function of absorbed photons per molecule (Figure 4.5).

We use a linear fit of the initial portion of the intensity decay to calculate the slope which indicates the quantum yield (Figure 4.5). The initial portion of the 940 cm^{-1} and 1580 cm^{-1} Raman peaks intensity decay, and the decay of the RDX HPLC peak assumes that at the early stage of photolysis only RDX molecules absorb photons and photolyze removing their contributions to the HPLC band and to the RDX Raman intensities.

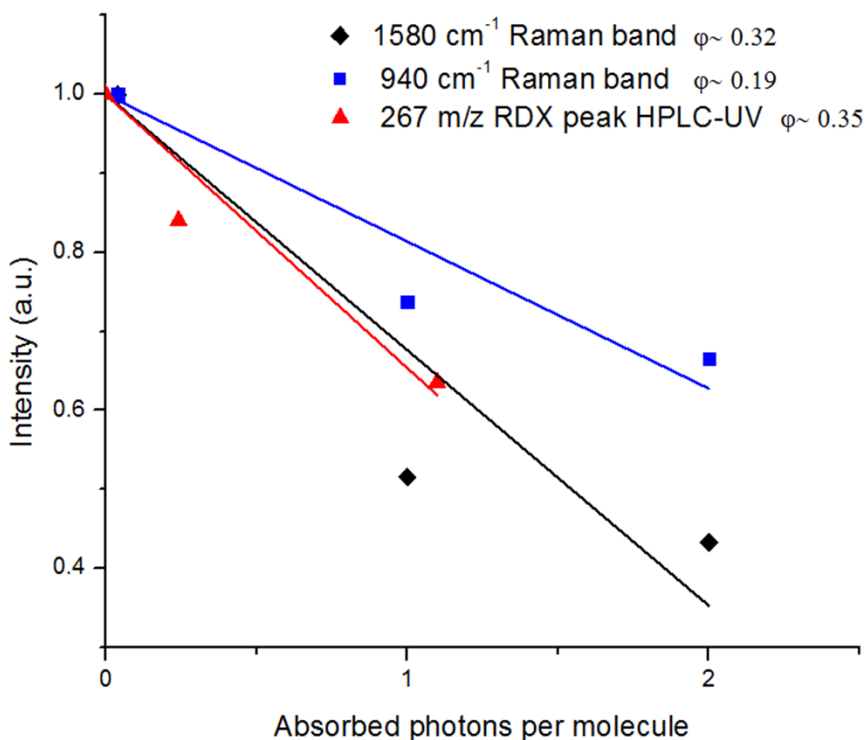


Figure 4.5: Solution RDX 940 cm^{-1} and 1580 cm^{-1} Raman bands intensity vs. absorbed photons per molecule and the 267 m/z peak intensity from the HPLC-UV versus absorbed photons/molecule. A linear fit is shown for each of the plots.

We measured the HPLC-mass spectrometry to identify the RDX peak and used HPLC-UV chromatograms to determine the RDX content of the initial and the irradiated samples of RDX. We calibrated this measurement with 0.030, 0.015, 0.0076, 0.0038 mg/mL RDX standard solutions. A linear fit gives a slope indicating a quantum yield of $\phi \sim 0.35$ ($R^2=0.99$).

Figure 4.5 also shows the intensity decay of the 940 cm^{-1} Raman band vs absorbed photons/molecule in the initial stages of RDX photolysis. The 940 cm^{-1} Raman band derives from N-N stretching^{28, 31, 101} and disappears quickly in the solution state photolysis indicating cleavage of the N-NO₂ bond. The linear fit gives a quantum yield of $\phi = 0.19$ ($R^2 = 0.99$). The intensity decay of the 1580 cm^{-1} O-N-O stretching^{28, 31, 101} Raman band vs. absorbed

photons/molecule is shown in Figure 4.5. The 1580 cm^{-1} Raman band disappears quickly in the solution photolysis. A linear fit gives a quantum yield of $\phi = 0.32$ ($R^2 = 0.97$).

The DUVRR quantum yield of the 1580 cm^{-1} Raman band is close to that of the HPLC 0.35, while the 940 cm^{-1} Raman band is 0.19. The 940 cm^{-1} Raman band intensity may contain contribution from photoproducts of RDX that will bias the results toward a smaller RDX quantum yield.

We examined the Raman difference spectral changes during photolysis of solution state RDX to examine photoproduct formation (Figure 4.6). In addition, we measured the 229 nm DUVRR spectrum of nitric acid to compare its spectrum to the 30 photon/molecule difference spectrum of RDX (Figure 4.6).

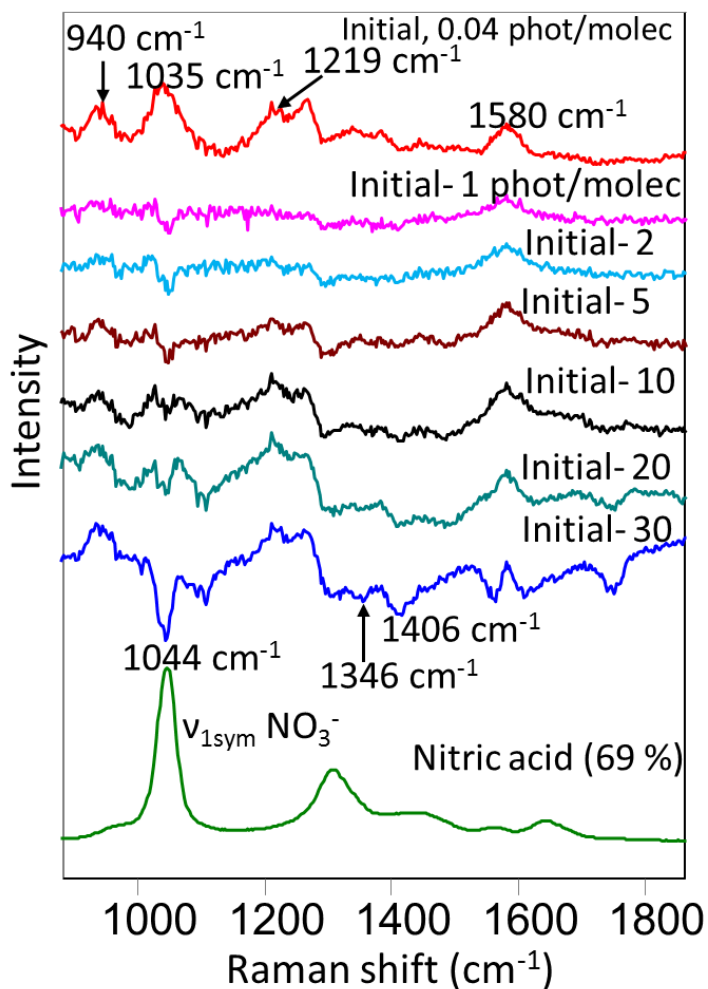


Figure 4.6: The RDX CD₃CN initial solution, 0.04 photon/molecule spectrum is shown in comparison to the RDX difference spectra between the minimally photolyzed 0.04 phot/molec RDX sample, and the 229 nm DUVRR spectra of RDX samples that absorbed 1, 2, 5, 10, 20, and 30 phot/molec. Negative peaks derive from photoproducts. 229 nm solution DUVRR spectrum of neat nitric acid (69 %) is also shown. The quartz and CD₃CN Raman bands were subtracted.

Figure 4.6 compares the RDX initial, 0.04 phot/molec spectrum to the difference spectra between the initial RDX DUVRR spectrum and the irradiated DUVRR spectra of RDX. Positive features indicate a decrease in the RDX concentrations while negative features indicate bands from photochemical products. We see negative features showing photoproduct formation at 1346

and 1406 cm^{-1} that increase as the irradiation time increases. The 1044 cm^{-1} Raman band intensity increases with irradiation time indicating photoproduct formation. The HPLC-HRMS studies discussed above demonstrated the formation of nitrate. We presume that the 1044 cm^{-1} band derives from the NO_3^- symmetric stretching vibration.

4.3.2 Solid Photolysis

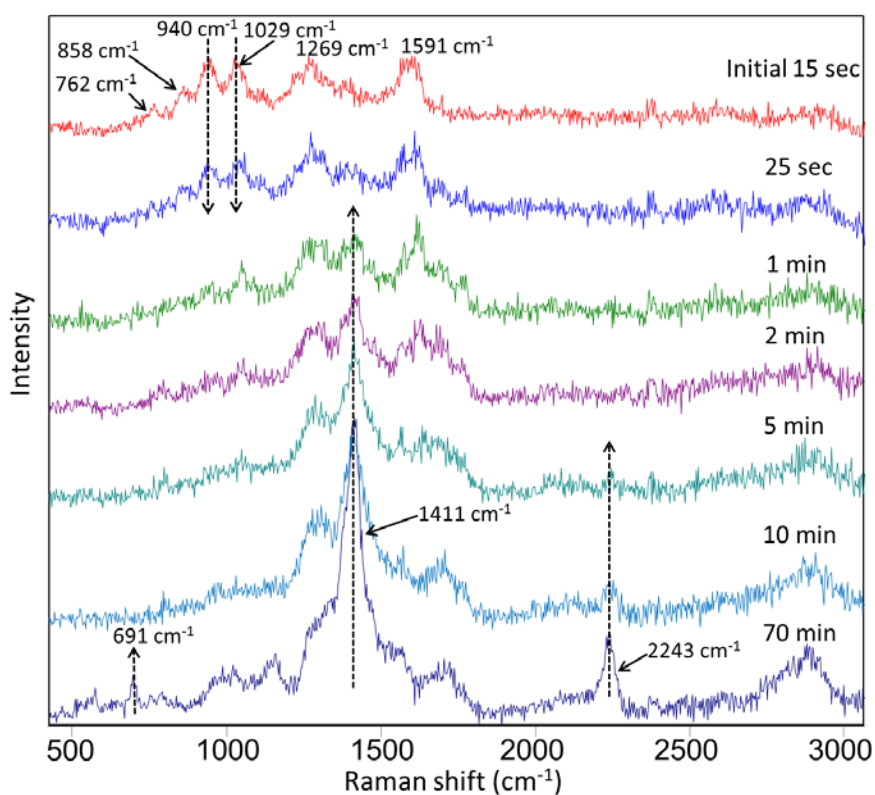


Figure 4.7: Irradiation time dependence of 229 nm excited DUVRR spectra of solid state RDX on MgF₂ powder (< 1 % by weight RDX). The sample was spun during excitation and irradiated with 4.2 mW of a 229 nm CW laser beam focused to a spot size of ~200 μm .

We compared the DUVRR spectra of solid state RDX (Fig. 4.7) to that of RDX in CD₃CN (Figure 4.1a). We were unable to reliably estimate the number of photons/molecule during the solid state photolysis of the RDX on the MgF₂ powder.

The minimally photolyzed RDX DUVRR spectra in the solid and solution states are similar and show the same major bands. DUVRR bands in the minimally photolyzed 15 sec solid state samples (Figure 4.7) are at 762 cm⁻¹ (ring bending and NO₂ scissoring), 858 cm⁻¹ (C-N stretching with NO₂ scissoring), 940 cm⁻¹ (N-N stretching), 1029 cm⁻¹ (N-C stretching with CH₂ rocking), 1226 cm⁻¹ (N-C stretching), 1269 cm⁻¹ (N-N stretching and O-N-O stretching), and 1591 cm⁻¹ (O-N-O stretching).^{28, 31, 101}

As solid state RDX absorbs photons, the isolated 940 cm⁻¹ band consisting of N-N stretching decreases and disappears after 1 min of irradiation. This indicates cleavage the N-N bond and the loss of the RDX -NO₂ groups. It is known that the initial step in the photochemical decomposition of RDX is the cleavage of the N-N bond to generate NO₂.^{55, 56, 66, 100} The solid and solution photolysis of RDX both involve cleavage of the N-N bond releasing NO₂.

A decrease in the 762 cm⁻¹ and the 858 cm⁻¹ bands is also seen after 1 min of irradiation showing the loss of the -NO₂ groups. The 1029 cm⁻¹ band that involves N-C stretching with CH₂ rocking band disappears after 1 min. The disappearance of this band indicates the loss of the CH₂ groups.

In the 1 min photolyzed RDX spectrum, a band at 1411 cm⁻¹ increases in intensity indicating photoproduct formation. The 5 min spectrum shows a band appearing at 2243 cm⁻¹ that we assign to C≡N stretching vibration.¹⁰³⁻¹⁰⁵ After long irradiation, the 70 min spectrum shows a band at 691 cm⁻¹ from a late stage photoproduct.

We studied the later stages of photolysis of RDX to identify late stage photoproducts that give rise to the 691, 1411, and 2243 cm^{-1} Raman bands present in the 70 min spectrum in Figure 4.7. For this sample ~ 1 mg of RDX was deposited onto a quartz slide as described above. The sample was stationary during excitation resulting in a faster photolysis and more RDX photodegradation.

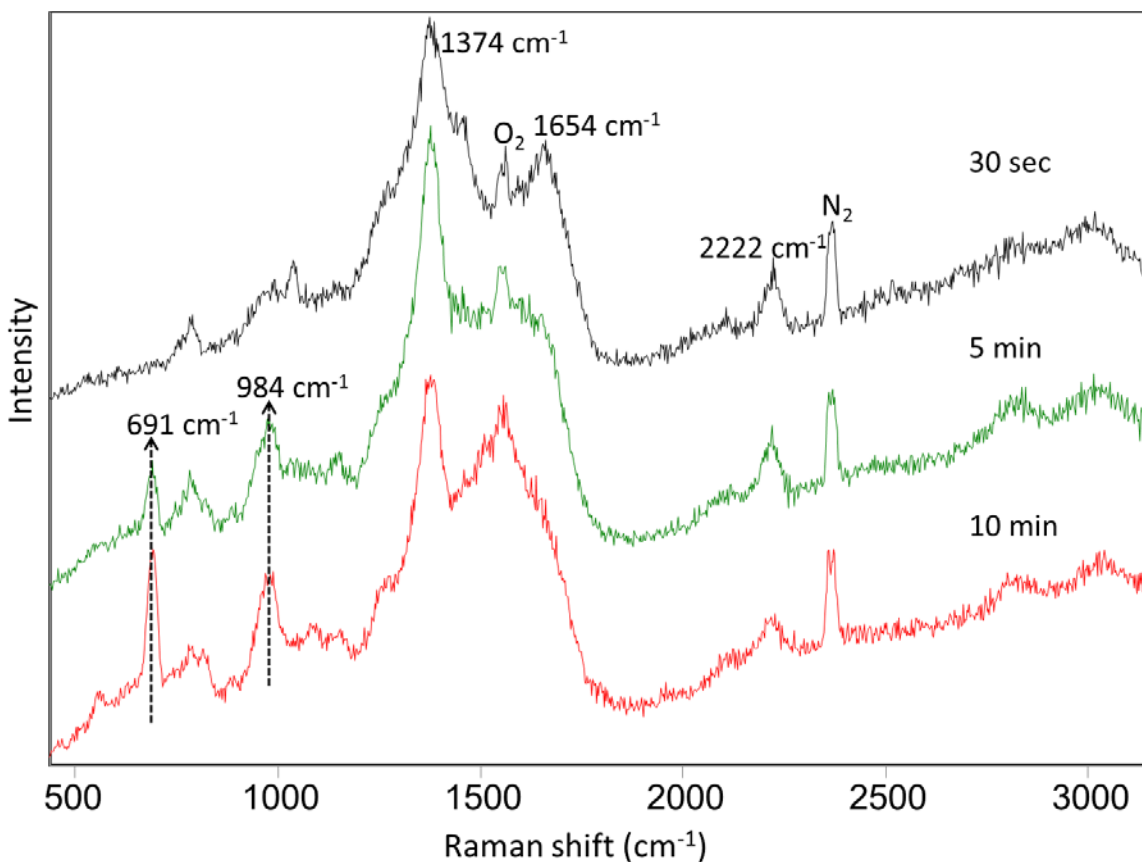


Figure 4.8: 229 nm DUVRR spectra of solid state photolyzed RDX on a SiO_2 substrate with varying irradiation times. The sample was stationary during excitation and contained ~ 1 mg of RDX. The sample was irradiated with 8.5 mW of a CW 229 nm laser beam focused to a spot size of ~ 200 μm . The 1555 and 2368 cm^{-1} bands derive from atmospheric oxygen and nitrogen, respectively.

The 30 sec Figure 4.8 DUVRR spectrum of RDX on a SiO₂ substrate displays three strong bands at 1374 cm⁻¹, 1654 cm⁻¹, and 2222 cm⁻¹. The band at 2222 cm⁻¹ is assigned to a C≡N stretching vibration.¹⁰³⁻¹⁰⁵ This band is 20 cm⁻¹ downshifted compared to that of RDX on MgF₂ at 2243 cm⁻¹. It appears that two different C≡N containing photochemical products are formed. The C≡N stretching frequency typically occurs between 2200-2260 cm⁻¹ in nitrile containing compounds.^{106, 107} The 1374 cm⁻¹ and 1654 cm⁻¹ bands resemble the “D” and “G” bands of graphitic/amorphous carbon nitride like samples.^{42, 103, 104, 108-110} The 1374 cm⁻¹ “D” band is generally observed in graphitic carbon and carbon nitride materials.¹⁰⁹ The ~1650 cm⁻¹ “G” band derives from the bond stretching of sp² atoms in both ring and chain structures.^{103, 104} We assign the 1411 cm⁻¹ band to the breathing modes of sp² atoms in ring structures.^{103, 104}

The more extensively irradiated samples show two additional strong peaks at 691 cm⁻¹ and 984 cm⁻¹ that grow in over time. The 984 cm⁻¹ peak we assign as a symmetric N-breathing mode of triazine rings due to this being a common vibration seen in graphitic carbon nitrides.¹⁰⁹ The 691 cm⁻¹ peak we assign to CNC in plane bending vibrations which is also seen for carbon nitrides.¹⁰⁹ The 1654 cm⁻¹ band becomes more intense as the number of photons absorbed increases. Figure 4.8 indicates the formation of a graphitic/amorphous carbon nitride after RDX is extensively photolyzed. The carbon nitride DUVRR spectrum can be used for standoff detection of RDX and photolyzed RDX.

RDX exists in two different polymorphic phases, α-RDX and β-RDX.^{101, 111-116} We used x-ray diffraction to determine that the RDX on SiO₂ and the RDX on the gold coated glass slide is in the α-RDX form. We also determined that the RDX on MgF₂ is in the α-RDX form by comparing its UVRR to the normal Raman spectra. The normal Raman spectrum easily differentiates between α-RDX and β-RDX.^{101, 111, 113-116} α-RDX has molecular symmetry C_s

while β -RDX is C_{3v} .^{101, 113-115} The β -RDX increased molecular symmetry results in a decrease in the number of β -RDX Raman bands.¹¹³⁻¹¹⁶ We diagnosed that RDX on MgF_2 is α -RDX from the 1595 cm^{-1} (NO_2 asymmetric stretching) and 1032 cm^{-1} (N-C-N stretching) bands present only in α -RDX.¹¹⁴

We used X-ray photoelectron spectroscopy (XPS) to study the solid state RDX photolysis. DUVRR and XPS spectra were measured for a ~ 0.01 mg sample of RDX on a gold coated glass slide as discussed above. The DUVRR spectra of this sample resemble that of Figure 4.8.

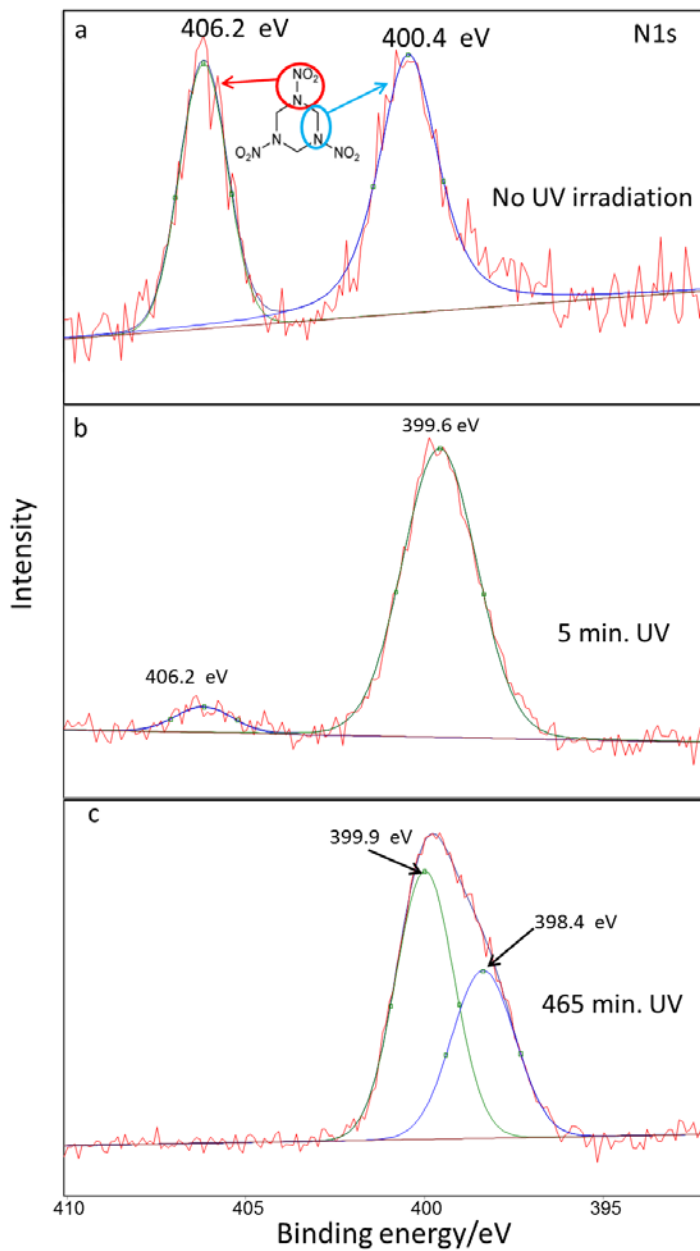


Figure 4.9: Nitrogen 1s electron XPS spectra of RDX (on a gold substrate) at different irradiation times: a) RDX with no UV irradiation, b) RDX after 5 min of UV irradiation, and c) RDX after 465 min of UV irradiation. The spectra were fit to Gaussian bands. The RDX sample was irradiated for 465 min with 5 mW of a CW 229 nm laser beam focused to a spot size of $\sim 300 \mu\text{m}$.

Figure 4.9a shows two distinct peaks for the N1s electrons of RDX. The peak at 406.2 eV is from the NO₂ group nitrogen electrons.^{117, 118} The peak at 400.4 eV comes from the ring nitrogen electrons.^{117, 118} The 406.2 eV peak intensity significantly decreases after 5 min of irradiation and disappears completely after 465 min irradiation, indicating the loss of the –NO₂ groups, which is consistent with the DUVRR (Figure 4.7). After 5 min irradiation, a peak at 399.6 eV is observed in Figure 4.9b that is attributed to sp² bonded nitrogen (C=N) electrons.¹¹⁹⁻¹²² After longer irradiation times, the spectrum resembles carbon nitride (Figure 4.9c).¹¹⁹⁻¹²² The 398.4 eV peak is assigned to CNC coordinated nitrogen of carbon nitride.¹²³

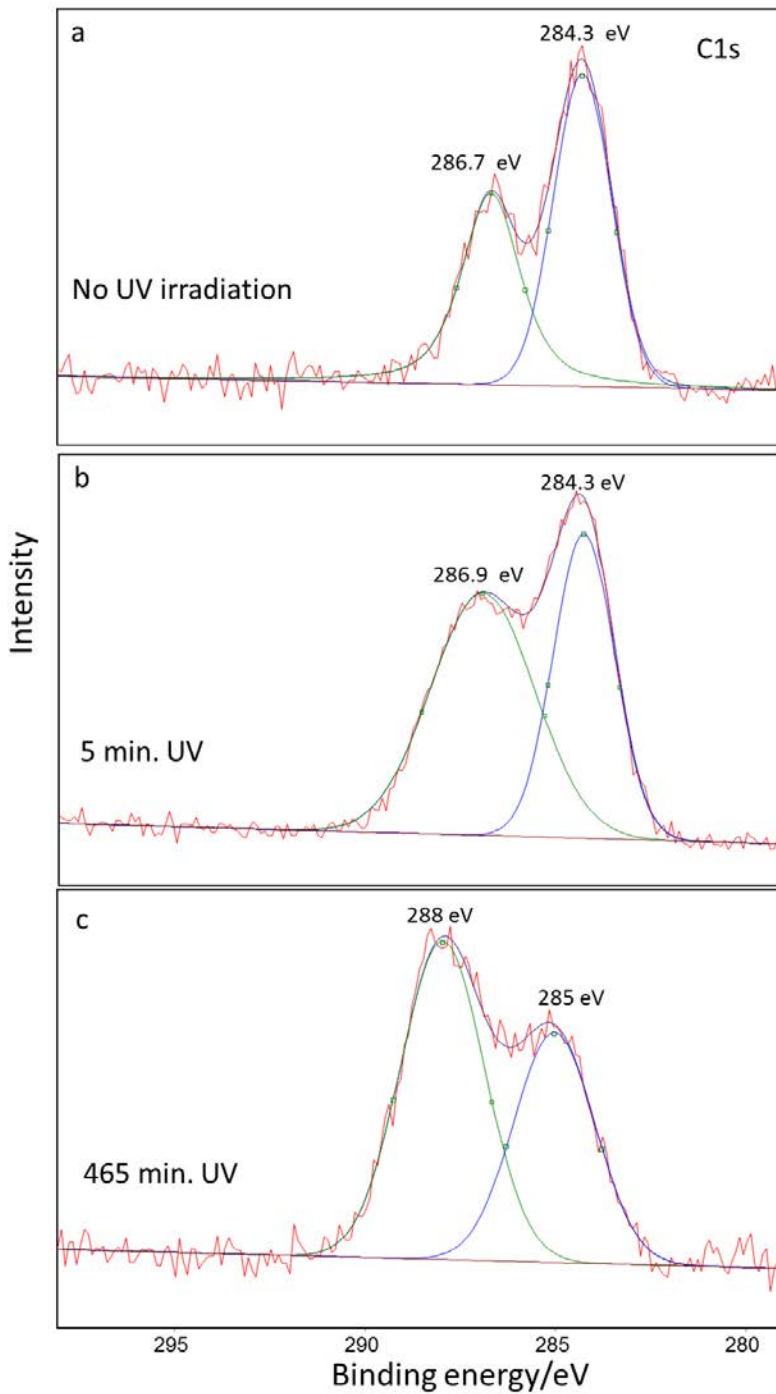


Figure 4.10: Carbon 1s electron XPS spectra of RDX (on a gold substrate) after different irradiation times: a) RDX without UV irradiation, b) RDX with 5 min of UV irradiation, and c) RDX with 465 min of UV irradiation. The spectra were fit to Gaussian bands. The RDX sample

was irradiated for 465 min with 5 mW of a CW 229 nm laser beam focused to a spot size of ~300 μm .

Figure 4.10a shows two peaks for the C1s electrons of RDX at 286.7 eV and 284.3 eV that are attributed to sp^3 carbon bonded to nitrogen (C-N) and graphitic carbon, respectively.^{121, 122} The C1s spectrum changes after irradiation with UV light. Spectrum b shows the 286.9 eV peak which is assigned to sp^2 bonded carbon (C=N).^{120, 122} Spectrum c shows a dominant peak at 288 eV which can be attributed to C-N-C coordination which is seen in carbon nitride.¹²³ The C1s and N1s spectra indicate that solid state RDX photolysis gives rise to carbon nitride-like photoproducts.

4.4 CONCLUSION

Solution state RDX in CD_3CN excited in resonance with 229 nm excitation quickly photolyzes with a quantum yield of $\phi \sim 0.35$ as determined by the HPLC-UV chromatography. DUVRR spectra show a loss of RDX bands and the appearance of photoproduct bands. The RDX 940 cm^{-1} band, which derives from N-N stretching, decreases and disappears over time indicating cleavage of the N-N bond. The RDX 1580 cm^{-1} band that involves O-N-O stretching, also decreases and disappears indicating the loss of the $-\text{NO}_2$ groups in the initial stages of photolysis. A 1044 cm^{-1} NO_3^- band appears indicating facile formation of NO_3^- which can serve as a signature of photolysis of RDX in solution.

We identified some of the solution state RDX photoproducts. The initial photoproducts are hexahydro-1-nitroso-3,5-dinitro-1,3,5-triazine (MNX), hexahydro-1,3-dinitroso-5-nitro-1,3,5-triazine (DNX), and hexahydro-1,3,5-trinitroso-1,3,5-triazine (TNX). After extensive

photolysis, NO_3^- is observed as a photoproduct in solution state photolysis. Thus, the NO_3^- band can be used as a signature of RDX photolysis in the solution state. The GCMS results show that formamide is also a photoproduct in the later stages of photolysis in the solution state. We do not detect formamide DUVRR spectra.

Solid RDX photodegrades quickly and shows cleavage of the N-N bonds and loss of the $-\text{NO}_2$ groups of RDX in the initial photolysis stages. XPS spectra further confirm this loss of $-\text{NO}_2$ groups. At late stages in the photolysis of solid state RDX, the DUVRR spectra show the formation of carbon nitride species. We also do not see formation of NO_3^- in the solid state photolysis.

4.5 ACKNOWLEDGEMENT

We would like to acknowledge Joel Gillespie for facilitating the X-ray photoelectron spectroscopy measurements. We would also like to acknowledge Steven Geib for the X-ray powder diffraction measurements. This work was funded by the Office of Naval Research (ONR) N00014-12-1-0021 contract.

5.0 UV RESONANCE RAMAN INVESTIGATION OF PENTAERYTHRITOL TETRANITRATE SOLUTION PHOTOCHEMISTRY AND PHOTOPRODUCT HYDROLYSIS

Adapted with permission from: “UV Resonance Raman Investigation of Pentaerythritol Tetranitrate Solution Photochemistry and Photoproduct Hydrolysis,” K.L. Gares, S.V. Bykov, and S.A. Asher, *Journal of Physical Chemistry A*, 2017, submitted.

Ultraviolet resonance Raman spectroscopy (UVRR) is being developed for standoff trace explosives detection. To accomplish this it is important to develop a deep understanding of the accompanying UV excited photochemistry of explosives, as well as the impact of reactions on the resulting photoproducts. In the work here we used 229 nm excited UVRR spectroscopy to monitor the photochemistry of pentaerythritol tetranitrate (PETN) in acetonitrile. We find that solutions of PETN in CD₃CN photodegrade with a quantum yield of 0.08 ± 0.02 , as measured by high performance liquid chromatography (HPLC). The initial step in the 229 nm UV photolysis of PETN in CD₃CN is cleavage of an O-NO₂ bond to form NO₂. The accompanying photoproduct is pentaerythritol trinitrate (PETriN), (CH₂ONO₂)₃CCH₂OH formed by photolysis of a single O-NO₂. The resulting UVRR spectra show a dominant photoproduct band at ~1308 cm⁻¹, which derives from the symmetric stretch of dissolved NO₂. This photoproduct NO₂ is hydrolyzed by trace amounts of water, which downshifts this 1308 cm⁻¹ NO₂ Raman band due to

the formation of molecular HNO₃. The dissociation of HNO₃ to NO₃⁻ in the presence of additional water results in an intense NO₃⁻ symmetric stretching UVRR band at 1044 cm⁻¹.

5.1 INTRODUCTION

Interest in explosives detection has dramatically increased due to the increasing number of terrorist attacks utilizing improvised explosive devices (IEDs).^{1-4, 8, 28, 29, 31, 32} It is essential to develop methods to detect explosives and to distinguish them from background interferences. Promising standoff detection methods are likely to involve laser spectroscopy methods^{18, 27-29, 31, 37-39, 41} that irradiate target surfaces and analyze the scattered or emitted light for evidence of explosive species.

Raman spectroscopy is a promising laser spectroscopy method for detection of explosives because it can detect their unique vibrational signatures. Normal Raman spectroscopy has already been used for explosive detection.^{3, 4, 18, 27-30, 32, 86, 124, 125} Unfortunately, trace detection of explosives, utilizing normal Raman, is impeded by the typically, small *normal* Raman cross sections of explosives. UV resonance Raman spectroscopy (UVRR) can be used to dramatically increase these Raman cross sections, which can dramatically increase the spectral sensitivity for detection of trace explosives.

UVRR spectroscopy shows great promise as a sensitive technique for trace explosive detection.^{2, 27, 28, 31, 37-39, 41, 47} Most explosives show deep UV absorption bands below 260 nm.^{28, 31} Excitation of resonance Raman spectra also result in the absorption of numerous UV photons since the absorption cross sections exceed resonance Raman cross sections by ~10⁸-fold. Analytes cycle through their electronic excited states myriad times prior to Raman scattering.

During this absorption and relaxation cycling, the analyte can undergo photolysis, which can decrease its concentration. This photochemistry can also produce new photochemical species. The resulting UVRR will show characteristic spectral changes due to this analyte depletion and photoproduct formation. We previously demonstrated the impact of photochemistry in the resonance Raman studies of nitrates, TNT, and RDX.^{37-39, 51} We also showed that these photochemically produced UVRR spectral changes provide additional information that can aid in identifying analytes.

In the work here, we investigated the 229 nm UVRR solution state photochemistry of the explosive pentaerythritol tetranitrate (PETN). We determined the PETN photochemical quantum yield and identified the initial photoproducts formed.

We base some of the observed photochemistry on the extensive previous studies of photolysis of nitrate esters in the gas phase.⁶⁷ This previous work was previously motivated by the need to characterize the nitrogen oxides formed during atmospheric photochemistry.⁶⁷ Most of these studies used excitation wavelengths $\lambda > 290$ nm, a region of very weak absorption.⁶⁷ For nitrate esters excited at $\lambda > 290$ nm, photolysis involves cleavage of the O-NO₂ bond to form NO₂ and an alkoxy radical.⁶⁷⁻⁷¹

We examined PETN photochemistry with 229 nm excitation, a region of strong absorption. In some of the discussion here, it appears that the tail of the absorption band excited with $\lambda > 290$ nm light involves the same electronic transition that shows strong absorption with a maximum at ~ 200 nm. Our results seem consistent with the expectation that 229 nm excitation photochemistry and the $\lambda > 290$ nm atmospheric photochemistry have identical mechanisms and photoproducts.

5.2 EXPERIMENTAL

5.2.1 PETN Solution State UVRR

5.2.1.1 Raman Instrumentation

The UVRR instrumentation was described previously.^{87, 88} A Coherent Industries Innova 300 FreD frequency doubled Ar⁺ laser generates 229 nm continuous wave (CW) light. A Spex Triplemate spectrograph was used to disperse the Raman scattered light, which was detected by a Princeton Instruments CCD camera (Spec-10).

5.2.1.2 UVRR Measurements

The 2 mL, 1 mg/mL PETN in CD₃CN sample used for UVRR measurements was obtained by evaporating a 2 mL sample of 1 mg/mL PETN in CH₃CN (Cerilliant). The PETN was then redissolved in 2 mL of CD₃CN (Acros Organics). The samples were measured in a 1 cm path length fused silica capped cuvette with a magnetic stir bar. The 229 nm UVRR were excited with an ~80 μm spot size laser beam.

The PETN sample was photolyzed by an unfocused ~10 mW 229 nm CW laser beam for the times necessary to achieve absorption of 0.5, 1, 3, 5, 11, 16 photons per molecule (phot/molc).³⁸ The UVRR of the samples were measured after each irradiation period by exciting the UVRR with ~4 mW of a ~80 μm spot size focused beam. The calculated total absorbed phot/molc includes the irradiation during the UVRR measurements. Quartz and CD₃CN UVRR spectral contributions were numerically subtracted. A 25 μL aliquot of these photolyzed samples was used for the quantum yield determination using HPLC-HRMS.

5.2.1.3 Absorption Measurements

The absorption spectra of the irradiated PETN/CD₃CN samples were measured in a capped 1 cm path length fused silica cuvette by using a Varian Cary 5000 UV-Vis/near-infrared (NIR) spectrometer.

A 3 mL, 1 mg/mL PETN in CD₃CN sample was used for the photolysis absorption measurements. The sample was obtained by evaporating a 3 mL sample of 1 mg/mL PETN in CH₃OH (Accustandard). The PETN was then redissolved in 2 mL of CD₃CN (Acros Organics). The sample was irradiated in a capped 1 cm path length fused silica cuvette. The PETN was irradiated by an unfocused ~10 mW 229 nm CW laser beam for the times necessary to achieve absorption of 0.5, 1, 3, 5, 11, 16 phot/molc.³⁸ The absorption spectra were then measured.

5.2.1.4 PETN Photolysis Quantum Yield

HPLC-HRMS was used to determine the solution state quantum yield of the PETN photolysis. A reversed phase 100 x 2 mm Phenomenex Luna HPLC column with 3 μm C-18 silica particles was utilized for HPLC measurements. The loss of PETN during photolysis was determined from the area of the PETN + formate adduct peak in photolyzed solutions. This peak elutes at 8.3 min with a 361 m/z as measured with UV detection. A calibration curve was determined by measuring HPLC of calibration standards of 1, 0.5, 0.25, 0.13, 0.063 mg/mL solutions of PETN in CD₃CN. This calibration curve was used to determine PETN concentrations within the irradiated PETN samples.

5.2.2 UVRR and Absorption Studies of NO₂ Hydrolysis in Acetonitrile

The presence of water significantly alters the PETN photoproduct distributions. We examined this dependence by using UVRR and absorption spectra of solutions of NO₂ with varying concentrations of water.

To obtain NO_{2(g)}, ~10 g of Pb(NO₃)₂ was placed into a round bottom flask and heated with a Meker-Fisher burner until decomposition occurred, forming NO_{2(g)}.¹²⁶ The NO_{2(g)} was drawn up into a syringe and bubbled into 3 mL of CD₃CN (Acros). Varying concentrations of water were added to the NO₂/CD₃CN sample (0, 0.1, 0.5, 1, 3, and 5 % H₂O by volume). These samples were excited with ~5 mW of CW 229 nm light for the UVRR measurements. The absorption was measured for each sample in a 1 cm path length fused silica cuvette.

5.3 RESULTS

5.3.1 PETN Photolysis

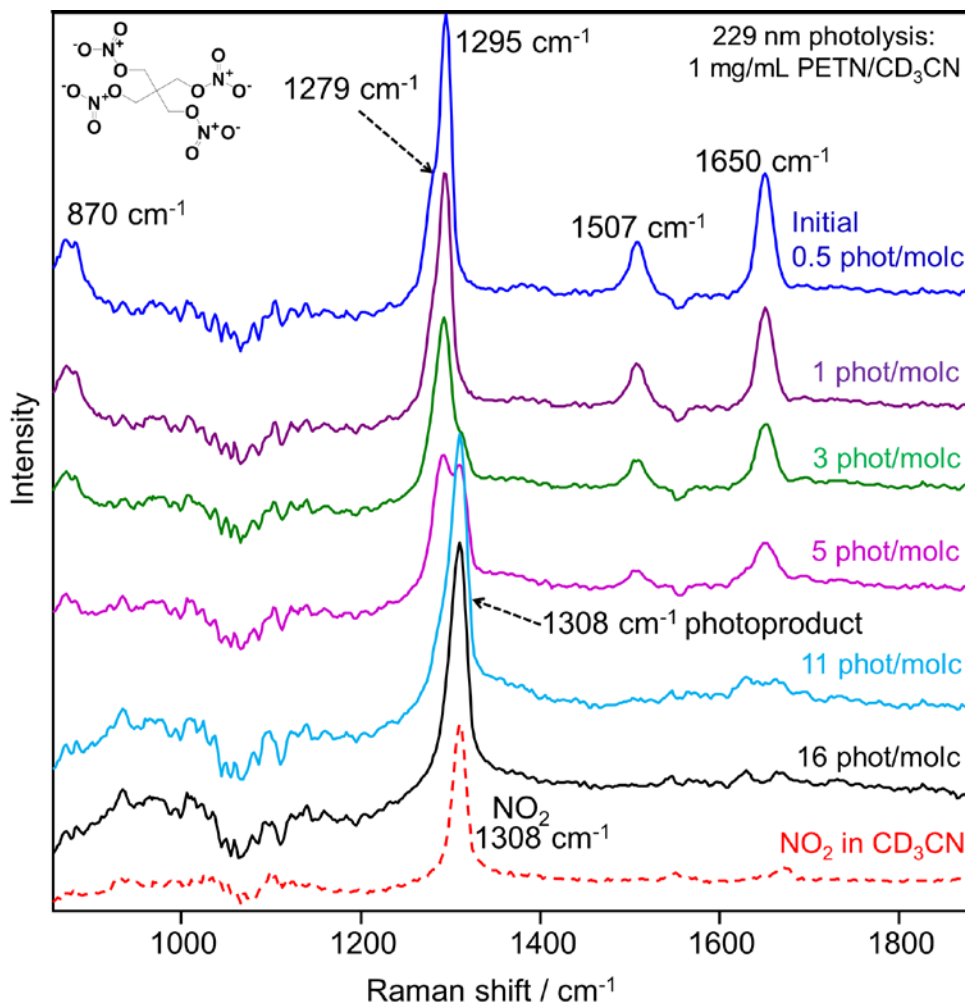


Figure 5.1: 229 nm UVRR of PETN in CD₃CN with increasing irradiation times (absorbed photons per molc). The NO₂ in CD₃CN spectrum shows the NO₂ Raman band at 1308 cm⁻¹. CD₃CN and quartz UVRR bands were subtracted.

Figure 5.1 shows the UVRR spectra of PETN in CD₃CN as the irradiation time increases. The initial PETN UVRR spectra show PETN UVRR bands at 869 cm⁻¹ (O-N stretching and C-C

stretching), at 1279 cm^{-1} (C_5 skeletal and CH bending), at 1295 cm^{-1} ($-\text{NO}_2$ symmetric stretch with CH_2 wagging), at 1507 cm^{-1} (CH_2 scissoring), and at 1650 cm^{-1} ($-\text{NO}_2$ asymmetric stretching).^{28, 31, 127, 128} The initial UVRR PETN spectrum with minimal irradiation shows negligible contributions of photoproducts.

The PETN Raman band intensities monotonically decrease as the irradiation time increases. The 5 phot/molc PETN UVRR spectrum clearly shows a new strong overlapping photoproduct Raman band at 1308 cm^{-1} . At longer irradiation times, the PETN 1295 cm^{-1} Raman band intensity continues to decrease, while the 1308 cm^{-1} photoproduct Raman band intensity increases. There is clearly an extensive photolysis of PETN at 16 phot/molc, where the photoproduct 1308 cm^{-1} Raman band dominates.

Figure 5.1 also shows the UVRR spectrum of pure NO_2 dissolved in CD_3CN . The UVRR shows that the dominating NO_2 symmetric stretch Raman band occurs at 1308 cm^{-1} in CD_3CN . Thus, Figure 5.1 allows us to conclude that NO_2 is a PETN photoproduct of 229 nm excitation.

We used HPLC-HRMS to study the photoproducts formed during PETN photolysis. In the early stages of photolysis (1 phot/molc), we observe a photoproduct that has the m/z value of 316, which is pentaerythritol trinitrate (PETriN), $(\text{CH}_2\text{ONO}_2)_3\text{CCH}_2\text{OH}$ + formate adduct. Studies measuring PETN using electrospray ionization in the negative ion mode in liquid chromatography mass spectrometry (LCMS) have shown that nitrate esters form adduct ions rather than molecular ions.¹²⁹ PETriN results from cleavage of a single O- NO_2 bond of PETN, $\text{C}(\text{CH}_2\text{ONO}_2)_4$. PETriN has been observed as a post explosion degradation product of PETN.^{130,}

¹³¹ Other minor photoproduct peaks are also observed with HPLC-HRMS.

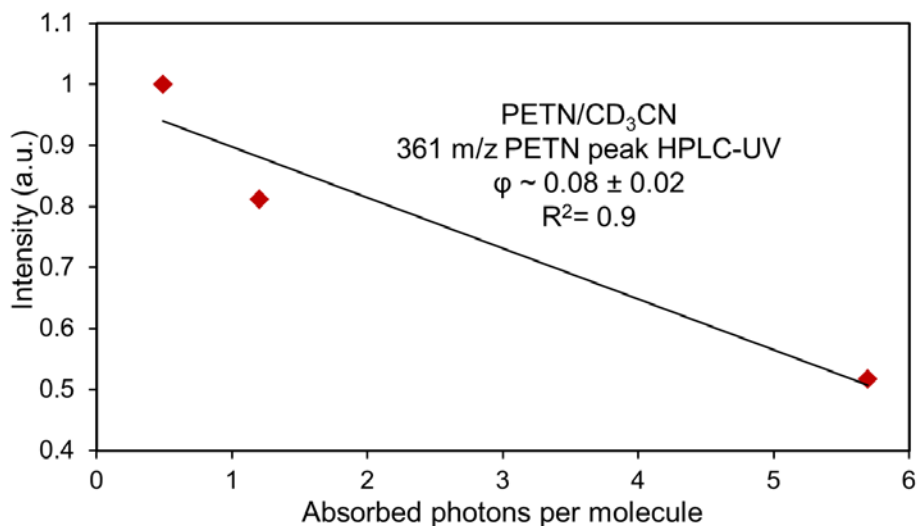


Figure 5.2: PETN photolysis quantum yield measurements. Dependence of PETN 361 m/z peak intensity measured by HPLC-UV on the number of absorbed phot/molc during initial stages of photolysis in the absence of water. The quantum yield is determined from the slope.

We determined the photochemical quantum yield of PETN in CD₃CN by using HPLC to monitor the dependence of the 361 m/z PETN+ formate adduct peak intensity on the number of absorbed photons/molc (Figure 5.2). The measurements used a HPLC-HRMS calibration curve for PETN in CD₃CN. We calculate a quantum yield of $\phi = 0.08 \pm 0.02$.

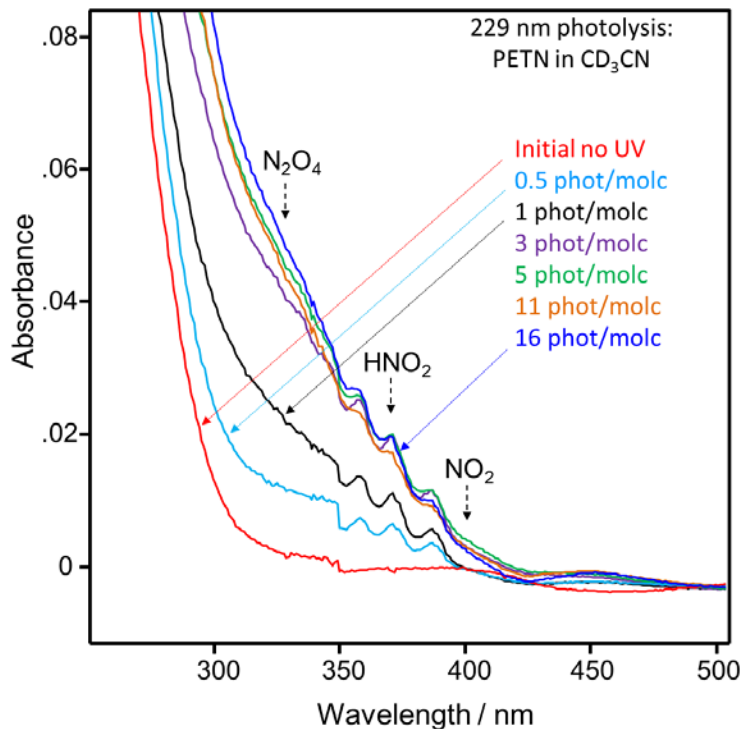


Figure 5.3: Absorption spectra of PETN in CD₃CN (1 cm path length) upon 229 nm irradiation of 0.5, 1, 3, 5, 11, and 16 absorbed phot/molc.

Figure 5.3 shows the dependence of the PETN absorption spectrum on increasing 229 nm light absorption. PETN has an absorption maximum at ~ 200 nm that derives from two $\pi \rightarrow \pi^*$ electronic transitions at ~ 208 nm and ~ 187 nm localized on each of the four PETN O–NO₂ groups.¹³² During photolysis an increase in absorption occurs between 300–350 nm which derives from formation of N₂O₄, a dimer of NO₂. The dimer is in equilibrium with the monomer photoproduct, NO₂. The NO₂ absorption maximum occurs at ~ 400 nm.¹³³ In addition, a series of sharp absorption features are observed between 350–400 nm that derive from nitrous acid (HNO₂). We hypothesize that the nitrous acid results from the reaction of NO₂ with trace amounts of water.^{126, 134, 135}

The presence of water significantly alters the PETN photoproduct UVRR spectra. We find that under humid lab conditions the 1308 cm^{-1} photoproduct UVRR band of Figure 5.1 downshifts due to NO_2 hydrolysis.

5.3.2 Hydrolysis of NO_2 Photoproduct in CD_3CN

We investigated the hydrolysis of NO_2 by measuring the absorption and UVRR of NO_2 in the presence of different volume fractions of water (Figure 5.4 and Figure 5.5).

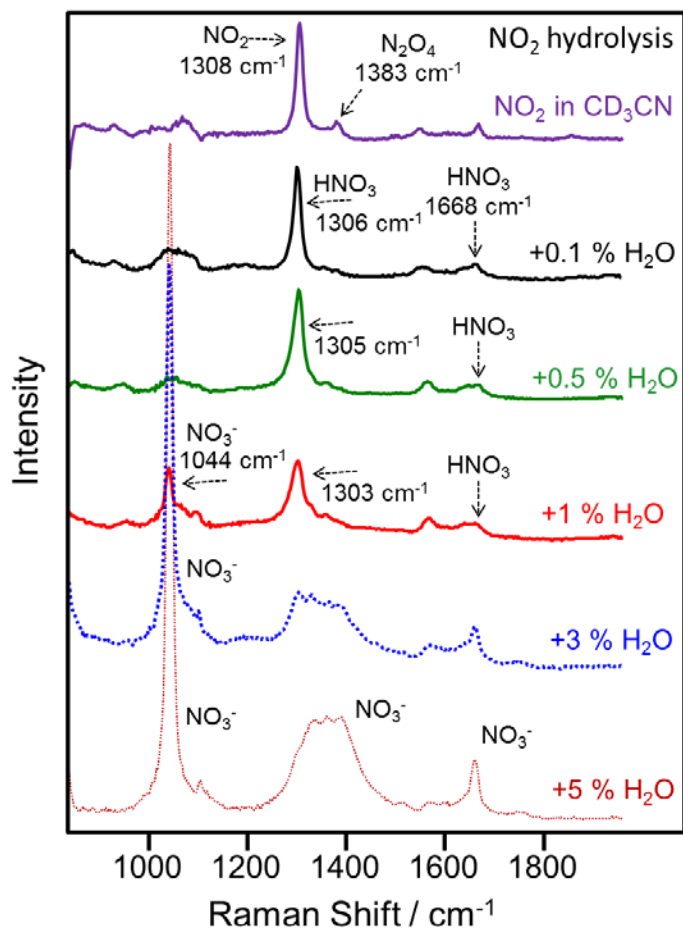
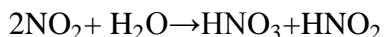


Figure 5.4: UVRR excited at 229 nm of NO_2 dissolved in CD_3CN with addition of 0.1, 0.5, 1, 3, 5 % volume fractions of H_2O . The spectra are normalized to the 2061 cm^{-1} band of CD_3CN .

Quartz and CD₃CN Raman bands are subtracted. This sample was also used for the absorption measurements of Figure 5.5.

Figure 5.4 shows the UVRR spectra of NO₂ dissolved in CD₃CN at increasing volume fractions of H₂O. The NO₂ spectrum without H₂O added shows the NO₂ symmetric stretching Raman band at 1308 cm⁻¹, and a N₂O₄ Raman band at ~1383 cm⁻¹(coupled NO₂ symmetric stretching).¹³⁶

At 0.1 % volume fraction of H₂O, we observe that the 1308 cm⁻¹ NO₂ Raman band is downshifted to 1306 cm⁻¹. We assign this 1306 cm⁻¹ band to the symmetric stretching vibration of undissociated HNO₃,¹³⁷ as clearly shown by the Figure 5.5 absorption spectra and discussion below. We also observe the HNO₃ asymmetric stretching Raman band at ~1668 cm⁻¹ in the Figure 5.4 0.1 % volume fraction H₂O UVRR spectrum.¹³⁷ HNO₃ is formed by the reaction between NO₂ and H₂O at room temperature,^{126, 134, 135, 138, 139}



The HNO₂ photoproduct is observed in the Figure 5.5 absorption measurements. We do not observe UVRR HNO₂ bands likely because they have small Raman cross sections.

The HNO₃ vibrational frequencies depend on interactions with the solvent. The frequency dependence in wet solvents is probably dominated by water hydrogen bonding.^{137, 140-143} We observe that, with increasing water concentration, the HNO₃ 1306 cm⁻¹ Raman band (0.1 % H₂O) downshifts to 1305 cm⁻¹ (0.5 % H₂O). This Raman band then further downshifts to 1303 cm⁻¹ (1 % H₂O) likely due to increased water hydrogen bonding to HNO₃. At ~1% H₂O, HNO₃ begins to dissociate to nitrate (NO₃⁻) as indicated by the appearance of the NO₃⁻ symmetric stretching Raman band at 1044 cm⁻¹.^{37, 51} The NO₃⁻ 1044 cm⁻¹ Raman band is first observed at 1 % volume

fraction water concentration with an intensity close to that of the HNO_3 Raman band at 1303 cm^{-1} .

The NO_3^- concentration dramatically increases with water concentration as indicated by the dominating 1044 cm^{-1} Raman band intensity in the 3 and 5 % water spectra. In the 5 % H_2O spectrum, the NO_3^- 1044 cm^{-1} Raman band becomes ~ 5 times more intense than the NO_2 1308 cm^{-1} Raman band if no H_2O is present.

This is an important result for UVRR detection of PETN because NO_3^- is the ultimate photoproduct in the presence of H_2O , and NO_3^- shows a dominating UVRR cross section. We do not observe the nitrite (NO_2^-) photoproduct because the weak acid HNO_2 will not dissociate under these conditions to form NO_2^- .¹²⁶

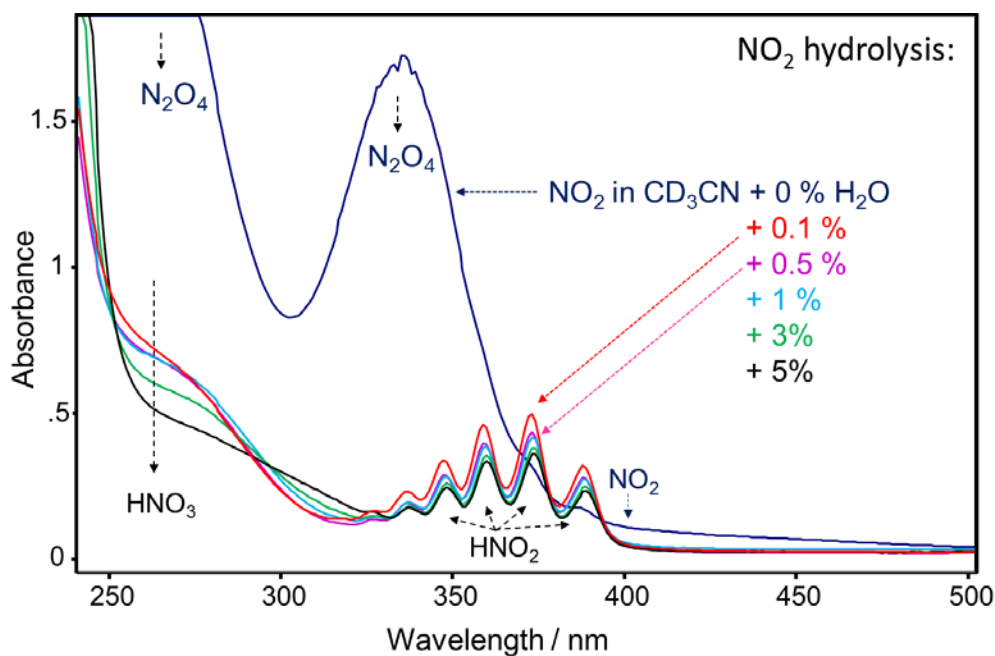


Figure 5.5: Absorption spectra of NO_2 dissolved in CD_3CN at increasing volume fractions of H_2O (0.1, 0.5, 1, 3, and 5 %) measured using a 1.0 cm path length cuvette. This is the same sample used for the UVRR measurements of Figure 5.4.

Figure 5.5 shows that the absorption spectrum of NO_2 dissolved in CD_3CN is dominated by the N_2O_4 dimer absorption, which has a strong gas phase absorption maximum at ~ 340 nm.¹⁴⁴⁻¹⁴⁶ NO_2 gives rise to a broad absorption band with a maximum at ~ 400 nm.^{133, 146} NO_2 and N_2O_4 coexist in equilibrium in acetonitrile.^{134, 147} See Appendix C for the absorption spectrum of the gaseous monomer NO_2 and gaseous N_2O_4 . A larger absorption is observed for N_2O_4 in Figure 5.5 compared to that of NO_2 because the dimer is favored in CD_3CN solution.¹⁴⁷

The N_2O_4 and NO_2 absorption bands essentially disappear upon addition of 0.1 % H_2O , indicating conversion of N_2O_4 and NO_2 to HNO_2 and HNO_3 . Undissociated HNO_3 shows an absorption maximum at ~ 260 nm, which derives from an $n \rightarrow \pi^*$ transition.¹⁴⁸⁻¹⁵⁰ This absorption band decreases in intensity as the water concentration increases, indicating HNO_3 dissociation, which agrees with the UVRR spectra that show intense bands of NO_3^- . HNO_2 shows distinct absorption bands between ~ 300 - 400 nm (Figure 5.5).¹⁵¹⁻¹⁵³ See Appendix C for the absorption spectrum of gaseous HNO_2 . In contrast to HNO_3 , the HNO_2 bands persist with increasing concentration of water because HNO_2 does not dissociate in the presence of the strong acid, HNO_3 .

5.4 CONCLUSION

We examined the 229 nm photochemistry of PETN dissolved in CD_3CN . The initial photolysis of PETN involves loss of one of the four nitrate ester, ($-\text{ONO}_2$), groups forming the photoproducts PETriN [$(\text{CH}_2\text{ONO}_2)_3\text{CCH}_2\text{OH}$] and NO_2 . We measure a quantum yield for PETN/ CD_3CN photolysis of $\phi \sim 0.08 \pm 0.02$. The UVRR spectra of PETN/ CD_3CN show a decrease in the PETN Raman band intensities upon photolysis and the appearance of a photoproduct Raman band at

1308 cm^{-1} , which results from the symmetric stretch of dissolved NO_2 . Absorbance measurements show that NO_2 and its dimer N_2O_4 coexist in equilibrium in CD_3CN .

The NO_2 photoproduct undergoes hydrolysis in the presence of trace amounts of water forming HNO_3 and HNO_2 . The 1308 cm^{-1} NO_2 photoproduct Raman band downshifts to 1306 cm^{-1} upon conversion to HNO_3 . This Raman band further downshifts to 1303 cm^{-1} upon an increase in water concentration likely due to increased water hydrogen bonding to the HNO_3 . At higher water concentrations HNO_3 dissociates to form NO_3^- . The very large UVRR 229 nm cross section of the NO_3^- symmetric stretch causes this band to dominate the UVRR of PETN in the presence of trace water.

5.5 ACKNOWLEDGEMENT

We gratefully acknowledge funding from ONR grants N00014-12-1-0021 and N00014-16-1-2681.

6.0 DISSERTATION SUMMARY

We have demonstrated that UV resonance Raman (UVR) is a powerful technique for examining the photochemistry of explosives. We have developed detection methodologies and gained photochemical insights that will aid in the detection of explosives. We have shown that UVR can be utilized to analyze characteristic spectral changes due to photoproduct formation. By examining the photochemistry, we can identify the photoproduct Raman bands which increase in intensity and the explosive analyte Raman bands which decrease in intensity over time. We can determine the identity of the explosive analyte even after the explosive is photolyzed because of the characteristic photoproduct Raman bands. Furthermore, excitation in the deep UV (229 nm) allows for a large increase in intensity of the Raman bands of the explosives and larger Raman cross sections. This allows for increased sensitivity and selectivity which will enable detection of explosives and their photochemical products.

We examined the 229 nm photochemistry of TNT, RDX, and PETN. Quantum yields were determined for each explosive. TNT has a solution state quantum yield of $\phi = 0.015$. Solution state RDX in CD_3CN quickly photolyzes with a quantum yield of $\phi \sim 0.35$, with 229 nm excitation. PETN has a solution state quantum yield of $\phi \sim 0.08 \pm 0.02$. These explosives all absorb in the deep UV and are quickly photolyzed when exposed to 229 nm irradiation.

We examined the 229 nm UVR spectra for TNT, RDX, and PETN photolysis. For TNT photolysis, we determined that the TNT signature band at 1210 cm^{-1} in the solution state and

1202 cm^{-1} in the solid state derives from a symmetric aromatic ring breathing motion that is unique to the symmetry of the TNT molecule. The intensities of the photoproduct Raman bands slowly decrease and persist over time. These photoproduct Raman bands mainly involve $-\text{NO}_2$ stretching vibrations and have contribution from TNT and its photoproducts. These photoproduct Raman bands enable detection of TNT and its photoproducts even after TNT has been photolyzed. We see a similar TNT photolysis in the solid state.

The RDX photolysis UVRR spectra show a decrease in intensity of the initial RDX bands with the appearance of photoproduct bands in both solution and solid state RDX photolysis. The 940 cm^{-1} band of RDX, which derives from N-N stretching, decreases and disappears over time indicating cleavage of the N-N bond of RDX which indicates loss of $-\text{NO}_2$ groups in the initial stages of photolysis. The solution UVRR spectra show a photoproduct band at 1044 cm^{-1} which derives from the symmetric stretching vibration of NO_3^- . The solid state photolysis of RDX also shows cleavage of the N-N bonds indicating the loss of the $-\text{NO}_2$ groups in the initial stages of photolysis, similar to the solution state photolysis.

The 229 nm photochemistry of PETN dissolved in CD_3CN was investigated. In the initial stages of photolysis, PETN loses one of the four nitrate ester, ($-\text{ONO}_2$), groups forming the photoproducts PETriN $[(\text{CH}_2\text{ONO}_2)_3\text{CCH}_2\text{OH}]$ and NO_2 . The UVRR spectra show the initial PETN Raman bands decrease in intensity upon photolysis and a photoproduct Raman band at 1308 cm^{-1} appears and increases in intensity. This photoproduct Raman band results from the symmetric stretching vibration of dissolved NO_2 . We also observed that the NO_2 photoproduct of PETN undergoes hydrolysis in the presence of trace amounts of water. This results in the formation of HNO_2 and HNO_3 . The HNO_3 dissociates to NO_3^- at higher water concentrations as

observed with the 1044 cm^{-1} symmetric stretch of NO_3^- , which dominates the UVRR of PETN in the presence of water.

Finally, we determined the composition of the initial photoproducts in each of these photolysis mechanisms. We utilized high performance liquid chromatography-high resolution mass spectrometry (HPLC-HRMS) to determine the initial photoproducts. Some of the initial photoproducts for TNT photolysis are 2-amino-4,6-dinitrotoulene, 3,5-dinitroaniline, and 2,5-dinitrophenol. For RDX photolysis, we determined the initial photoproducts as the mono-, di-, and tri-nitroso derivatives (MNX, DNX, and TNX) of RDX. HPLC-HRMS also indicated that NO_3^- is a photoproduct after extensive photolysis of solution state RDX. PETN photolysis forms the initial photoproduct pentaerythritol trinitrate (PETriN), $(\text{CH}_2\text{ONO}_2)_3\text{CCH}_2\text{OH}$, as determined with HPLC-HRMS. This photoproduct results from cleavage of a single O- NO_2 bond of PETN.

The combined results from the UVRR studies of the photochemistry of TNT, RDX, and PETN demonstrate that UVRR is an incisive method for detection of explosives and their photoproducts. UVRR has the ability to monitor spectral changes due to photolysis. We have shown that characteristic photoproduct UVRR bands allow for detection of these explosives even after they have been photolyzed. Fundamentally understanding the photochemistry of these explosive molecules is vital in developing detection methodologies.

APPENDIX A

A.1 SUPPORTING INFORMATION FOR CHAPTER 3

A.1.1 Solution MS/MS

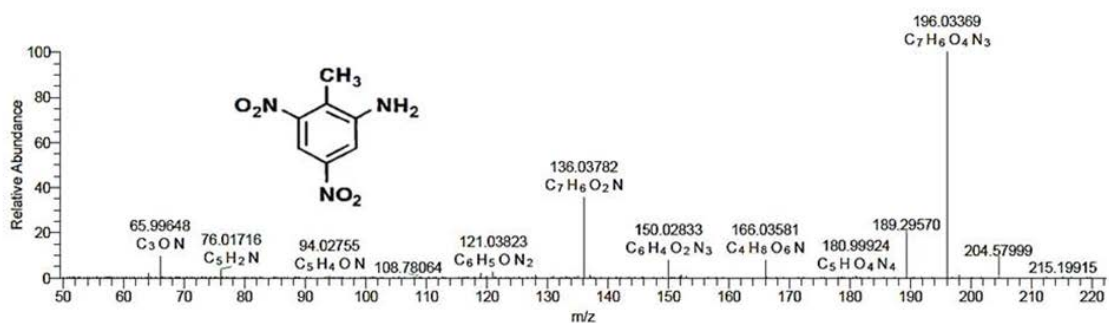


Figure A1: MS/MS of the standard 1 mg/mL 2-amino-4,6-dinitrotoluene in CH₃CN.

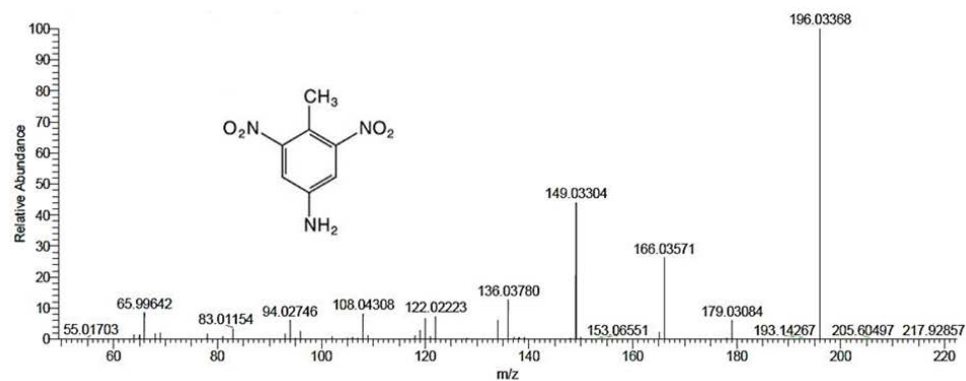


Figure A2: MS/MS of the standard 1 mg/mL 4-amino-2,6-dinitrotoluene in CH₃CN. The 149 m/z peak distinguishes it from its isomer 2-amino-4,6-DNT.

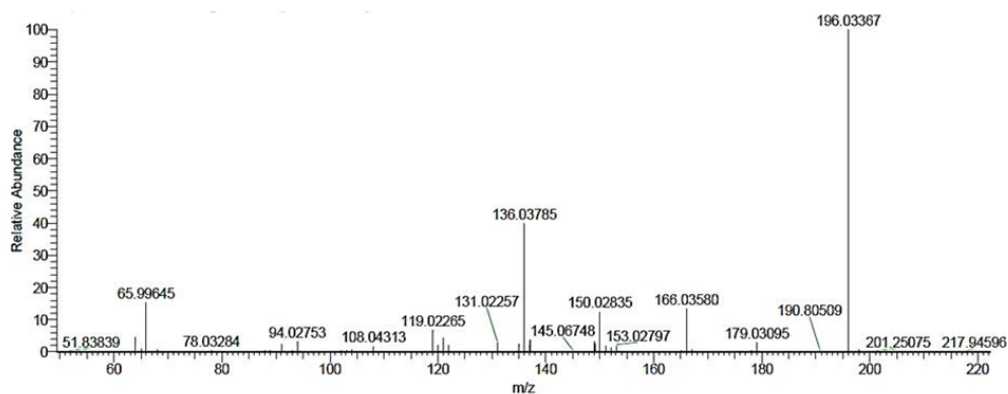


Figure A3: MS/MS of 196 m/z peak from the TNT irradiated samples, retention time of 7.1 min.

The MS/MS of the 196 m/z peak in the TNT irradiated samples (Fig. A3) matches the MS/MS of the standard 2-amino-4,6-DNT (Fig. A1). 2-amino-4,6-DNT was determined to be one of the initial photoproducts forming.

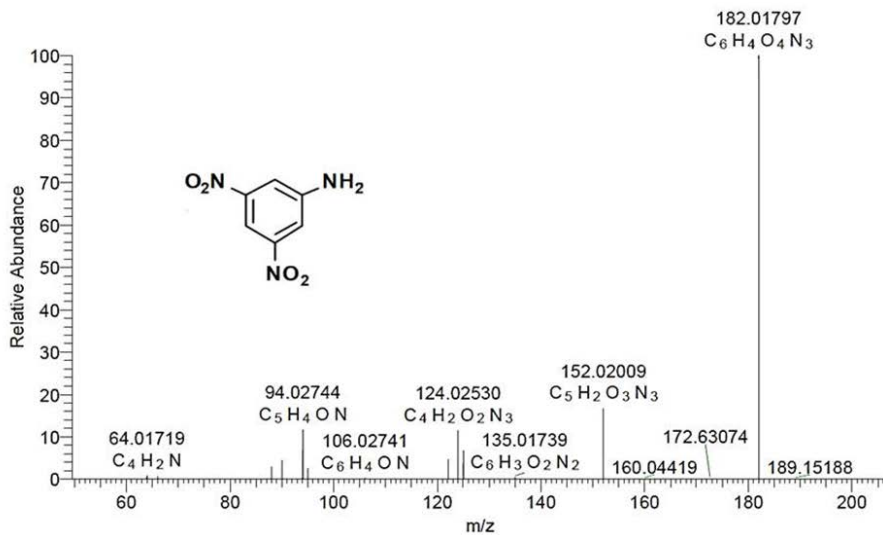


Figure A4: MS/MS of the standard 1 mg/mL 3,5-dinitroaniline in CH₃CN

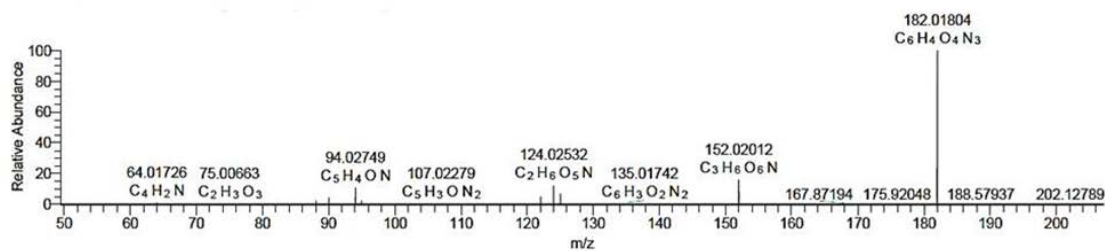


Figure A5: MS/MS of 182 m/z peak from the TNT irradiated samples, retention time of 3.5 min.

The MS/MS of the 182 m/z peak in the TNT irradiated samples (Fig. A5) matches the MS/MS of the standard 3,5-dinitroaniline (Fig. A4). This confirmed that 3,5-dinitroaniline is one of the initial photoproducts in the TNT photolysis.

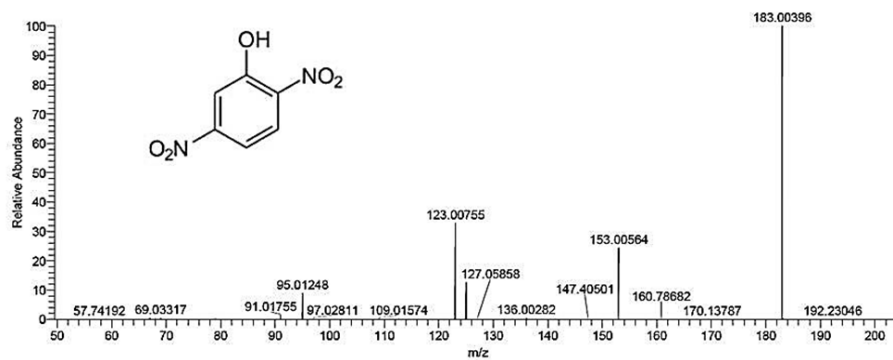


Figure A6: MS/MS of standard 2,5-dinitrophenol in water.

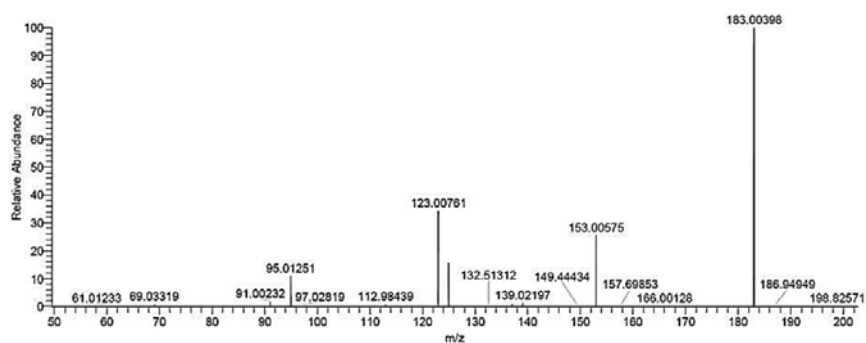


Figure A7: MS/MS of 183 m/z peak from TNT irradiated samples, retention time of 5.1 min.

The MS/MS of the 183 m/z peak in the TNT irradiated samples (Fig. A7) matches the MS/MS of the standard 2,5-dinitrophenol (Fig. A6). This confirmed that 2,5-dinitrophenol is one of the initial photoproducts in the TNT photolysis.

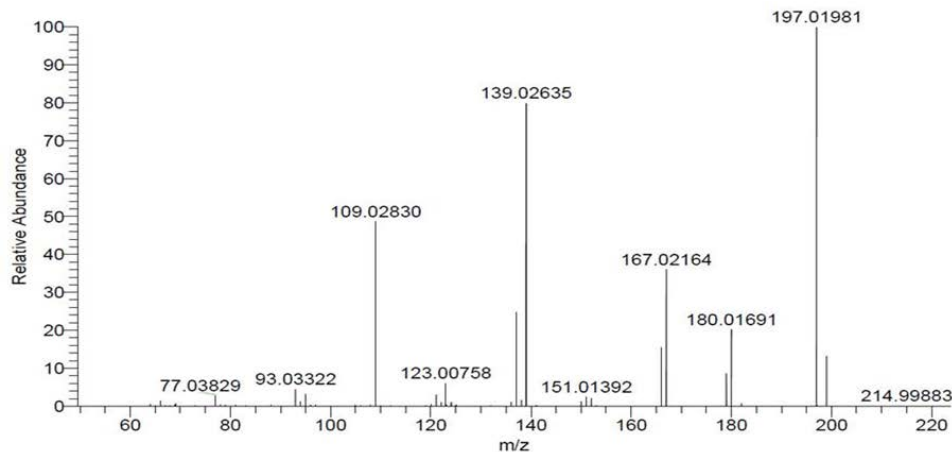


Figure A8: MS/MS of 197 m/z peak from TNT irradiated samples, retention time of 11.7 min.

Figure A8 shows the MS/MS of the 197 m/z compound that most likely results from a dinitrobenzyl alcohol.

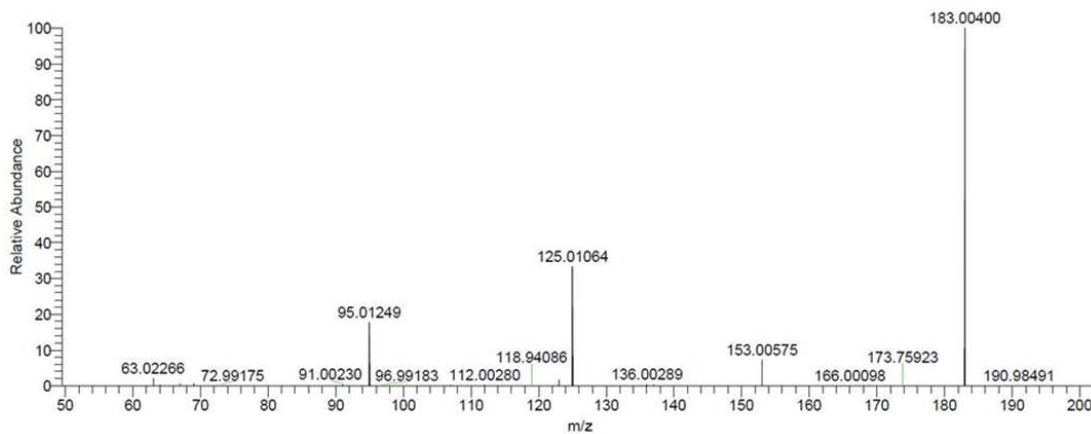


Figure A9: MS/MS of 183 m/z peak from TNT irradiated samples, retention time 7.4 min.

Figure A9 shows the MS/MS of the 183 m/z peak at 7.4 min. in the TNT irradiated samples.

A.1.2 Solid Mass Spectra

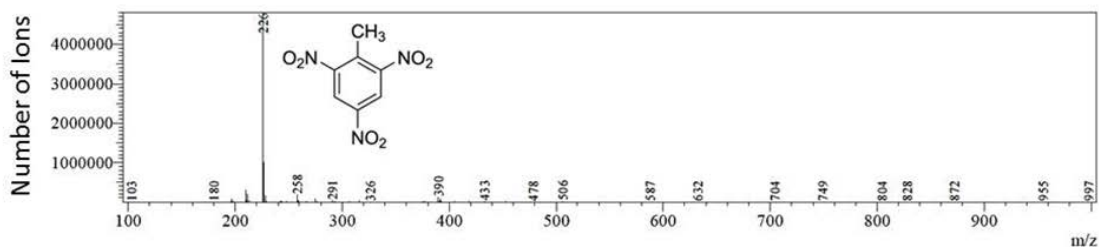


Figure A10: Mass spectrum of initial solid TNT sample showing 226 m/z peak, 11.980 min. retention time.

The initial mass spectrum of solid TNT (Fig. A10) shows the TNT peak at 226 m/z at a retention time of 11.980 min.

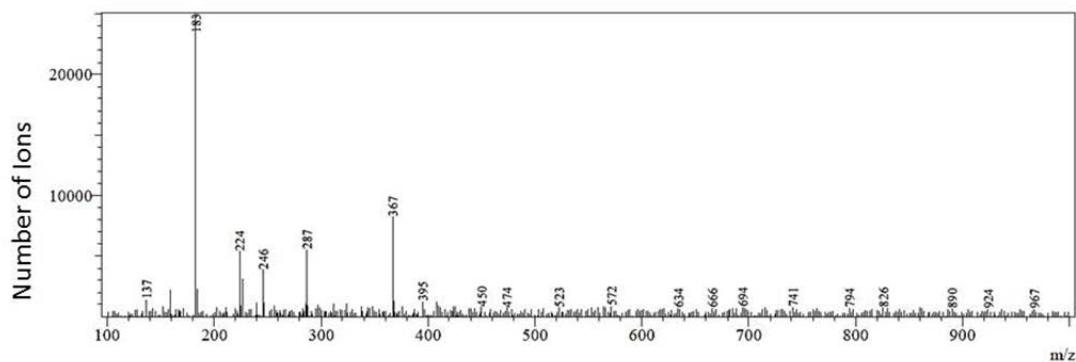


Figure A11: Mass spectrum of the 10 min. irradiated solid TNT sample: 183 m/z peak, 10.592 min. retention time.

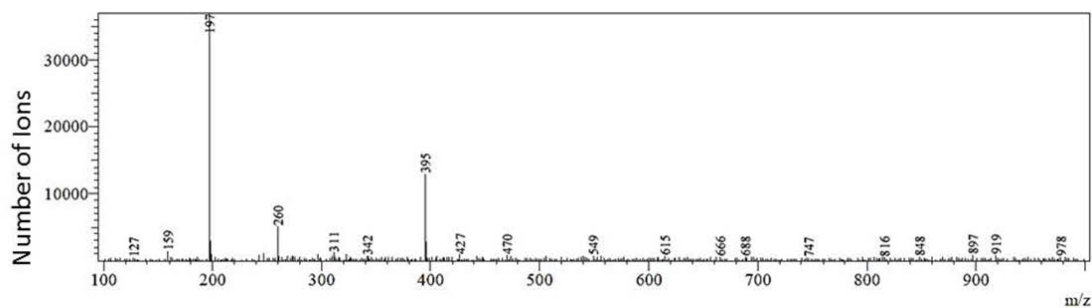


Figure A12: Mass spectrum of the 10 min. irradiated solid TNT sample: 197 m/z peak, 11.395 min. retention time.

The 183 m/z peak in the solid state (Fig. A11) and the 197 m/z peak (Fig. A12) for the solid state are also seen in the solution MS/MS data.

APPENDIX B

B.1 SUPPORTING INFORMATION FOR CHAPTER 4

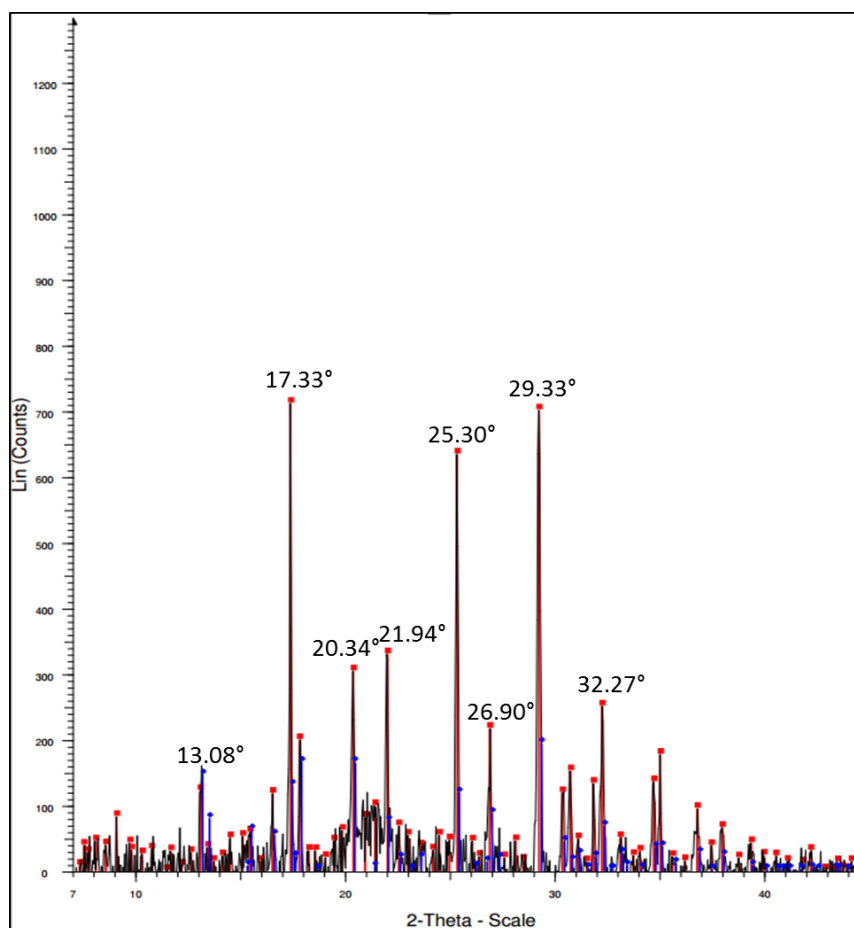


Figure B1: Diffraction pattern of RDX on the SiO₂ substrate. The blue diffraction pattern is the PDF entry of α -RDX from the database. The black diffraction pattern is the raw data of the RDX on SiO₂ substrate and the red is the peaks identified by the Bruker Eva software program. There

is overlap of the blue PDF entry of α -RDX from the database and the black raw data of RDX on SiO_2 substrate.

The measured RDX x-ray powder pattern is in excellent agreement with the PDF (Powder Diffraction File) entry 00-044-1619, which is from the alpha form of RDX with unit-cell parameters of $a= 13.192$, $b= 11.592$, $c= 10.709$, and $\alpha=\beta=\gamma=90$ deg.

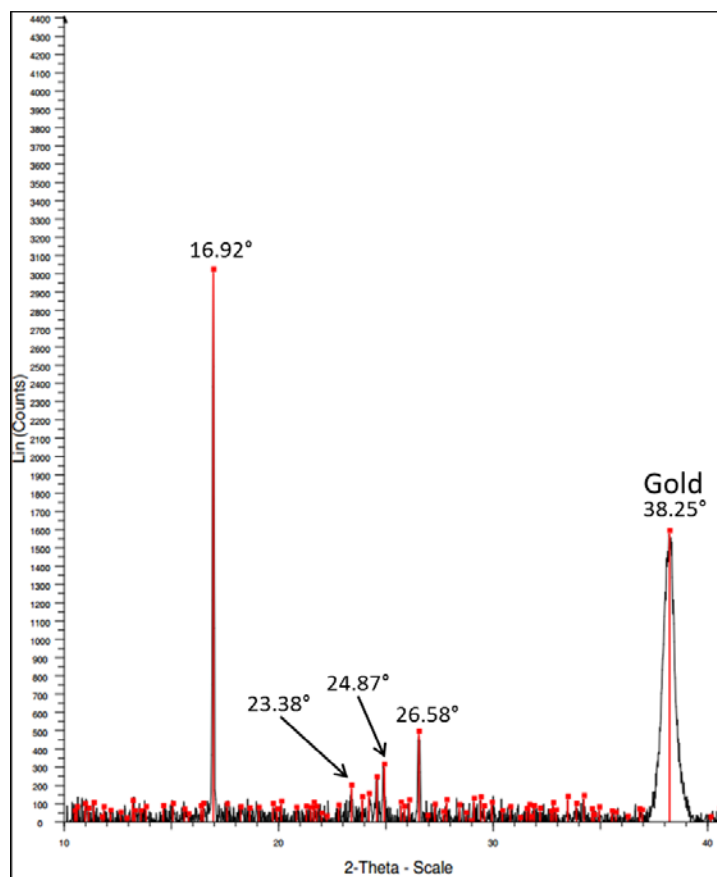


Figure B2: Diffraction pattern of RDX on the gold coated glass slide. The black diffraction pattern is the raw data of the RDX on SiO_2 substrate and the red are the peaks identified by the Bruker Eva software program. The contribution from the gold is labeled at ~ 38.25 degrees.

The measured RDX x-ray powder pattern matches the PDF entry (Powder Diffraction File) entry 00-044-1619, which is from the alpha form of RDX with unit-cell parameters of $a= 13.192$, $b= 11.592$, $c= 10.709$, and $\alpha=\beta=\gamma=90$ deg. The four major peaks at 16.92, 23.38, 24.87,

and 26.58 degrees match the α -RDX PDF entry. The diffraction pattern of the RDX on gold and the RDX on SiO₂ substrate are similar and agree with α -RDX. There are slight differences between the peaks which may be due to small structural differences between the two samples.

APPENDIX C

C.1 SUPPORTING INFORMATION FOR CHAPTER 5

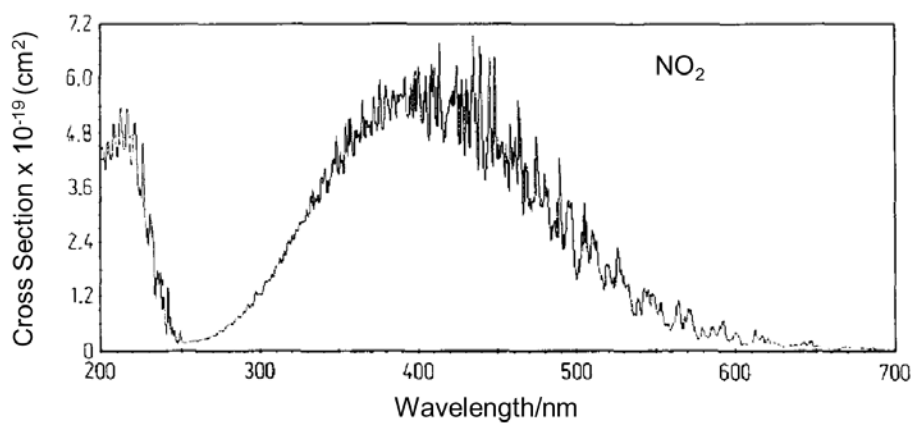


Figure C1: Total absorption spectrum of gaseous NO₂ measured at 298 K. [Reproduced with permission of Elsevier Sequoia.¹³³]

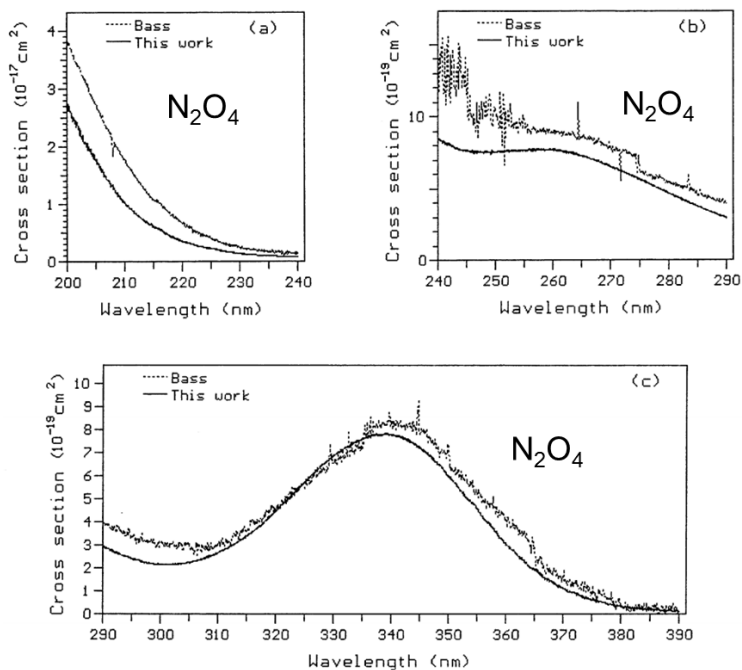


Figure C2: Absorption cross sections of gaseous N_2O_4 at 220 K. The cross sections are compared to previous work completed by Bass et al. (1976) at 250 K. [Reproduced with the permission of Kluwer Academic Publishers.¹⁴⁴]

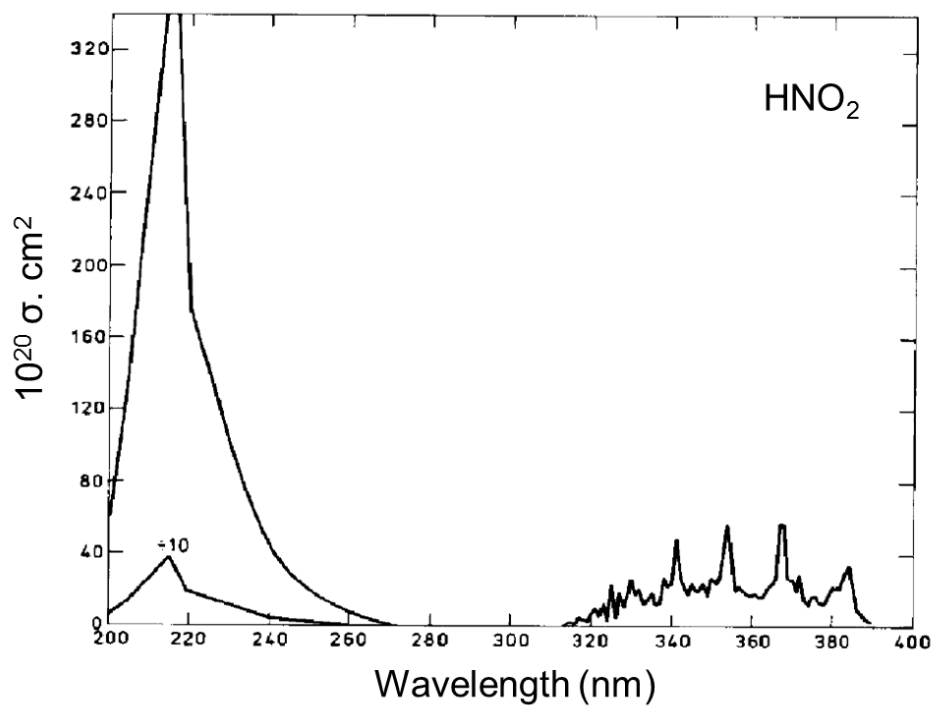


Figure C3: Absorption cross sections of gaseous HNO₂. [Reproduced with permission from Elsevier. ¹⁵³]

APPENDIX D

D.1 EXPLOSIVE HANDLING AND SAFETY PROCEDURES

D.1.1 Purpose

This Explosive Safety Guide has been compiled for the handling of explosives at the University of Pittsburgh.

D.1.2 Storage

All explosives are stored in Type 2 indoor magazines that compile with ATF storage requirements ATF specs 27 CFR 555.11. The 2 hidden locks are used on the indoor magazines according to ATF guidelines. The exterior of the magazines are 1/4" ASTM A-36 prime steel and the interior is lined with 3" of hardwood with two lock staples that are shrouded by 1/4" steel hoods. There is a hinge side door that offers protection to prevent the door from being opened if the hinges are broken. The magazines are properly vented and are mounted on 6' wide angle beams that keep the bottom of the magazines off the ground.

The high explosives are stored in a separate indoor magazine from the low explosives, according to ATF specs 555.202 (Figures D1 and D2).



Figure D1: Magazine containing high explosives.



Figure D2: Magazine containing low explosives.

D.1.3 Explosive Usage

Small quantities are used in experiments. The goal of our research is to detect explosives and their photochemical products (not for detonation) using UV resonance Raman spectroscopy. We use low power (<10 mW) deep UV laser beams for excitation of the explosives. The samples are less than one gram of explosive powder that is dissolved into acetonitrile to make a solution. We then test the explosives in the solution state or the solid state. For the solid state the solution

sample is dissolved in a salt powder such as MgF_2 and/or used deposited as explosive films on a quartz slide. The solid sample is placed into the groove of a brass spinning cell or attached to the brass spinning cell in the case of the quartz slides. Liquid samples are placed into a 1 cm path length cuvette. Both of these samples can then be placed in the Raman setup and interrogated with the laser beam for the experiments.

D.1.4 Explosive Inventory

An inventory of the explosives is kept and updated every year. The explosive magazines are inspected each week and a weekly magazine log sheet is completed. The personnel using the explosives will keep a log of the amount of explosive they take out of the magazine with the log sheet.

D.1.5 Personnel Limits

1. Access to the indoor magazines is limited to 1 or 2 personnel involved in the project.
2. Access control is also implemented by having two locks on each indoor magazine. The keys for the magazine are kept safe by the personnel responsible for keeping the keys.
3. The storage box should never be left open and unattended by the personnel who have the access keys.
4. It is the personnel with key access that should make sure the magazines display explosive warning signs.
5. The supervisor should be notified immediately about any unsafe procedures.

6. The person with key access should keep a weekly inventory and a DSMT for the explosives in the magazines.

D.1.6 Explosive Inventory

1. All personnel should follow safety procedures when handling an explosive sample or storing explosives in the proper magazines.
2. Matches, cigarette lighters, or any other flame producing devices are not permitted in the areas where the magazines are stored. Smoking is not permitted in the building as well.
3. Gasoline-, diesel-, and LPG-powered equipment will not be used near the magazines.
4. Explosive warning signs are posted on the magazines.
5. Personal protective equipment must be worn while handling explosives. These are lab coat, gloves, and safety glasses.
6. Safe handling procedures must be understood by personnel handling the explosives. Low explosives are static sensitive and susceptible to moisture. High explosives are shock or cap sensitive and are to be stored separately. All explosives are sensitive to climate conditions and static electricity. Therefore, all explosives should be handled with care to avoid static discharge.
7. Clothes containing cotton, flame-retardant cotton, or Nomex are preferred to be worn when handling explosives. Clothing that should not be worn while handling explosives includes materials such as nylon or other synthetics, silk, or wool. These materials produce charges of static electricity and can cause ignition of the explosives. Furthermore, static dissipative shoes, gloves, and lab coat are encouraged to reduce static discharge.

8. Small amounts of explosives are used and therefore no large spills should occur. To clean up any spill of any explosive material or flammable liquid, personnel should follow the proper expert advice for the spill cleanup.
9. A “buddy system” should be utilized when handling the explosive materials. According to University guidelines (EH&S # 03-020) state that “laboratory personnel should not work alone when handling hazardous materials.” Information is found at the following link: <http://www.ehs.pitt.edu/assets/docs/03-020WorkingAloneinLabs.pdf>.

D.2 STANDARD OPERATING PROCEDURES (SOP)

The following procedure describes the correct method to handle explosives at the University of Pittsburgh, Asher research group. This procedure applies to all staff who perform work involving the storage of explosives or who use small explosive samples for experiments.

D.2.1 Purpose

Any people who conduct experiments that involved explosives are responsible to understand and follow the procedure to handle the explosives properly.

D.2.2 Procedure

This procedure is to be followed and completed each time an explosive sample is needed.

1. Make sure the MSDS has been read for the particular compound being used. Make sure clothing is not static sensitive and there are no materials that could cause fires (matches or cigarette lighters) in the vicinity.
2. Make sure that gloves, safety glasses, and a lab coat are being worn. Static dissipative shoes are also encouraged. Make sure fire extinguishers are available if needed.
3. Open the locks on the magazine with the keys.
4. Take the needed amount of explosive (less than 1 gram) for sample preparation from the magazine. Close and lock the magazine. Close the door to the room.
5. Carry the sample to the lab space.
6. Then, weigh the sample on a laboratory balance and write down the material's name and weight used in a lab notebook.
7. Return any unused explosive material back to its container in the locked magazine. Close the lid or door of the magazine and lock it once again.
8. Always have the magazine lid or door closed and locked and never left unattended when open.
9. Record in the DSMT the type of material taken out of the magazine, date it was removed, the quantity removed, and the total amount remaining in the magazine that day.

D.2.3 Sample Preparation and Experiment

1. Prepare the sample according to what is needed for the experiment.
2. Place either the solid or solution sample in the appropriate Raman setup, where it will be irradiated with a deep UV laser.

3. Once the irradiation is complete the sample is placed into a waste container to be disposed of by EH&S. Solution samples can be taken to the waste room as is, with a waste label appropriately labeled. Solid samples must be dissolved in acetonitrile or a solvent the explosive is compatible with and then placed in the waste room with the appropriately labeled waste label.

Handle the explosive materials carefully according to their MSDS during the experiment.

D.2.4 Fire Safety

1. Fire extinguishers are located on the walls, near the magazines in the hallways of the floor which they are stored on. They are also located in the area where experiments are performed with the explosives.
2. Personnel handling the stored explosives are to familiarize themselves of where these fire extinguishers are located and how to use them if needed.
3. There are fire alarms and sprinklers located in the hallways of the floor that these explosives are stored on and exit signs.

D.2.5 Emergency Procedures

1. If there is a bulk spill of any explosive, call 911 and warn other people in the building. Evacuate immediately, fire or explosion is a danger with an explosive spill.
2. If there is injury to the body from fire, seek immediate medical assistance and call 911.
3. University of Pittsburgh Police number is 412-624-212.

4. University of Pittsburgh “Fire and Emergency Evacuation Procedures” can be found in EH&S guidelines 02-001.

D.2.6 Accident Reporting

1. In the case of an accident or injury, the person should seek appropriate medical attention, at an urgent care or a local hospital.
2. The supervisor should be informed of the accident or injury as soon as possible. The accident or injury should then be reported. EHS policies state “University employees should report all on-the-job accidents, injuries, or illnesses to their Supervisor and provide as much information as you can about the injury or illness.”
3. If emergency medical treatment is required call Pitt Police at 412-624-2121 (4-2121).
4. See EHS policy # 01-003.

APPENDIX E

E.1 DETAILS OF EXPERIMENTAL SETUP

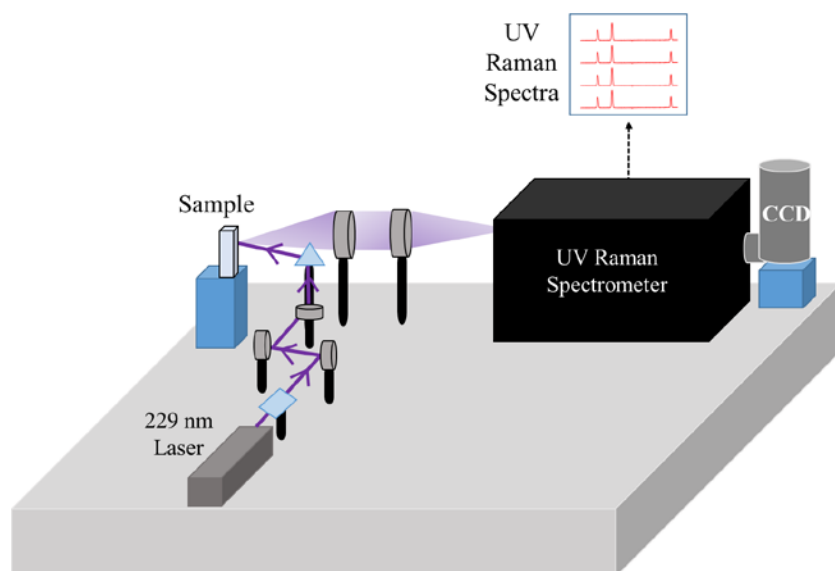


Figure E1: Diagram of experimental setup utilized for the photochemistry experiments.

The experimental setup (Figure E1) utilizes a Coherent Industries Innova 300 FreD frequency doubled Ar^+ laser to excite the explosive samples. A Spex Triplemate spectrometer along with collection optics collects the Raman scattered light. The spectrometer filters and disperses the Raman light onto a CCD detector to obtain the UVRR spectra of the explosive analytes.

The Coherent Industries Innova 300 FreD frequency doubled Ar^+ ion laser is intracavity doubled through the use of BBO nonlinear optical crystals.⁸⁷ There are 5 frequencies that can be

doubled that are below 260 nm. These frequencies are obtained by intracavity frequency doubling the 457 nm laser line through a BBO nonlinear optical crystal to produce the continuous wave (CW) 229 nm light.⁸⁷ The laser output is dispersed by a Pellin Broca prism to separate and remove the plasma emission lines.⁸⁷

A Spex Triplemate spectrometer along with collection optics are utilized to collect the Raman scattered light. The Raman scattered light is collected in a 150° backscattering geometry. The scattered light is directed into the Spex Triplemate spectrometer. The first stage disperses the scattered light and filters out the Rayleigh light.⁸⁸ The second stage disperses the light onto the CCD detector.⁸⁸ We utilize a liquid nitrogen cooled Princeton Instruments Spec-10 digital charged-coupled device (CCD) detector to detect our UVRR spectra.

APPENDIX F

F.1 STANDOFF DETECTION DIAGRAM

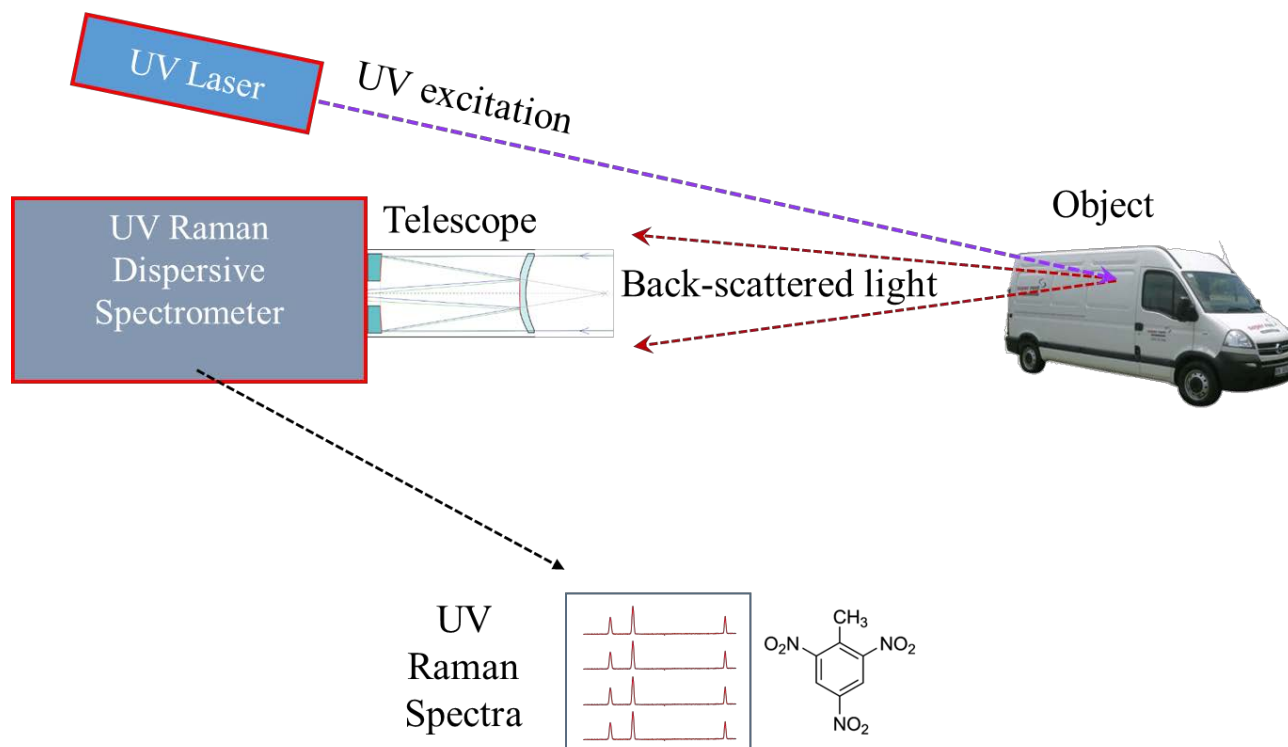


Figure F1: Diagram of the proposed rastering standoff detection setup.

BIBLIOGRAPHY

1. J. S. Caygill, F. Davis, and S. P. J. Higson, "Current trends in explosive detection techniques". *Talanta*. 2012. 88(0): 14-29.
2. A. W. Fountain, S. D. Christesen, R. P. Moon, J. A. Guicheteau, and E. D. Emmons, "Recent Advances and Remaining Challenges for the Spectroscopic Detection of Explosive Threats". *Appl. Spectrosc.* 2014. 68(8): 795-811.
3. D. S. Moore, "Instrumentation for trace detection of high explosives". *Rev. Sci. Instrum.* 2004. 75(8): 2499-2512.
4. D. S. Moore, "Recent Advances in Trace Explosives Detection Instrumentation". *Sens Imaging*. 2007. 8(1): 9-38.
5. P. M. Pellegrino, E. L. Holthoff, and M. E. Farrell. *Laser-Based Optical Detection of Explosives*. CRC Press, 2015.
6. J. I. Steinfeld and J. Wormhoudt, "EXPLOSIVES DETECTION: A Challenge for Physical Chemistry". *Annu. Rev. Phys. Chem.* 1998. 49(1): 203.
7. J. Yinon, "Field detection and monitoring of explosives". *Trac-Trend Anal Chem.* 2002. 21(4): 292-301.
8. K. L. Gares, K. T. Hufziger, S. V. Bykov, and S. A. Asher, "Review of explosive detection methodologies and the emergence of standoff deep UV resonance Raman". *J. Raman Spectrosc.* 2016. 47(1): 124-141.
9. "National Consortium for the Study of Terrorism and Responses to Terrorism (START)", (2013).
10. C. Wilson, "Improvised explosive devices (IEDs) in Iraq and Afghanistan: effects and countermeasures", (2006).
11. M. Marshall and J. C. Oxley, "Explosives: The Threats and The Materials", In: M. Marshall and J. C. Oxley, editors. *Aspects of explosives detection*. Oxford: Elsevier, 2009. 11-26.
12. K. G. Furton and L. J. Myers, "The scientific foundation and efficacy of the use of canines as chemical detectors for explosives". *Talanta*. 2001. 54(3): 487-500.
13. K. J. Garner, L. Busbee, P. Cornwell, J. Edmonds, K. Mullins, K. Rader, J. Johnston, and J. Williams, "Duty cycle of the detector dog: A baseline study". *Institute for Biological Detection Systems, Auburn University*. 2001.
14. R. G. Ewing, D. A. Atkinson, G. Eiceman, and G. Ewing, "A critical review of ion mobility spectrometry for the detection of explosives and explosive related compounds". *Talanta*. 2001. 54(3): 515-529.
15. M. E. Germain and M. J. Knapp, "Optical explosives detection: from color changes to fluorescence turn-on". *Chem. Soc. Rev.* 2009. 38(9): 2543-2555.

16. S. J. Toal and W. C. Trogler, "Polymer sensors for nitroaromatic explosives detection". *J. Mater. Chem.* 2006. 16(28): 2871-2883.
17. C. J. Cumming, C. Aker, M. Fisher, M. Fok, M. J. La Grone, D. Reust, M. G. Rockley, T. M. Swager, E. Towers, and V. Williams, "Using novel fluorescent polymers as sensory materials for above-ground sensing of chemical signature compounds emanating from buried landmines". *IEEE transactions on geoscience and remote sensing.* 2001. 39(6): 1119-1128.
18. J. C. Carter, S. M. Angel, M. Lawrence-Snyder, J. Scaffidi, R. E. Whipple, and J. G. Reynolds, "Standoff Detection of High Explosive Materials at 50 Meters in Ambient Light Conditions Using a Small Raman Instrument". *Appl. Spectrosc.* 2005. 59(6): 769-775.
19. S. K. Sharma, P. G. Lucey, M. Ghosh, H. W. Hubble, and K. A. Horton, "Stand-off Raman spectroscopic detection of minerals on planetary surfaces". *Spectrochim. Acta, Part A.* 2003. 59(10): 2391-2407.
20. J. J. Brady, S. D. Roberson, M. E. Farrell, E. L. Holthoff, D. N. Stratis-Cullum, and P. M. Pellegrino, "Laser-Induced Breakdown Spectroscopy: A Review of Applied Explosive Detection", (DTIC Document, 2013).
21. J. L. Gottfried, F. C. De Lucia, C. A. Munson, and A. W. Miziolek, "Laser-induced breakdown spectroscopy for detection of explosives residues: a review of recent advances, challenges, and future prospects". *Anal Bioanal Chem.* 2009. 395(2): 283-300.
22. C. Lopez-Moreno, S. Palanco, J. J. Laserna, F. DeLucia Jr, A. W. Miziolek, J. Rose, R. A. Walters, and A. I. Whitehouse, "Test of a stand-off laser-induced breakdown spectroscopy sensor for the detection of explosive residues on solid surfaces". *J. Anal. At. Spectrom.* 2006. 21(1): 55-60.
23. M. T. Bremer, P. J. Wrzesinski, N. Butcher, V. V. Lozovoy, and M. Dantus, "Highly selective standoff detection and imaging of trace chemicals in a complex background using single-beam coherent anti-Stokes Raman scattering". *Applied Physics Letters.* 2011. 99(10): 101109.
24. O. Katz, A. Natan, Y. Silberberg, and S. Rosenwaks, "Standoff detection of trace amounts of solids by nonlinear Raman spectroscopy using shaped femtosecond pulses". *Applied Physics Letters.* 2008. 92(17): 171116.
25. A. Natan, J. M. Levitt, L. Graham, O. Katz, and Y. Silberberg, "Standoff detection via single-beam spectral notch filtered pulses". *Appl. Phys. Lett.* 2012. 100(5): 051111.
26. J.-X. Cheng and X. S. Xie, "Coherent anti-Stokes Raman scattering microscopy: instrumentation, theory, and applications", (ACS Publications, 2004).
27. J. A. Carroll, E. L. Izake, B. Cletus, and E. Jaatinen, "Eye-safe UV stand-off Raman spectroscopy for the ranged detection of explosives in the field". *J. Raman Spectrosc.* 2015. 46(3): 333-338.
28. M. Ghosh, L. Wang, and S. A. Asher, "Deep-Ultraviolet Resonance Raman Excitation Profiles of NH_4NO_3 , PETN, TNT, HMX, and RDX". *Appl Spectrosc.* 2012. 66(9): 1013-1021.
29. H. Östmark, M. Nordberg, and T. E. Carlsson, "Stand-off detection of explosives particles by multispectral imaging Raman spectroscopy". *Appl. Opt.* 2011. 50(28): 5592-5599.
30. A. Pettersson, I. Johansson, S. Wallin, M. Nordberg, and H. Östmark, "Near Real-Time Standoff Detection of Explosives in a Realistic Outdoor Environment at 55 m Distance". *Propell. Explos. Pyrot.* 2009. 34(4): 297-306.
31. D. D. Tuschel, A. V. Mikhonin, B. E. Lemoff, and S. A. Asher, "Deep Ultraviolet Resonance Raman Excitation Enables Explosives Detection". *Appl. Spectrosc.* 2010. 64(4): 425-432.

32. S. Wallin, A. Pettersson, H. Östmark, and A. Hobro, "Laser-based standoff detection of explosives: a critical review". *Anal Bioanal Chem.* 2009. 395(2): 259-274.
33. K. T. Hufziger, S. V. Bykov, and S. A. Asher, "Ultraviolet Raman Wide-Field Hyperspectral Imaging Spectrometer for Standoff Trace Explosive Detection". *Appl. Spectrosc.* 2017. 71(2): 173-185.
34. S. K. Sharma, A. K. Misra, and B. Sharma, "Portable remote Raman system for monitoring hydrocarbon, gas hydrates and explosives in the environment". *Spectrochimica Acta Part A: Molecular and Biomolecular Spectroscopy.* 2005. 61(10): 2404-2412.
35. J. C. Carter, S. M. Angel, M. Lawrence-Snyder, J. Scaffidi, R. E. Whipple, and J. G. Reynolds, "Standoff detection of high explosive materials at 50 meters in ambient light conditions using a small Raman instrument". *Appl. Spectrosc.* 2005. 59(6): 769-775.
36. H. Östmark, M. Nordberg, and T. E. Carlsson, "Stand-off detection of explosives particles by multispectral imaging Raman spectroscopy". *Appl. Opt.* 2011. 50(28): 5592-5599.
37. S. V. Bykov, M. Mao, K. L. Gares, and S. A. Asher, "Compact Solid-State 213 nm Laser Enables Standoff Deep Ultraviolet Raman Spectrometer: Measurements of Nitrate Photochemistry". *Appl. Spectrosc.* 2015. 69(8): 895-901.
38. K. L. Gares, S. V. Bykov, T. Brinzer, and S. A. Asher, "Solution and Solid Hexahydro-1, 3, 5-trinitro-1, 3, 5-triazine (RDX) Ultraviolet (UV) 229 nm Photochemistry". *Appl. Spectrosc.* 2015. 69(5): 545-554.
39. K. L. Gares, S. V. Bykov, B. Godugu, and S. A. Asher, "Solution and Solid Trinitrotoluene (TNT) Photochemistry: Persistence of TNT-like Ultraviolet (UV) Resonance Raman Bands". *Appl. Spectrosc.* 2014. 68(1): 49-56.
40. K. T. Hufziger, S. V. Bykov, and S. A. Asher, "Raman Hyperspectral Imaging Spectrometer Utilizing Crystalline Colloidal Array Photonic Crystal Diffraction". *Appl. Spectrosc.* 2014. 68(11): 1219-1223.
41. T. A. Reichardt, S. E. Bisson, and T. J. Kulp, "Standoff Ultraviolet Raman Scattering Detection of Trace Levels of Explosives". Sandia National Labs. 2011.
42. L. Wang, D. Tuschel, and S. A. Asher, "229 nm UV photochemical degradation of energetic molecules", in *Proc. of SPIE* (2011), p. 80181B-80181B.
43. S. A. Asher, "UV resonance Raman spectroscopy for analytical, physical, and biophysical chemistry". *Anal. Chem.* 1993. 65(4): 201A-210A.
44. S. A. Asher and C. R. Johnson, "Raman spectroscopy of a coal liquid shows that fluorescence interference is minimized with ultraviolet excitation". *Science.* 1984. 225(4659): 311-313.
45. L. Wang, D. Tuschel, and S. A. Asher, "Templated Photonic Crystal Fabrication of Stoichiometrically Complex Nanoparticles for Resonance Raman Solid Cross Section Determinations". *J. Phys. Chem. C.* 2011. 115(32): 15767-15771.
46. E. D. Emmons, J. A. Guicheteau, A. W. Fountain, and S. D. Christesen, "Comparison of visible and near-infrared Raman cross-sections of explosives in solution and in the solid state". *Appl. Spectrosc.* 2012. 66(6): 636-643.
47. E. D. Emmons, A. Tripathi, J. A. Guicheteau, A. W. Fountain, and S. D. Christesen, "Ultraviolet Resonance Raman Spectroscopy of Explosives in Solution and the Solid State". *J. Phys. Chem. A.* 2013. 117(20): 4158-4166.
48. C. E. Wayne and R. P. Wayne. *Photochemistry.* New York: Oxford University Press Inc., 1996.

49. B. Wardle. Principles and Applications of Photochemistry. John Wiley & Sons, Ltd, 2009.
50. K. L. Gares, S. V. Bykov, and S. A. Asher, "UV Resonance Raman Investigation of Pentaerythritol Tetranitrate Solution Photochemistry and Photoproduct Hydrolysis". Anal Chem. 2017. submitted.
51. S. A. Asher, D. D. Tuschel, T. A. Vargson, L. Wang, and S. J. Geib, "Solid State and Solution Nitrate Photochemistry: Photochemical Evolution of the Solid State Lattice". J. Phys. Chem. A. 2011. 115(17): 4279-4287.
52. T. L. Andrew and T. M. Swager, "Detection of Explosives via Photolytic Cleavage of Nitroesters and Nitramines". J. Org. Chem. 2011. 76(9): 2976-2993.
53. J. C. Sanchez and W. C. Troglor, "Efficient blue-emitting silafluorene-fluorene-conjugated copolymers: selective turn-off/turn-on detection of explosives". J. Mater. Chem. 2008. 18(26): 3143-3156.
54. M. L. Clark, M. J. Aernecke, K. E. Gregory, D. E. Hardy, and R. R. Kunz, "Sensing Impacts of the Fate of Trace Explosives Signatures under Environmental Conditions", (2010), p. 1-8.
55. M. Greenfield, Y. Q. Guo, and E. R. Bernstein, "Ultrafast photodissociation dynamics of HMX and RDX from their excited electronic states via femtosecond laser pump-probe techniques". Chem. Phys. Lett. 2006. 430(4-6): 277-281.
56. H.-S. Im and E. R. Bernstein, "On the initial steps in the decomposition of energetic materials from excited electronic states". J. Chem. Phys. 2000. 113(18): 7911-7918.
57. R. R. Kunz, K. E. Gregory, M. J. Aernecke, M. L. Clark, A. Ostrinskaya, and A. W. Fountain, 3rd, "Fate dynamics of environmentally exposed explosive traces". J. Phys. Chem. A. 2012. 116(14): 3611-3624.
58. J. C. Pennington, K. A. Thorn, L. G. Cox, D. K. MacMillan, S. Yost, and R. D. Laubscher, "Photochemical degradation of composition B and its components", (Engineer Research and Development Center, Vicksburg, Miss., 2007).
59. G. R. Peyton, M. H. LeFaivre, and S. W. Maloney, "Verification of RDX photolysis mechanism", (Engineer Research and Development Center, 1999).
60. A. F. Smetana and S. Bulusu, "Photochemical Studies of Secondary Nitramines. Part 2. Ultraviolet Photolysis and Ozonolysis of RDX in Aqueous Solutions", (Large Caliber Weapons Systems Laboratory, 1977).
61. N. E. Burlinson, L. A. Kaplan, and C. A. Adams, "Photochemistry of TNT: Investigation of the "Pink Water" Problem", (Naval Ordnance Laboratory Silver Spring, Maryland 20910, 1973).
62. L. A. Kaplan, N. E. Burlinson, and M. E. Sitzmann, "Photochemistry of TNT: Investigation of the "Pink Water" Problem: Part II", (Naval Surface Weapons Center White Oak Laboratory: Silver Spring, MD, 1975).
63. O. Sandus and N. Slagg, "Mechanism of the Formation of Pink Water", (U.S. Army Armament Research and Development Command: Dover, NJ, 1978).
64. D. J. Glover and J. C. Hoffsommer, "Photolysis of RDX in aqueous solution, with and without ozone", (Naval Surface Weapons Center 1979).
65. Y. Q. Guo, M. Greenfield, A. Bhattacharya, and E. R. Bernstein, "On the excited electronic state dissociation of nitramine energetic materials and model systems". J. Chem. Phys. 2007. 127(15): -.

66. N. J. Harris and K. Lammertsma, "Ab Initio Density Functional Computations of Conformations and Bond Dissociation Energies for Hexahydro-1,3,5-trinitro-1,3,5-triazine". *J. Am. Chem. Soc.* 1997. 119(28): 6583-6589.
67. I. Barnes, K. H. Becker, and T. Zhu, "Near UV absorption spectra and photolysis products of difunctional organic nitrates: Possible importance as NO_x reservoirs". *J. Atmos. Chem.* 17(4): 353-373.
68. R. W. Binkley and D. J. Koholic, "Photolysis of nitrate esters. Photochemically initiated inversion of configuration". *J. Org. Chem.* 1979. 44(12): 2047-2048.
69. D. Chambers, "Perspectives on Pentaerythritol Tetranitrate (PETN) Decomposition". Lawrence Livermore National Laboratory. 2002. 148956(1-18).
70. L. D. Hayward, R. A. Kitchen, and D. J. Livingstone, "Photolysis Of Nitrate Esters: Part I. Photonitration Of Diphenylamine". *Can. J. Chem.* 1962. 40(3): 434-440.
71. W. T. Luke, R. R. Dickerson, and L. J. Nunnermacker, "Direct measurements of the photolysis rate coefficients and Henry's law constants of several alkyl nitrates". *J. Geophys. Res.: Atmos.* 1989. 94(D12): 14905-14921.
72. M. A. Hiskey, K. R. Brower, and J. C. Oxley, "Thermal decomposition of nitrate esters". *J. Phys. Chem.* 1991. 95(10): 3955-3960.
73. W. Ng, J. Field, and H. Hauser, "Thermal, fracture, and laser-induced decomposition of pentaerythritol tetranitrate". *J. Appl. Phys.* 1986. 59(12): 3945-3952.
74. W. L. Ng, J. E. Field, and H. M. Hauser, "Study of the thermal decomposition of pentaerythritol tetranitrate". *J. Chem. Soc. Perk T 2.* 1976. 6): 637-639.
75. B. D. Roos and T. B. Brill, "Thermal decomposition of energetic materials 82. Correlations of gaseous products with the composition of aliphatic nitrate esters". *Combust. Flame.* 2002. 128(1-2): 181-190.
76. D. A. Long and D. Long. Raman spectroscopy. McGraw-Hill New York, 1977.
77. A. B. Myers and R. A. Mathies. Resonance Raman Intensities: A Probe of Excited State Structure and Dynamics, in "Biological Applications of Raman Spectroscopy: Vol. 2 - Resonance Raman Spectra of Polyenes and Aromatics". John Wiley & Sons, Inc., 1987. 2, 1-58
78. T. G. Spiro. Biological Applications of Raman Spectroscopy. John Wiley & Sons Canada, Limited, 1988.
79. J. R. Ferraro, Nakamoto, Kazuo. Introductory Raman Spectroscopy. Academic Press Inc., 1994. 54-58.
80. S. A. Asher, "UV resonance Raman studies of molecular structure and dynamics: applications in physical and biophysical chemistry". *Annu. Rev. Phys. Chem.* 1988. 39(1): 537-588.
81. S. A. Asher, "Ultraviolet resonance Raman spectrometry for detection and speciation of trace polycyclic aromatic hydrocarbons". *Anal. Chem.* 1984. 56(4): 720-724.
82. A. C. Albrecht, "On the Theory of Raman Intensities". *J. Chem. Phys.* 1961. 34(5): 1476-1484.
83. D. Moore, "Recent Advances in Trace Explosives Detection Instrumentation". *Sens Imaging.* 2007. 8(1): 9-38.
84. D. Moore and R. J. Scharff, "Portable Raman explosives detection". *Anal Bioanal Chem.* 2009. 393(6-7): 1571-1578.
85. L. Pacheco-Londoño, W. Ortiz-Rivera, O. Primera-Pedrozo, and S. Hernández-Rivera, "Vibrational spectroscopy standoff detection of explosives". *Anal Bioanal Chem.* 2009. 395(2): 323-335.

86. I. Johansson, M. Norrefeldt, A. Pettersson, S. Wallin, and H. Östmark, "Close-Range and Standoff Detection and Identification of Liquid Explosives by Means of Raman Spectroscopy", In: H. Schubert and A. Kuznetsov, editors. *Detection of Liquid Explosives and Flammable Agents in Connection with Terrorism*. Springer Netherlands, 2008. 14, 143-153.
87. S. A. Asher, R. W. Bormett, X. G. Chen, D. H. Lemmon, N. Cho, P. Peterson, M. Arrigoni, L. Spinelli, and J. Cannon, "UV Resonance Raman Spectroscopy Using a New cw Laser Source: Convenience and Experimental Simplicity". *Appl Spectrosc.* 1993. 47(5): 628-633.
88. S. Bykov, I. Lednev, A. Ianoul, A. Mikhonin, C. Munro, and S. A. Asher, "Steady-State and Transient ultraviolet Resonance Raman Spectrometer for the 193-270 nm Spectral Region". *Appl Spectrosc.* 2005. 59(12): 1541-1552.
89. J. Clarkson, W. E. Smith, D. N. Batchelder, D. A. Smith, and A. M. Coats, "A theoretical study of the structure and vibrations of 2,4,6-trinitrotoluene". *J. Mol. Struct.* 2003. 648(3): 203-214.
90. H. Wackerbath, L. Gundrum, C. Salb, K. Christou, and W. Viol, "Challenge of false alarms in nitroaromatic explosive detection-a detection device based on surface-enhanced Raman spectroscopy". *Appl. Opt.* 2010. 49(23): 4367-4371.
91. W. A. Al-Saidi, S. A. Asher, and P. Norman, "Resonance Raman Spectra of TNT and RDX Using Vibronic Theory, Excited-State Gradient, and Complex Polarizability Approximations". *J. Phys. Chem. A.* 2012.
92. J. C. Pennington, K. A. Thorn, L. G. Cox, D. K. MacMillan, S. Yost, and R. D. Laubscher, "Photochemical degradation of composition B and its components", ([US Army Corps of Engineers, Engineer Research and Development Center], Environmental Laboratory, Vicksburg, Miss., 2007).
93. J. M. Dudik, C. R. Johnson, and S. A. Asher, "Wavelength Dependence of the Preresonance Raman Cross Sections of CH_3CN , SO_4^{2-} , ClO_4^- and NO_3^- ". *J. Chem. Phys.* 1985. 82(4): 1732-1740.
94. G. E. Nahla A. Hatab, Paukl B. Hatzinger, Baohua Gu, "Detection and analysis of cyclotrimethylenetrinitramine (RDX) in environmental samples by surface-enhanced Raman spectroscopy". *J. Raman Spectrosc.* 2010. 41(1131-1136).
95. G. R. Peyton, M. H. LeFaivre, and S. W. Maloney, "Verification of RDX Photolysis Mechanism", (Champaign, IL, 1999), p. 1-58.
96. A. H. J. Hawari, C. Groom, S. Deschamps, L. Paquet, C. Beaulieu, A. Corriveau, "Photodegradation of RDX in Aqueous Solution: A Mechanistic Probe for Biodegradation with *Rhodococcus* sp.". *Environ. Sci. Technol.* 2002. 36(23): 5117-5123.
97. B. Zachhuber, C. Gasser, G. Ramer, E. t. H. Chrysostom, and B. Lendl, "Depth Profiling for the Identification of Unknown Substances and Concealed Content at Remote Distances Using Time-Resolved Stand-Off Raman Spectroscopy". *Appl. Spectrosc.* 2012. 66(8): 875-881.
98. H.-B. Liu, Y. Chen, G. J. Bastiaans, and X. C. Zhang, "Detection and identification of explosive RDX by THz diffuse reflection spectroscopy". *Opt. Express.* 2006. 14(1): 415-423.
99. J. C. H. Donald J. Glover, "Photolysis of RDX in Aqueous Solution with and without Ozone", R. a. T. Department, Ed. (Naval Weapons Research Center White Oak, Silver Spring, MD 20910, 1979).
100. Y. Q. Guo, M. Greenfield, and E. R. Bernstein, "Decomposition of nitramine energetic materials in excited electronic states: RDX and HMX". *J. Chem. Phys.* 2005. 122(24): -.

101. Z. A. Dreger and Y. M. Gupta, "High Pressure Raman Spectroscopy of Single Crystals of Hexahydro-1,3,5-trinitro-1,3,5-triazine (RDX)". *J. Phys. Chem. B.* 2007. 111(15): 3893-3903.
102. A. Gapeev, M. Sigman, and J. Yinon, "Liquid chromatography/mass spectrometric analysis of explosives: RDX adduct ions". *Rapid Commun. Mass Spectrom.* 2003. 17(9): 943-948.
103. A. C. Ferrari, S. E. Rodil, and J. Robertson, "Interpretation of infrared and Raman spectra of amorphous carbon nitrides". *Phys. Rev. B.* 2003. 67(15): 155306.
104. S. E. Rodil, A. C. Ferrari, J. Robertson, and S. Muhl, "Infrared spectra of carbon nitride films". *Thin Solid Films.* 2002. 420-421(0): 122-131.
105. A. K. M. S. Chowdhury, D. C. Cameron, and M. S. J. Hashmi, "Vibrational properties of carbon nitride films by Raman spectroscopy". *Thin Solid Films.* 1998. 332(1-2): 62-68.
106. G. Socrates. *Infrared and Raman characteristic group frequencies: tables and charts.* John Wiley & Sons, 2004.
107. N. B. Colthup, L. H. Daly, and S. E. Wiberley. *Introduction to infrared and Raman spectroscopy.* Elsevier, 1990.
108. P. X. Feng, H. X. Zhang, and H. Y. Li, "Nanostructured Carbon Nitride Films Deposited Using The Low-Cost Penning Discharge Plasma-Sputtering Technique". *Int. J. Mod. Phys. B.* 2008. 22(23): 3957-3966.
109. P. F. McMillan, V. Lees, E. Quirico, G. Montagnac, A. Sella, B. Reynard, P. Simon, E. Bailey, M. Deifallah, and F. Corà, "Graphitic carbon nitride $C_6N_9H_3 \cdot HCl$: Characterisation by UV and near-IR FT Raman spectroscopy". *J. Solid State Chem.* 2009. 182(10): 2670-2677.
110. S. S. Roy, R. McCann, P. Papakonstantinou, P. Maguire, and J. A. McLaughlin, "The structure of amorphous carbon nitride films using a combined study of NEXAFS, XPS and Raman spectroscopies". *Thin Solid Films.* 2005. 482(1-2): 145-150.
111. E. D. Emmons, M. E. Farrell, E. L. Holthoff, A. Tripathi, N. Green, R. P. Moon, J. A. Guicheteau, S. D. Christesen, P. M. Pellegrino, and A. W. F. Iii, "Characterization of Polymorphic States in Energetic Samples of 1,3,5-Trinitro-1,3,5-Triazine (RDX) Fabricated Using Drop-on-Demand Inkjet Technology". *Appl. Spectrosc.* 2012. 66(6): 628-635.
112. I. G. Goldberg and J. A. Swift, "New Insights into the Metastable β Form of RDX". *Crystal Growth & Design.* 2012. 12(2): 1040-1045.
113. R. J. Karpowicz and T. B. Brill, "Comparison of the molecular structure of hexahydro-1,3,5-trinitro-s-triazine in the vapor, solution and solid phases". *J. Phys. Chem.* 1984. 88(3): 348-352.
114. R. Infante-Castillo, L. C. Pacheco-Londoño, and S. P. Hernández-Rivera, "Monitoring the $\alpha \rightarrow \beta$ solid-solid phase transition of RDX with Raman spectroscopy: A theoretical and experimental study". *J. Mol. Struct.* 2010. 970(1-3): 51-58.
115. B. M. Rice and C. F. Chabalowski, "Ab Initio and Nonlocal Density Functional Study of 1,3,5-Trinitro-s-triazine (RDX) Conformers". *J. Phys. Chem. A.* 1997. 101(46): 8720-8726.
116. P. Torres, L. Mercado, I. Cotte, S. P. Hernández, N. Mina, A. Santana, R. T. Chamberlain, R. Lareau, and M. E. Castro, "Vibrational Spectroscopy Study of β and α RDX Deposits". *J. Phys. Chem. B.* 2004. 108(26): 8799-8805.
117. F. J. Owens and J. Sharma, "X-ray photoelectron spectroscopy and paramagnetic resonance evidence for shock-induced intramolecular bond breaking in some energetic solids". *J. Appl. Phys.* 1980. 51(3): 1494-1497.

118. C. M. Mahoney, A. J. Fahey, K. L. Steffens, B. A. Benner, and R. T. Lareau, "Characterization of Composition C4 Explosives using Time-of-Flight Secondary Ion Mass Spectrometry and X-ray Photoelectron Spectroscopy". *Anal. Chem.* 2010. 82(17): 7237-7248.
119. M. Aono, S. Aizawa, N. Kitazawa, and Y. Watanabe, "XPS study of carbon nitride films deposited by hot filament chemical vapor deposition using carbon filament". *Thin Solid Films.* 2008. 516(5): 648-651.
120. E. Ech-chamikh, A. Essafti, Y. Ijdiyaou, and M. Azizan, "XPS study of amorphous carbon nitride (a-C:N) thin films deposited by reactive RF sputtering". *Sol. Energy Mater. Sol. Cells.* 2006. 90(10): 1420-1423.
121. M. Kim, S. Hwang, and J.-S. Yu, "Novel ordered nanoporous graphitic C₃N₄ as a support for Pt-Ru anode catalyst in direct methanol fuel cell". *J. Mater. Chem.* 2007. 17(17): 1656-1659.
122. M. Matsuoka, S. Isotani, R. D. Mansano, W. Sucasaire, R. A. Pinto, J. C. Mittani, K. Ogata, and N. Kuratani, "X-Ray Photoelectron Spectroscopy and Raman Spectroscopy Studies on Thin Carbon Nitride Films Deposited by Reactive RF Magnetron Sputtering". *World J. Nano Sci. Eng.* 2012.
123. A. Thomas, A. Fischer, F. Goettmann, M. Antonietti, J.-O. Muller, R. Schlogl, and J. M. Carlsson, "Graphitic carbon nitride materials: variation of structure and morphology and their use as metal-free catalysts". *J. Mater. Chem.* 2008. 18(41): 4893-4908.
124. A. K. Misra, S. K. Sharma, T. E. Acosta, J. N. Porter, and D. E. Bates, "Single-pulse standoff Raman detection of chemicals from 120 m distance during daytime". *Appl. Spectrosc.* 2012. 66(11): 1279-1285.
125. S. K. Sharma, A. K. Misra, and B. Sharma, "Portable remote Raman system for monitoring hydrocarbon, gas hydrates and explosives in the environment". *Spectrochim. Acta, Part A.* 2005. 61(10): 2404-2412.
126. P. Gray and A. Yoffe, "The Reactivity and Structure of Nitrogen Dioxide". *Chem. Rev.* 1955. 55(6): 1069-1154.
127. Y. A. Gruzdkov and Y. M. Gupta, "Vibrational Properties and Structure of Pentaerythritol Tetranitrate". *J. Phys. Chem. A.* 2001. 105(25): 6197-6202.
128. W. F. Perger, J. Zhao, J. M. Winey, and Y. M. Gupta, "First-principles study of pentaerythritol tetranitrate single crystals under high pressure: Vibrational properties". *Chem. Phys. Lett.* 2006. 428(4-6): 394-399.
129. X. Zhao and J. Yinon, "Identification of nitrate ester explosives by liquid chromatography–electrospray ionization and atmospheric pressure chemical ionization mass spectrometry". *J. Chromatogr. A.* 2002. 977(1): 59-68.
130. H. Brust, A. van Asten, M. Koeberg, J. Dalmolen, A. van der Heijden, and P. Schoenmakers, "Accurate quantitation of pentaerythritol tetranitrate and its degradation products using liquid chromatography–atmospheric pressure chemical ionization–mass spectrometry". *J. Chromatogr. A.* 2014. 1338(111-116).
131. H. Brust, A. van Asten, M. Koeberg, A. van der Heijden, C.-J. Kuijpers, and P. Schoenmakers, "Pentaerythritol tetranitrate (PETN) profiling in post-explosion residues to constitute evidence of crime-scene presence". *Forensic Sci. Int.* 2013. 230(1): 37-45.
132. P. Mullen and M. Orloff, "Ultraviolet absorption spectrum of pentaerythritol tetranitrate". *J. Phys. Chem.* 1973. 77(7): 910-911.
133. W. Schneider, G. K. Moortgat, G. S. Tyndall, and J. P. Burrows, "Absorption cross-sections of NO₂ in the UV and visible region (200–700 nm) at 298 K". *J. Photochem. Photobiol., A.* 1987. 40(2-3): 195-217.

134. C. England and W. H. Corcoran, "Kinetics and Mechanisms of the Gas-Phase Reaction of Water Vapor and Nitrogen Dioxide". *Ind. Eng. Chem. Fundam.* 1974. 13(4): 373-384.
135. R. Zhu, K.-Y. Lai, and M. Lin, "Ab initio chemical kinetics for the hydrolysis of N₂O₄ isomers in the gas phase". *J. Phys. Chem. A.* 2012. 116(18): 4466-4472.
136. F. Bolduan, H. Jodl, and A. Loewenschuss, "Raman study of solid N₂O₄: temperature induced autoionization". *J. Chem. Phys.* 1984. 80(5): 1739-1743.
137. N. Minogue, E. Riordan, and J. R. Sodeau, "Raman spectroscopy as a probe of low-temperature ionic speciation in nitric and sulfuric acid stratospheric mimic systems". *J. Phys. Chem. A.* 2003. 107(22): 4436-4444.
138. B. Finlayson-Pitts, L. Wingen, A. Sumner, D. Syomin, and K. Ramazan, "The heterogeneous hydrolysis of NO₂ in laboratory systems and in outdoor and indoor atmospheres: an integrated mechanism". *Phys. Chem. Chem. Phys.* 2003. 5(2): 223-242.
139. M. A. Kamboures, J. D. Raff, Y. Miller, L. F. Phillips, B. J. Finlayson-Pitts, and R. B. Gerber, "Complexes of HNO₃ and NO₃⁻ with NO₂ and N₂O₄, and their potential role in atmospheric HONO formation". *Phys. Chem. Chem. Phys.* 2008. 10(39): 6019-6032.
140. H. Lucas and J.-P. Petitet, "High Pressure Raman Spectroscopy of Nitric Acid". *J. Phys. Chem. A.* 1999. 103(45): 8952-8958.
141. C. Ratcliffe and D. Irish, "Vibrational spectral studies of solutions at elevated temperatures and pressures. VII. Raman spectra and dissociation of nitric acid". *Can. J. Chem.* 1985. 63(12): 3521-3525.
142. O. Redlich and L. Nielsen, "Raman Spectrum and Molecular Vibrations of Nitric and Deuteronitric Acids". *J. Am. Chem. Soc.* 1943. 65(4): 654-660.
143. S. A. Stern, J. Mullhaupt, and W. B. Kay, "The Physicochemical Properties of Pure Nitric Acid". *Chem. Rev.* 1960. 60(2): 185-207.
144. M. F. Merienne, A. Jenouvrier, B. Coquart, and J. P. Lux, "The NO₂ absorption spectrum. IV: The 200–400 nm region at 220 K". *J. Atmos. Chem.* 1997. 27(3): 219-232.
145. T. C. Hall and F. E. Blacet, "Separation of the Absorption Spectra of NO₂ and N₂O₄ in the Range of 2400–5000Å". *J. Chem. Phys.* 1952. 20(11): 1745-1749.
146. M. Merienne, A. Jenouvrier, B. Coquart, and J. Lux, "The NO₂ absorption spectrum. IV: The 200–400 nm region at 220 K". *J. Atmos. Chem.* 1997. 27(3): 219-232.
147. T. F. Redmond and B. B. Wayland, "Dimerization of nitrogen dioxide in solution: a comparison of solution thermodynamics with the gas phase". *J. Phys. Chem.* 1968. 72(5): 1626-1629.
148. H. Johnston and R. Graham, "Gas-phase ultraviolet absorption spectrum of nitric acid vapor". *J. Phys. Chem.* 1973. 77(1): 62-63.
149. R. N. Jones, G. Thorn, M. Lyne, and E. Taylor, "Ultra-violet Absorption Spectrum of Anhydrous Nitric Acid". *Nature.* 1947. 159(163-165).
150. A. Genich, L. Eremenko, and L. Nikitina, "Spectra and molecular structure of nitric acid in solutions". *Russ. Chem. Bull.* 1967. 16(4): 733-735.
151. A. Bongartz, J. Kames, F. Welter, and U. Schurath, "Near-UV absorption cross sections and trans/cis equilibrium of nitrous acid". *J. Phys. Chem.* 1991. 95(3): 1076-1082.
152. G. King and D. Moule, "The ultraviolet absorption spectrum of nitrous acid in the vapor state". *Can. J. Chem.* 1962. 40(11): 2057-2065.
153. R. Cox and R. Derwent, "The Ultra-Violet Absorption Spectrum of Gaseous Nitrous Acid". *J. Photochem.* 1976. 6(1): 23-34.